Emeis, K.-C., Robertson, A.H.F., Richter, C., et al., 1996
Proceedings of the Ocean Drilling Program, Initial Reports, Vol. 160

10. SITE 969[1]

Shipboard Scientific Party[2]

HOLE 969A

Date occupied: 14 April 1995

Date departed: 15 April 1995

Time on hole: 16 hr, 15 min

Position: 33°50.399′N, 24°53.065′E

Bottom felt (drill-pipe measurement from rig floor, m): 2211.8

Distance between rig floor and sea level (m): 11.5

Water depth (drill-pipe measurement from sea level, m): 2200.3

Total depth (from rig floor, m): 2320.1

Penetration (m): 108.3

Number of cores (including cores having no recovery): 13

Total length of cored section (m): 108.3

Total core recovered (m): 111.4

Core recovery (%): 102.9

Oldest sediment cored:
Depth (mbsf): 108.30
Nature: calcareous silty clay
Measured velocity (km/s): 1.95

HOLE 969B

Date occupied: 15 April 1995

Date departed: 15 April 1995

Time on hole: 10 hr, 30 min

Position: 33°50.469′N, 24°52.978′E

Bottom felt (drill-pipe measurement from rig floor, m): 2213.6

Distance between rig floor and sea level (m): 11.5

Water depth (drill-pipe measurement from sea level, m): 2202.1

Total depth (from rig floor, m): 2311.5

Penetration (m): 97.9

Number of cores (including cores having no recovery): 11

Total length of cored section (m): 97.9

Total core recovered (m): 100.2

Core recovery (%): 102.3

Oldest sediment cored:
Depth (mbsf): 97.90
Nature: clayey nannofossil ooze
Earliest age: early Pliocene
Measured velocity (km/s): 1.7

HOLE 969C

Date occupied: 15 April 1995

Date departed: 15 April 1995

Time on hole: 02 hr

Position: 33°50.323′N, 24°53.005′E

Bottom felt (drill-pipe measurement from rig floor, m): 2207.0

Distance between rig floor and sea level (m): 11.5

Water depth (drill-pipe measurement from sea level, m): 2195.5

Total depth (from rig floor, m): 2216.5

Penetration (m): 9.5

Number of cores (including cores having no recovery): 1

Total length of cored section (m): 9.5

Total core recovered (m): 10.0

Core recovery (%): 105.0

Oldest sediment cored:
Depth (mbsf): 9.50
Nature: nannofossil ooze
Earliest age: Pleistocene
Measured velocity (km/s): 1.6

HOLE 969D

Date occupied: 15 April 1995

Date departed: 16 April 1995

Time on hole: 12 hr, 15 min

Position: 33°50.319′N, 24°53.000′E

Bottom felt (drill-pipe measurement from rig floor, m): 2203.6

Distance between rig floor and sea level (m): 11.5

Water depth (drill-pipe measurement from sea level, m): 2192.1

Total depth (from rig floor, m): 2319.8

Penetration (m): 116.2

Number of cores (including cores having no recovery): 13

Total length of cored section (m): 116.2

Total core recovered (m): 118.5

Core recovery (%): 102.0

Oldest sediment cored:
Depth (mbsf): 116.20
Nature: nannofossil clay
Earliest age: early Pliocene
Measured velocity (km/s): 1.7

HOLE 969E

Date occupied: 16 April 1995

Date departed: 16 April 1995

[1]Emeis, K.-C., Robertson, A.H.F., Richter, C., et al., 1996. *Proc. ODP, Init. Repts.,* 160: College Station, TX (Ocean Drilling Program).
[2]Shipboard Scientific Party is given in the list preceding the Table of Contents.

Time on hole: 09 hr, 15 min

Position: 33°50.462′N, 24°52.981′E

Bottom felt (drill-pipe measurement from rig floor, m): 2212.6

Distance between rig floor and sea level (m): 11.5

Water depth (drill-pipe measurement from sea level, m): 2201.1

Total depth (from rig floor, m): 2310.5

Penetration (m): 97.9

Number of cores (including cores having no recovery): 11

Total length of cored section (m): 97.9

Total core recovered (m): 100.2

Core recovery (%): 102.4

Oldest sediment cored:
Depth (mbsf): 97.90
Nature: nannofossil clay
Measured velocity (km/s): 2.0

HOLE 969F

Date occupied: 16 April 1995

Date departed: 16 April 1995

Time on hole: 08 hr, 15 min

Position: 33°50.475′N, 24°52.962′E

Bottom felt (drill-pipe measurement from rig floor, m): 2210.0

Distance between rig floor and sea level (m): 11.5

Water depth (drill-pipe measurement from sea level, m): 2198.5

Total depth (from rig floor, m): 2229.0

Penetration (m): 19.0

Number of cores (including cores having no recovery): 2

Total length of cored section (m): 19.0

Total core recovered (m): 19.5

Core recovery (%): 102.4

Oldest sediment cored:
Depth (mbsf): 19.00
Nature: nannofossil ooze
Earliest age: Pleistocene
Measured velocity (km/s): 1.5

Principal results: Six holes were cored at Site 969 to a maximum depth of 116 mbsf and recovered sediments ranging from the uppermost Miocene(?)/lowermost Pliocene to the Holocene. They consist of nannofossil ooze and nannofossil clay with sapropels of earliest Pliocene (MPL1) to Holocene age and unconformably overlie calcareous silty clay of indeterminate age. Holes 969A, 969B, and 969C contain locally faulted and thinned sedimentary sequences; Hole 969D recovered a tilted sequence containing small reverse faults. This hole appears to have yielded a more complete sedimentary sequence than the others, which contain numerous normal faults. The average sedimentation rate was 22 m/m.y.

More than 80 sapropels were recovered from the lower Pliocene through Holocene section at Site 969. The sapropels occur in five distinct groups, which are separated by intervals of sediment that are commonly oxidized, are yellowish brown in color, and have no preserved sapropels. The darkest black sapropels, of middle Pliocene age, contain up to 30% organic carbon. The clay-rich unit at the base of the recovered sequence contained no age-diagnostic taxa and yielded only reworked marine specimens and ostracodes indicative of brackish water. Pore-water concentrations of dissolved ions imply that solutions characteristic of late-stage brine, possibly derived from dissolving evaporites at depth, are present below the cored sediment interval.

BACKGROUND AND OBJECTIVES

Site 969 is located on the Mediterranean Ridge in water 2200 m deep (Fig. 1; see "Geological Setting" section, this chapter). The location was chosen to recover a sedimentary record of sapropel formation on the ridge that separates the Ionian Basin in the west from the Levantine Basin in the east. It is the central tie point of a longitudinal and depth transect across the Mediterranean Sea (ODP Legs 160 and 161) and will help constrain environmental gradients (salinity, temperature, nutrients) and their chemical and paleontological expressions. The site is close (60 nmi) to the Pliocene land sections in southern Crete, where extensive work on the stratigraphy of sapropels has been conducted (e.g., Spaak, 1982).

Penetration at Site 969 was limited to refusal of the APC tool because of safety concerns. It was estimated from the pre-site survey that the thickness of the Pliocene to Holocene sediment was approximately 120 m (0.13 s two-way traveltime [TWT]) and the record at Site 969 was expected to extend to the lowermost Pliocene and possibly to the uppermost Miocene.

Our principal objective was to construct a composite sediment section of Pliocene to Holocene age by repeated coring and detailed interhole correlation of the lithology and physical properties. Initial shipboard stratigraphy, based on biostratigraphic and magnetostratigraphic investigations, was to assess if the sequence is complete and will be augmented by detailed work in shore-based studies, as well as by additional stratigraphic information from isotope studies and tephrochronology. The goal is to establish a detailed age model, which can be linked to the other sites drilled during Leg 160 and to the orbitally tuned stratigraphic record from land sections. A subsidiary goal was to recover a well-developed lower Pliocene sequence to study the transition from the Messinian evaporite facies to fully marine conditions at the Miocene/Pliocene boundary.

GEOLOGICAL SETTING

Site 969 is sited on the Mediterranean Ridge about 100 km south of the island of Crete. The following summary is based on recent synopses by Cita and Limonov (1993) and by Cita and Camerlenghi (1990) and is included for background information, although the ob-

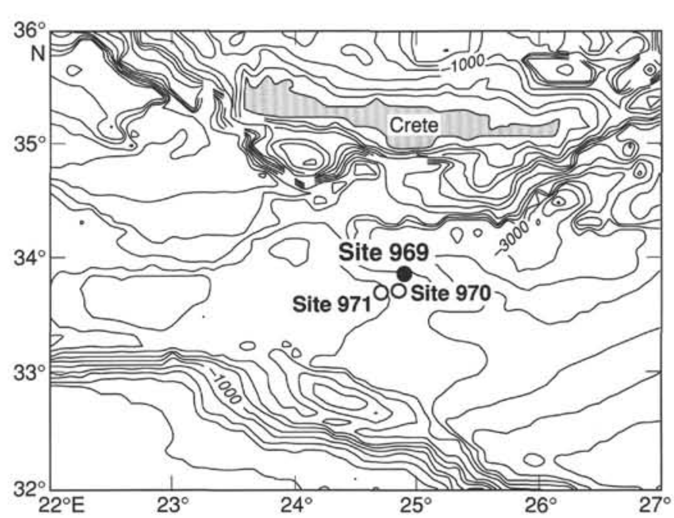

Figure 1. Location map of Site 969 on the Mediterranean Ridge. The bathymetry is from the ETOPO5 data set.

jectives of this site were mainly paleoceanographic. The Mediterranean Ridge is approximately 150 km wide and stretches from the Calabrian Ridge in the west (including Site 964) as far as the Florence Rise in the east, a distance of approximately 1500 km (see "Tectonic Introduction" chapter, this volume; Cita and Limonov, 1993). The southern margin of the Mediterranean Ridge is bounded by elongate, flat abyssal plains, which increase in depth from east to west: the Ionian (or Messina) Abyssal Plain, Sirte Abyssal Plain, and Herodotus Abyssal Plain, respectively. Directly south of Crete, and to the south of Site 969, the abyssal plain decreases in width to a narrow trough, and in this area a northward-protruding segment of the North African continental margin is in the initial stages of collision with the leading edge of the Mediterranean Ridge.

The average depth of the Mediterranean Ridge is approximately 2.1–2.2 km, and its depth varies between 1200 m and more than 3000 m. The topography is characterized by small closely spaced depressions and ridges (with a relief of 50–100 m and a wavelength of 0.5–2 km), oriented mostly parallel to the overall trend of the ridge. The pattern gives rise to well-known hummocky acoustic reflections known as cobblestone topography (Hersey, 1965) when using standard echo-sounding devices.

The Mediterranean Ridge was initially seen as a component of the Alpine mountain system of Miocene age (Giermann, 1969). With the advent of plate tectonic theory, the Mediterranean Ridge was recognized as related to a plate boundary between the African and Eurasian plates; however, the active margin was initially seen as located to the north of the ridge, in view of the existence of the Hellenic "trench" in this direction. Accordingly, the Mediterranean Ridge was seen as the result of lithospheric downflexure to the south of the downgoing slab (Stride et al., 1977; Hsü, Ryan, et al., 1973). The current interpretation is that the Mediterranean Ridge is a subduction complex formed by offscraping of sediments from the downgoing slab; this concept was first put forward by Dewey et al. (1973), and has since been validated by numerous studies.

Le Pichon (1982) argued, based on geophysical data, that the lower part of the thick sediment pile has been subducted, while the upper part was detached and incorporated into an accretionary wedge (Fig. 2). Ryan et al. (1982) hypothesized that the décollement becomes increasingly deep away from the frontal zone of detachment, down to an Aptian age toward the north. The Hellenic Trench was then reinterpreted as a fault-controlled forearc basin. Side-scan sonar and other studies have provided much evidence concerning the structure of the Mediterranean Ridge (Belderson et al., 1972). In addition, detailed seismic studies have imaged the most southerly extension of the accretionary wedge (e.g., Finetti, 1982; J. Mascle, pers. comm., 1994). The structural style of the Mediterranean Ridge has also recently become better known through detailed bathymetric and piston coring studies (Kastens et al., 1992).

One unusual feature of the Mediterranean Ridge is that the southern part is more elevated than the northern part. In other areas, the toe of the wedge is typically at a low topographic level and is uplifted to progressively higher levels across the arc-trench gap. The discrepancy in this case is explained by the accretion of thick sediments of the North African continental margin to the wedge, in contrast to an earlier phase when thinner, more distal sediments were incorporated into the wedge.

Another unusual feature of the Mediterranean Ridge is the presence of Messinian evaporites at a depth of 100–400 m. In addition, Messinian evaporites may have been incorporated into the accretionary wedge and may influence its rheological behavior and structure at depth. Also, their existence influences pore-water chemistry and diagenetic sediment reactions. One peculiar feature is that small anoxic basins are located on the upper part of the ridge, and these have been locally permeated with deep-derived brines (Cita et al., 1986).

Recently, the deep structure of the Mediterranean Ridge has become better known through the acquisition of deep seismic data and gravity modeling (Truffert et al., 1993). The possible history of the ridge has also been inferred from indirect lines of evidence (Kastens, 1991). However, considering its obvious importance, startlingly little is still known about the tectonic history of the Mediterranean Ridge. The presence of Messinian evaporites has greatly hampered progress, both by impeding seismic investigation and by giving rise to a perceived safety hazard for ODP drilling. The present coring at Site 969 was intended to recover only the Pliocene-Pleistocene section and was not expected to yield any significant evidence of the tectonic evolution of the Mediterranean Ridge.

OPERATIONS

Transit to Site 969

The 385-nmi transit to Site 969 (proposed Site MEDSAP-2D) required 31.8 hr at an average speed of 12.1 kt. A 15.6-nmi seismic survey was run over Site 969 in 2.6 hr at 6.0 kt. A Datasonics 354M beacon (S/N 799, 15.0 kHz) was deployed at 1300 hr on 14 April.

Hole 969A

The same APC/XCB BHA used at the previous sites was run, and Hole 969A was spudded at 1800 hr on 14 April. The estimated seafloor depth was at 2200.3 m by drill-pipe measurement (DPM). APC Cores 160-969A-1H through 13H were taken from 0 to 108.3 mbsf (Table 1), with 108.3 m cored and 111.43 m recovered (102.9% recovery). Cores were oriented from Core 160-969A-3H. ADARA heat-flow measurements were taken on Cores 160-969A-5H, 7H, and 9H. Six of the last seven cores were partial strokes, and coring was terminated when Core 160-969A-11H had an imploded top and the core liner had to be pumped out on Core 160-969A-12H. The maximum gas detected was 4 ppm methane. Some core separation occurred as a result of gas expansion.

Hole 969B

The ship was moved 190 m to the northwest of the beacon, and Hole 969B was spudded at 0620 hr on 15 April. A seafloor depth of 2202.1 m DPM was indicated. APC Cores 160-969B-1H through 11H were taken from 0 to 97.9 mbsf (Table 1), with 97.9 m cored and 100.2 m recovered (102.3% recovery). The bit cleared the seafloor at 1540 hr on 15 April.

Hole 969C

The ship was moved 175 m southwest of the beacon, and Hole 969C was spudded at 1720 hr on 15 April. A seafloor depth of 2195.5 m DPM was indicated. APC Core 160-969C-1H was taken from 0 to 9.5 mbsf, with 9.5 m cored and 9.98 m recovered (105.1% recovery). The top of the core appeared to be about 3 m below the seafloor, and the hole was abandoned for that reason. The bit cleared the seafloor at 1745 hr on 15 April.

Hole 969D

Hole 969D was spudded in the same position as Hole 969C at 1720 hr on 15 April. A seafloor depth of 2192.1 m DPM was indicated. APC Cores 160-969D-1H through 13H were taken from 0 to 116.2 mbsf (Table 1), with 115.7 m cored and 118.54 m recovered (102.5% recovery). The bit cleared the seafloor at 0555 hr on 15 April.

Hole 969E

The ship was moved 170 m north of the beacon (5 m south of Hole 969B), and Hole 969E was spudded at 0655 hr on 16 April. A seafloor depth of 2201.1 m was indicated. APC Cores 160-969E-1H

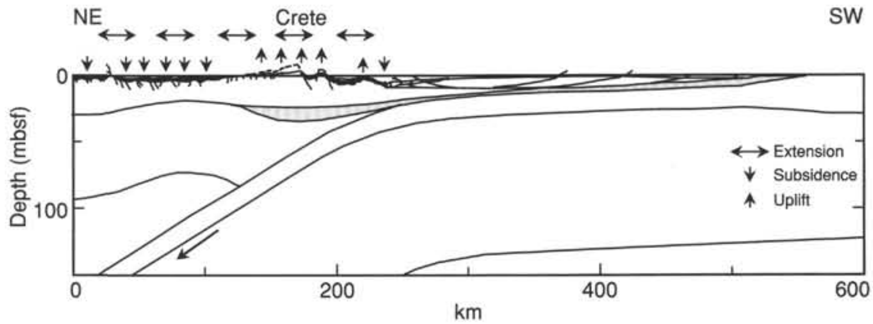

Figure 2. True-scale cross section of the Mediterranean Ridge from the Aegean Sea to the Libyan continental margin to the south. Note the inferred accreted slices within the accretionary wedge. The position of the Hellenic Trench is shown by the black arrow. The upward-pointing arrows show the uplift of Crete related to subduction and underplating. After Le Pichon (1982).

through 11H were taken from 0 to 97.9 mbsf (Table 1), with 97.9 m cored and 100.23 m recovered (102.4% recovery). The liner imploded or failed on four of the last five cores. Coring was terminated when the formation got extremely firm while drilling for Core 160-969-12H. The bit cleared the seafloor at 1520 hr on 16 April.

Hole 969F

The ship was moved 10 m south of Hole 969E, and Hole 969F was spudded at 1615 hr on 16 April. A seafloor depth of 2198.5 m DPM was indicated. APC Cores 160-969F-1H and 2H were taken from 0 to 19.0 mbsf (Table 1), with 19.0 m cored and 19.46 m recovered (102.4% recovery). The bit cleared the rotary table at 2306 hr, and the rig floor was secured for sea voyage at 2324 hr on 16 April. The beacon was recovered.

SITE GEOPHYSICS

Site 969 is situated on the inner, shallower part of the Mediterranean Ridge and is therefore in a region of intense deformation. The site was chosen because it is in a relatively undeformed area, with what appeared to be an expanded Pliocene-Pleistocene section that could be expected to contain as full as possible a record of sapropel layers (see "Geological Setting" section, this chapter). It was first identified during a 1989 cruise of the *Bannock* and further examined during a 1993 survey by *Gelendzhik* using high-resolution seismic methods, coring, and both long-range and deep-tow side-scan sonar observations (Limonov et al., 1994). The site survey conducted prior to drilling duplicated sections of the *Gelendzhik* survey lines crossing the site at right angles (Fig. 3).

The southeast to northwest seismic line (Fig. 4) crossed a slightly disturbed region first and then a previously observed deeper pond of generally flat-lying but northwestward-deepening sediments. The signal characteristics of the seismic system on *JOIDES Resolution* (see "Explanatory Notes" chapter, this volume) prevent the resolution of detail in the upper sediments; however, it is possible from signal interference effects to infer a low-amplitude, horizontal, continuous reflector at about 130 ms sub-bottom TWT, followed at a depth below seafloor of about 180 to 200 ms TWT by a stronger reflector that varies in strength and has small-amplitude undulations along the line. Below this upper section lie a medium-strength discontinuous horizontal reflector at about 260 ms TWT below seafloor, a gently northwestward-dipping and very discontinuous medium- to strong-amplitude reflector at about 320 ms TWT below seafloor, and a deeper reflector at about 400 to 450 ms TWT below seafloor, which appears to be the base of the small sediment pond. The deeper reflector shallows by more than 100 ms about 700 m southeast of the site, where the deformed section of sediment was observed.

The line run from southwest to northeast across the site displays a similar picture, with relatively undeformed sediment to the southwest and deformed sediment to the northeast (Fig. 5); however, the appearance of some of the reflectors is different in this line. The site appears to be situated where there is some subsurface deformation. The vague indication of a reflector at a depth of about 130 ms TWT below seafloor is part of a general, but still poorly imaged, uneven reflector within the upper sedimentary unit (assumed previously, for example, by Limonov et al., 1994, to be post-Miocene). The strong assumed Messinian reflector is clearly observed southwest of the site at a sub-bottom depth of 150 to 175 ms, but it is poorly seen at the site because of the presence of diffractions. The diffractions are associated with a break in the lower sedimentary units below the site, and to the east, the reflectors are more deformed as indicated by the presence of diffractions.

Poor definition of reflectors observed on the southeast to northwest line in comparison to the cross line could be explained by assuming that the southeast to northwest line roughly ran along a zone of deformation observed more clearly on the cross line. The nature of the disturbance in the sedimentary section is difficult to interpret. It does not appear to be the result of simple folding, which is common nearby. It could be the result of faulting, but the reflectors do not appear to be offset across it. It looks more like a small collapse feature similar to others inferred in the vicinity from site-survey deep-tow side-scan sonar data. There is a downturn in the reflector below the upper sedimentary unit (from about 150 to 200 ms TWT below seafloor), which is not likely the result of either diffraction or velocity effects. Within the disturbed zone, there is evidence at about 3.25 s TWT that the intermediate sedimentary unit giving the strong reflection at 3.2 s TWT is both downfaulted and tilted to the southwest. Such deformation might be expected if there has been some salt diapirism and dissolution or if there had been an early phase of mud diapirism that is now buried. Along the southwest to northeast line, the appearance of the second seismic unit (between about 3.1 and 3.2 s TWT in the seismic profile in Fig. 5) is similar to that of a thin Messinian evaporitic interval; this situation would not be contrary to the general assumption that only a very thin evaporitic unit could have been deposited high on the Mediterranean Ridge.

LITHOSTRATIGRAPHY

The sedimentary sequence recovered from six holes at Site 969 consists of a 97- to 116.2-m-thick, early Pliocene to Holocene age section of foraminifer nannofossil ooze, nannofossil ooze, and nannofossil clay with sapropels (Unit I). These sediments overlie calcareous silty clays of indeterminate age (Unit II), of which a total of 5.45 m was recovered. Within Unit I, intervals of predominantly gray sediment with sapropels alternate with intervals of reddish brown sedi-

Table 1. Coring summary for Site 969.

Core	Date (April 1995)	Time (UTC)	Depth (mbsf)	Length cored (m)	Length recovered (m)	Recovery (%)
160-969A-						
1H	14	1615	0.0–7.7	7.7	7.68	99.7
2H	14	1700	7.7–17.2	9.5	9.84	103.0
3H	14	1750	17.2–26.7	9.5	9.85	103.0
4H	14	1840	26.7–36.2	9.5	9.80	103.0
5H	14	1940	36.2–45.7	9.5	9.98	105.0
6H	14	2025	45.7–55.2	9.5	9.69	102.0
7H	14	2130	55.2–64.7	9.5	9.29	97.8
8H	14	2210	64.7–74.2	9.5	10.01	105.3
9H	14	2320	74.2–83.7	9.5	10.10	106.3
10H	14	2355	83.7–93.2	9.5	9.66	101.0
11H	15	0035	93.2–102.7	9.5	9.94	104.0
12H	15	0120	102.7–105.5	2.8	2.75	98.2
13H	15	0225	105.5–108.3	2.8	2.83	101.0
Coring totals:				108.3	111.4	102.9
160-969B-						
1H	15	0435	0.0–2.9	2.9	2.90	100.0
2H	15	0520	2.9–12.4	9.5	9.86	104.0
3H	15	0555	12.4–21.9	9.5	9.77	103.0
4H	15	0640	21.9–31.4	9.5	9.85	103.0
5H	15	0720	31.4–40.9	9.5	9.88	104.0
6H	15	0755	40.9–50.4	9.5	9.86	104.0
7H	15	0835	50.4–59.9	9.5	9.66	101.0
8H	15	0915	59.9–69.4	9.5	8.82	92.8
9H	15	0950	69.4–78.9	9.5	9.72	102.0
10H	15	1045	78.9–88.4	9.5	9.87	104.0
11H	15	1235	88.4–97.9	9.5	9.97	105.0
Coring totals:				97.9	100.2	102.3
160-969C-						
1H	15	1535	0.0–9.5	9.5	9.98	105.1
Coring totals:				9.5	10.0	105.1
160-969D-						
1H	15	1610	0.0–8.9	8.9	8.87	99.6
2H	15	1645	8.9–18.4	9.5	9.87	104.0
3H	15	1735	18.4–27.9	9.5	9.92	104.0
4H	15	1815	27.9–37.4	9.5	9.82	103.0
5H	15	1855	37.4–46.9	9.5	9.70	102.0
6H	15	1940	46.9–56.4	9.5	9.79	103.0
7H	15	2025	56.4–65.9	9.0	9.21	96.0
8H	15	2110	65.9–75.4	9.5	9.78	103.0
9H	15	2155	75.4–84.9	9.5	9.64	101.0
10H	15	2240	84.9–94.4	9.5	10.03	105.6
11H	15	2330	94.4–103.9	9.5	9.67	102.0
12H	16	0125	103.9–112.0	8.1	8.08	99.7
13H	16	0220	112.0–116.2	4.2	4.16	99.0
Coring totals:				115.7	118.5	102.5
160-969E-						
1H	16	0510	0.0–4.9	4.9	4.92	100.0
2H	16	0540	4.9–14.4	9.5	9.88	104.0
3H	16	0605	14.4–23.9	9.5	9.85	103.0
4H	16	0700	23.9–33.4	9.5	9.91	104.0
5H	16	0740	33.4–42.9	9.5	9.81	103.0
6H	16	0815	42.9–52.4	9.5	9.92	104.0
7H	16	0900	52.4–61.9	9.5	9.46	99.6
8H	16	0935	61.9–71.4	9.5	9.79	103.0
9H	16	1020	71.4–80.9	9.5	9.18	96.6
10H	16	1105	80.9–88.4	7.5	7.38	98.4
11H	16	1155	88.4–97.9	9.5	10.13	106.6
Coring totals:				97.9	100.2	102.4
160-969F-						
1H	16	1430	0.0–9.5	9.5	9.62	101.0
2H	16	1510	9.5–19.0	9.5	9.84	103.0
Coring totals:				19.0	19.5	102.4

ment without sapropels. The sequences recovered from the deeper holes were all affected to a varying extent by faulting and tilting, which has resulted in localized difficulties in interhole correlation. Because of differences among the holes, the lithostratigraphic summary for Holes 969A, 969B, 969C, 969E, and 969F (Fig. 6A) is presented separately from that of Hole 969D (Fig. 6B).

Criteria employed in lithostratigraphic description and classification at Site 969 included (1) visual observation of color; (2) visual observation of sedimentary structures, including bioturbation; (3) smear-slide examination; (4) color reflectance spectrophotometry measurements; (5) carbonate and organic carbon determinations; and (6) X-ray diffraction (XRD) analysis.

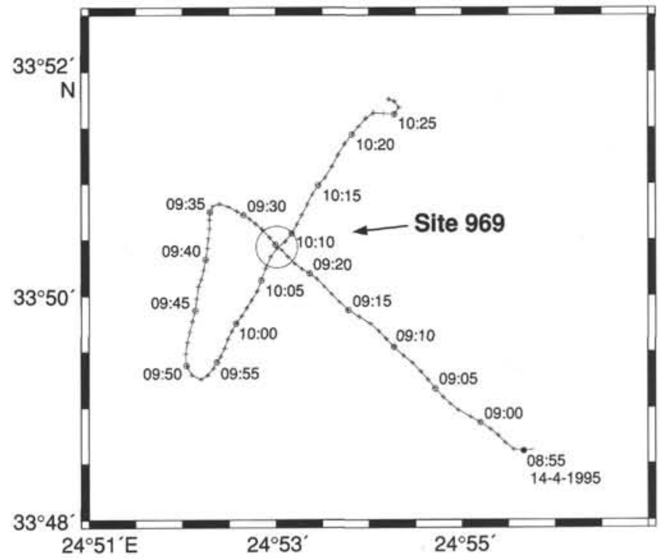

Figure 3. The ship's track during the predrilling survey for Site 969.

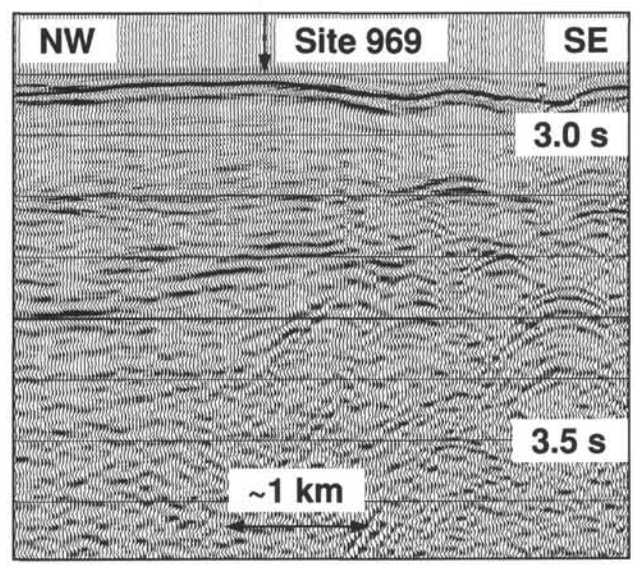

Figure 4. Southeast to northwest seismic profile across Site 969. Horizontal lines are every 100 ms.

Color Reflectance

Color scanning was performed at 2-cm intervals. The color intensity provided an excellent record of sapropel occurrence and this record was used in attempts to aid interhole correlation and compile a composite section (see "Composite Depths" section, this chapter). Distinctive intervals of yellowish brown sediment are well developed at Site 969. The intervals show up particularly well on the a* color axis as strongly reflective in the red part of the spectrum, and they were also used in interhole correlation (Fig. 6B). In addition, these intervals of red sediment correlate well with equivalent stratigraphic layers at Site 967.

Description of Lithostratigraphic Units

Lithostratigraphic Unit I

Description: Nannofossil ooze, clayey nannofossil ooze, foraminifer nannofossil ooze, and nannofossil clay

Intervals: Sections 160-969A-1H-1 through 12H-1, 13 cm, 160-969B-1H-1 through 11H-6, 125 cm, Core 160-969C-1H, 160-969D-1H through 13H, Sections 160-969E-1H-1 through 11H-6, 22 cm, and Cores 160-969F-1H and 2H
Depth: 0–102.83 mbsf, Hole 969A; 0–97.15 mbsf, Hole 969B; 0–9.5 mbsf, Hole 969C; 0–116.2 mbsf, Hole 969D; 0–96.12 mbsf, Hole 969E; 0–19 mbsf, Hole 969F
Age: early Pliocene to Holocene

The lithology of Unit I is predominantly nannofossil ooze, clayey nannofossil ooze, and foraminifer nannofossil ooze with minor intervals of nannofossil clay. The composition of the dominant lithology, according to smear-slide analysis, is commonly about 70% nannofossils, 10% foraminifers, and 10%–20% clay and terrigenous silt, with varying amounts of nannofossils (30%–80%), foraminifers (5%–30%), and clay (0%–70%) (Fig. 7). The composition of the carbonate component in the sediment, as determined by XRD analysis, is a mixture of low- and high-magnesium calcite within the top 20 m that changes to normal low-magnesium calcite below.

The topmost 2.5 m of sediment is very pale brown (10YR 7/4) nannofossil ooze (above sapropel S1), grading to a clayey nannofossil ooze below. Thereafter, the upper 20–25 m of sediment (all holes) comprises clayey nannofossil ooze and foraminifer clayey nannofossil ooze that is color banded from light gray (10YR 7/1) and gray (5Y 6/1) to light yellowish brown (10YR 7/4) on a decimeter to meter scale. Three distinctive ash layers occur in the upper few meters. The most notable of these is a 13-cm-thick bed with a prominent altered base that occurs above sapropel S3 (Fig. 8).

Below 20–25 mbsf, two main contrasting facies types occur that may be identified on the basis of sediment color and the presence or absence of sapropels. The more common facies comprises light gray to gray foraminifer clayey nannofossil ooze with sapropels. Within this sediment, between about 8 and 35 mbsf (Hole 969A) slightly darker, 5–10-cm-scale, more clay-rich interbeds are present (Fig. 9). The second facies comprises clayey nannofossil ooze that contains traces of hematite and is color banded on a decimeter to meter scale in various hues, from very pale brown (10YR 7/3) to reddish brown (5YR 5/4). Although there appears to be little difference in bulk sediment composition, the red intervals are characterized by trace quantities of hematite throughout, and the gray sediment by variable (trace–5%) pyrite. Small pyrite nodules are also present in the reduced sediment. Meter-scale, pale-dark color banding within the red sediment highlights burrow fabrics (Fig. 10). The red intervals contain sporadic, decimeter-scale interbeds of relatively more clay-rich, gray to grayish brown (5Y 5/1 to 10Y 5/2) nannofossil clay that are relatively enriched in hematite and opaque minerals (Fig. 11). The lowest interval of light gray sediment containing sapropels (of early Pliocene age) has an elevated clay content.

Contact with Unit II

The contact between Unit I and Unit II was recovered in Holes 969A (102.83 mbsf), 969B (97.15 mbsf), and 969E (96.12 mbsf). In Hole 969B, the consolidated, stiff, calcareous clays of Unit II (below) are overlain along an undeformed contact by dark gray to dark olive gray foraminifer nannofossil ooze. The basal sediments of Unit I are relatively dark and strongly laminated (Fig. 12). In Holes 969A and 969E, the contact is deformed by microfaults and overlain by a sheared sapropel (Hole 969E) (Fig. 13).

Lithostratigraphic Unit II

Description: Calcareous clay
Intervals: Sections 160-969A-12H-1, 13 cm, through 13H-CC, 160-969B-11H-6, 125 cm, through 11H-CC, and 160-969E-11H-6, 22 cm, through 11H-CC
Depth: 102.83–108.3 mbsf, Hole 969A; 97.15–97.9 mbsf, Hole 969B; 96.12–97.9 mbsf, Hole 969E
Age: unknown

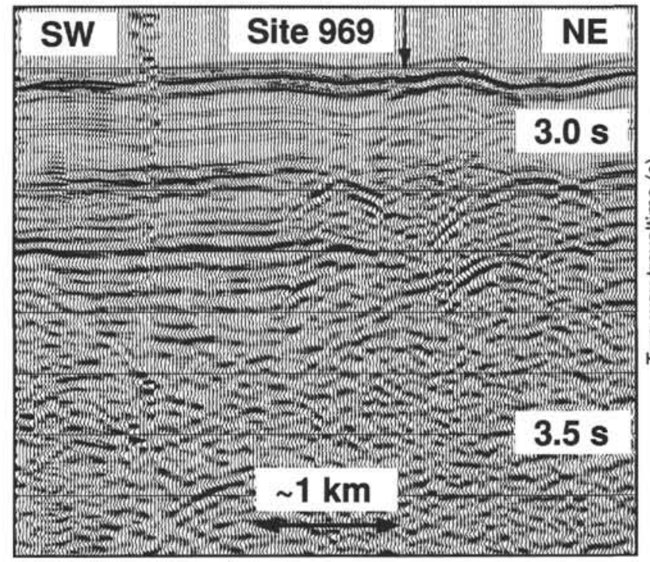

Figure 5. Southwest to northeast seismic profile across Site 969. Horizontal lines are every 100 ms.

The sediments of Unit II are composed of a uniform dark greenish gray (5GY 4/1) calcareous clay. Calcareous nannofossils present in low abundances (10%–20%) in the upper meter of core are, in part, reworked Cretaceous floras and partly non-age-diagnostic assemblages that span the late Miocene–early Pliocene time interval (see "Biostratigraphy and Sedimentation Rates" section, this chapter). Below this, the carbonate fraction is made up exclusively of calcite (typically 5–20 µm in size) with rare dolomite. In the most extensive (5.45 m) section recovered within Hole 969A, very thin (1–5 mm) beds and laminae of very fine silt-grade calcite are intercalated toward the base. The texture of these grains includes the characteristic rice-grain type observed in similar stratigraphic levels within Unit II at Site 968 and in Unit I at Site 965.

Sapropels

More than 80 sapropels were recovered from the upper Pliocene through Holocene section at Site 969. These occur in five distinct groups separated by intervals of sediment that are commonly oxidized and yellowish brown in color with no preserved sapropels (see above). From smear-slide analysis, the composition of the sapropels generally resembles the surrounding dominant lithology but contains, in addition, organic matter and pyrite. However, some layers or laminae within the sapropels appear particularly rich in calcareous nannofossils.

The upper group of sapropels contains the typical upper Pleistocene sequence with S1, S3, S4, S5, S6, and S7 all present (Fig. 14). They are generally dark gray (5Y 4/1) or very dark gray (5Y 3/1) in color. The thicker beds are laminated, mainly in their basal part (Fig. 15), although S5 shows distinctive laminations in the upper part (Fig. 16). In addition, there are several ash layers, including a distinctive 13-cm-thick layer with an altered base above S3 (Fig. 8). The lowest bed within this upper group is an oxidized sapropel that occurs between 8.5 and 8.1 mbsf (Holes 969A, 969B, and 969E) (Fig. 17).

In the uppermost Pliocene to lower Pleistocene sequence, between 19.3 and 36 mbsf (Hole 969A; 18–34 mbsf, Hole 969B; 16.5–34 mbsf, Hole 969E), sapropels are severely affected by shearing and several appear to be faulted out of the sequence (Fig. 18A, B). In contrast, in Hole 969D, this sequence is relatively expanded and contains beds in excess of 25 cm thick (Fig. 19). Some of the sapropels within top part of the uppermost Pliocene through lower Pleistocene sequence are, unusually, burrowed by *Zoophycos* (Fig. 20). Shipboard

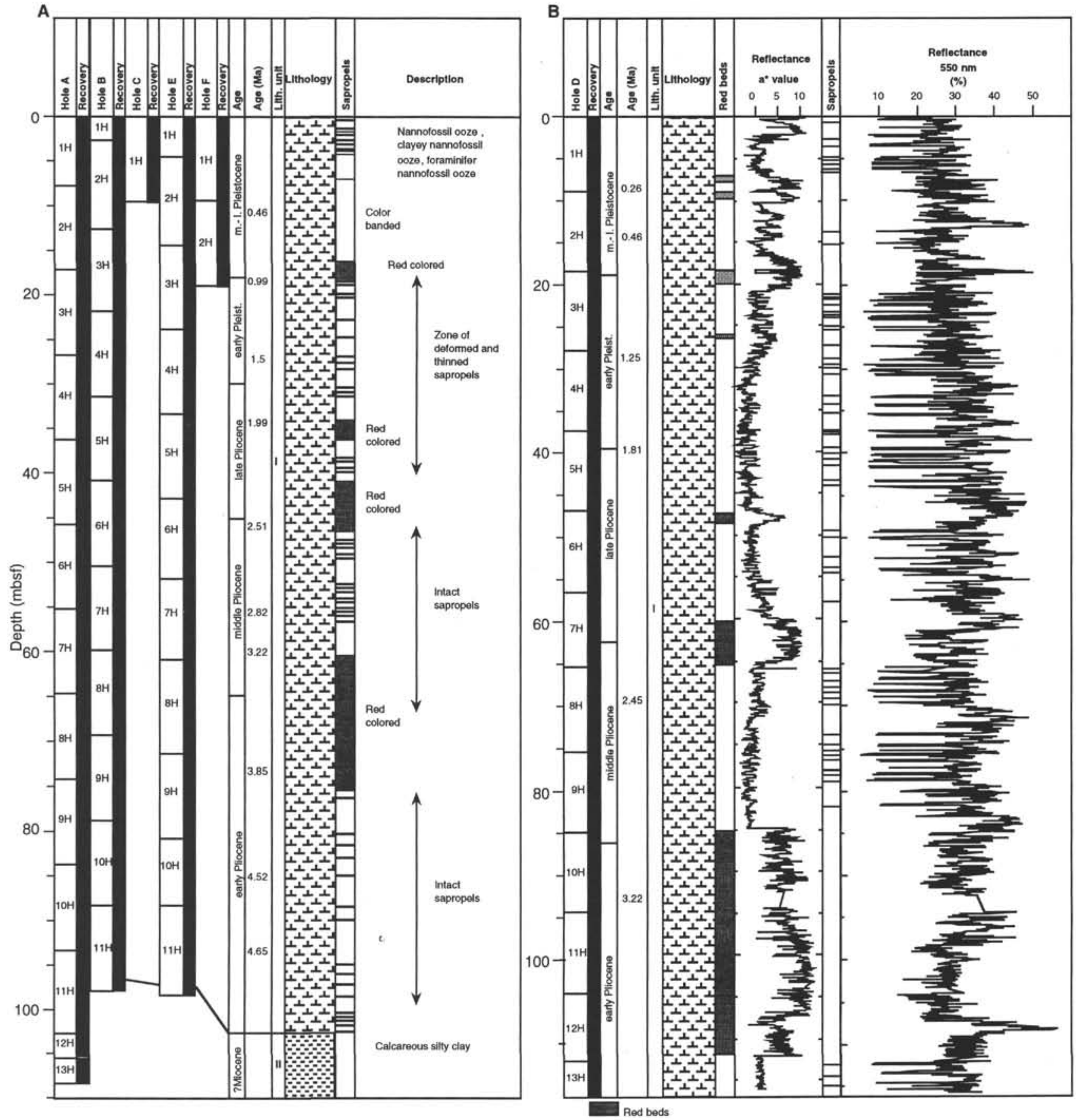

Figure 6. Core recovery, age, and lithostratigraphic summary for Site 969. **A.** Holes 969A, 969B, 969C, 969E, and 969F. **B.** Hole 969D. The column for the location of red beds indicates intervals where the sediment ranges from light brown (10YR 6/3) to reddish brown (5YR 5/4). Color reflectance a* values greater than zero indicate a red chroma.

organic carbon determinations through this interval (taken from Hole 969A) record maximum values of 17.6% TOC, with a more usual range of 2%–10%.

Two distinctive groups or packets of predominantly black (5Y 2.5/1) sapropels occur in a gray-colored interval of middle Pliocene age (Fig. 21). These sapropels may be correlated bed-by-bed among all holes at Site 969 (although some beds are missing within coring gaps). Individual beds were recognized on the basis of color, internal subdivisions, location, and intensity and type (trace fossils) of bioturbation, as well as relative spacing with other beds within the packet. Individual beds tend to possess the same distinctive features in all holes. For example, the basal two beds of the second middle Pliocene sapropel packet contain *Chondrites* burrows only in the lower part of the bed (Fig. 22). Although not obviously laminated from the visual core description, these highly organic-rich beds (up to 30.5% TOC) appear to have a bed-parallel fissility that may correspond to primary lamination.

Within the lowest group of sapropels (of early Pliocene age), beds are commonly burrowed throughout in their upper part by *Chondrites* and are not as dark colored as the middle and upper Pliocene beds, varying from dark gray and dark grayish brown (10YR 4/1, 10YR 4/2) through very dark gray (10YR 3/1) and only rarely, dark grayish

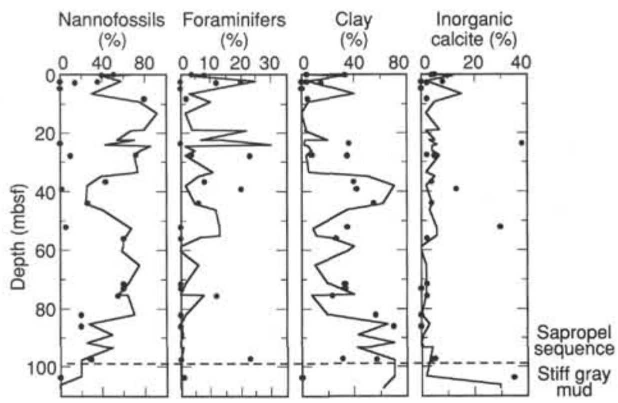

Figure 7. Major sediment components from smear-slide analysis of Holes 969A and 969B for both dominant (line) and minor (points) lithologies.

brown (10YR 3/2). Organic carbon percentages are correspondingly relatively low, varying from 2.25% to 5%. The basal Pliocene sapropel that lies on the calcareous clays of Unit II (observed only at Section 160-969B-11H-6, 30–125 cm) is a compound bed of olive gray (5Y 5/2), intermittently laminated foraminifer nannofossil ooze that contains two internal layers of dark gray (5Y 4/1) sediment (Fig. 12). This bed may, in part, be the equivalent of the "mystery sapropel" described from the Florentine Basin site of DSDP Leg 42 (Hsü, Montadert, et al., 1978).

Interhole Correlation and Development of a Composite Section

In order to provide a stratigraphic correlation among the holes at Site 969, distinctive lithologic markers were identified in all holes. The sedimentological characteristics and position of each sapropel were recorded, as were the position and composition of the more distinctive ash layers. A check on the visual correlation was provided by color-scanner data (see "Color Reflectance" section, above); reference was also made to selected MST data, including magnetic susceptibility.

Discrepancies in the number of sapropels recovered in the various holes can be attributed to (1) the presence of gaps in coring between successive cores (see "Composite Depths" section, this chapter) and (2) attenuation of the sequences by extensional soft-sediment faulting (see "Structural Geology" section, this chapter, and below). Discrepancies were also found in the thickness of the sapropels owing either to thinning or removal by faulting or to an increase in the apparent thickness of sapropels within intervals with gentle to moderate dips (apparent dips progressively increase from values of about 10° [Core 160-969D-5H] to about 45° at the base of the hole).

Holes 969A, 969B, and 969E

In comparing the sequences obtained from different holes, systematic depth-related differences occurred in the extent to which the sapropels could be correlated. The upper Pleistocene sapropel sequence (0–8.5 mbsf, Holes 969A, 969B, and 969D) correlates well (Fig. 23). However, in the uppermost Pliocene to lower Pleistocene sequence, between 19.3 and 36 mbsf (Hole 969A; 18–34 mbsf, Hole 969B; 16.5–34 mbsf, Hole 969E), many of the sapropels present appear partly sheared or cut out by faulting (Fig. 18A, B). Below 44 mbsf (all holes), the middle Pliocene sapropels are undeformed and may be entirely correlated among the holes (see below). In the lower Pliocene section, correlation between sapropels is also difficult, probably in part owing to faulting, but exacerbated by pull-out effects produced during piston coring that affect the middle of cores as well as the last sections (e.g., Cores 160-969B-10H and 11H and 160-969A-11H).

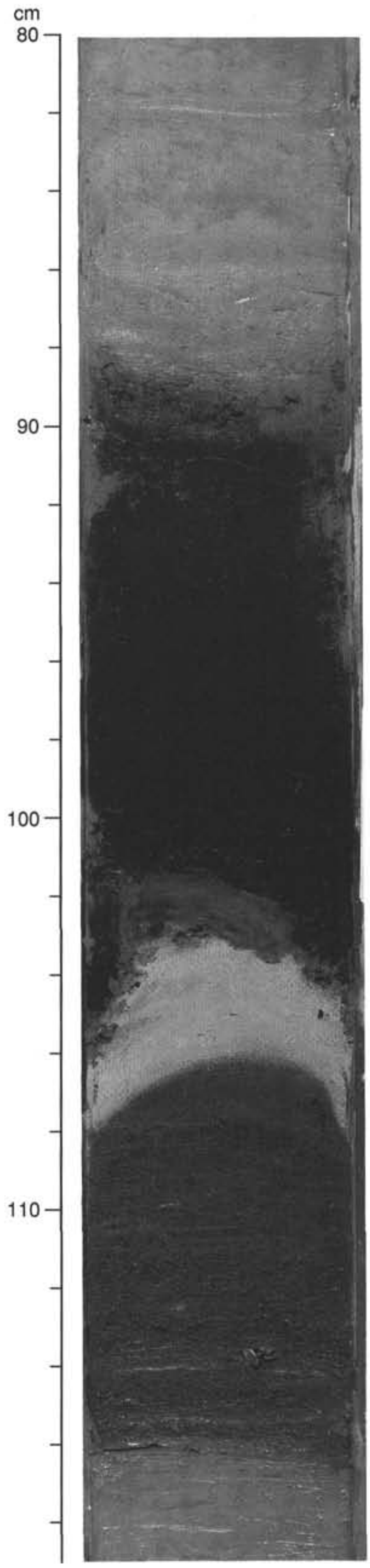

Figure 8. A distinctive thick (10 cm) ash layer immediately above sapropel S3 (Section 160-969A-1H-2, 80–119 cm). Note the altered base.

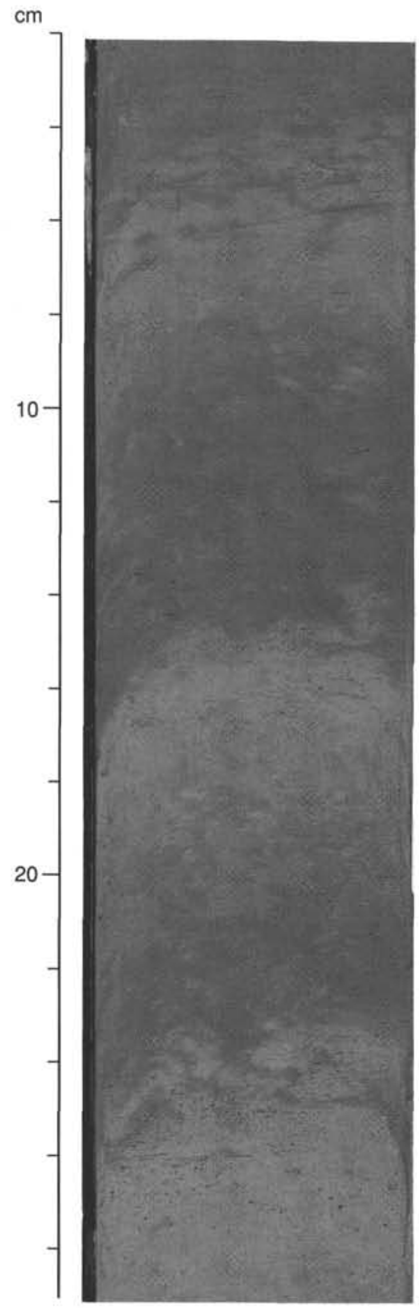

Figure 9. Color-graded, 5–10-cm-scale, darker, clay-rich beds within Unit I (Section 160-969A-4H-4, 2–29 cm). These may represent the deposits of low-density turbidity currents.

Hole 969D

In contrast to those of Holes 969A, 969B, and 969E, the sapropels recovered from Hole 969D (Table 2) are consistently intact and undeformed. The upper Pleistocene sapropel sequence is somewhat thinner, ending at 6.5 mbsf (compared with 8.1–8.5 mbsf). The upper Pliocene to lower Pliocene sequence contains 31 undeformed sapropels in 40 m of sediment: a thickness and number comparable to the equivalent sections at other sites. The two middle Pliocene sapropel packets are also present, and appear thicker owing to a moderate dip of the beds.

A complete list of all sapropels recovered at Site 969 is shown in Table 3, and the stratigraphic correlation, taken as far as was possible

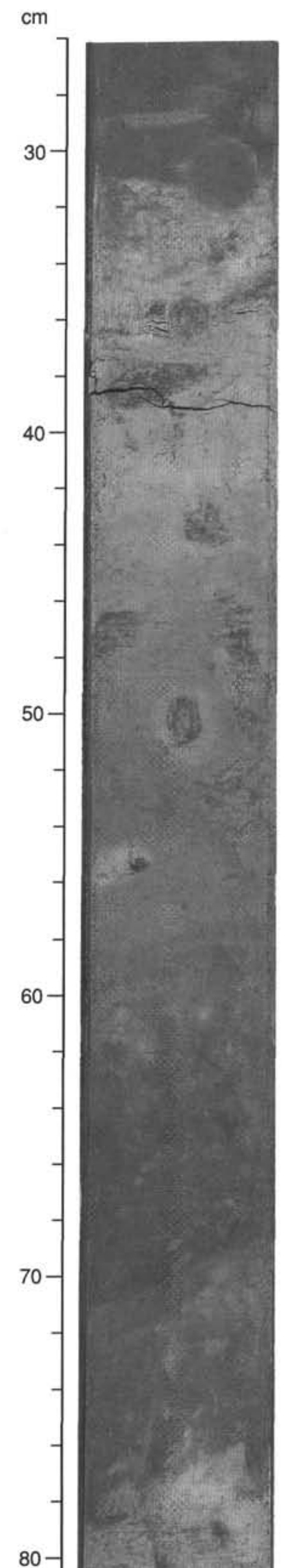

Figure 10. Prominent burrowing enhanced by pale-dark color-banding within an interval of red sediment in Section 160-969A-9H-4, 26–81 cm.

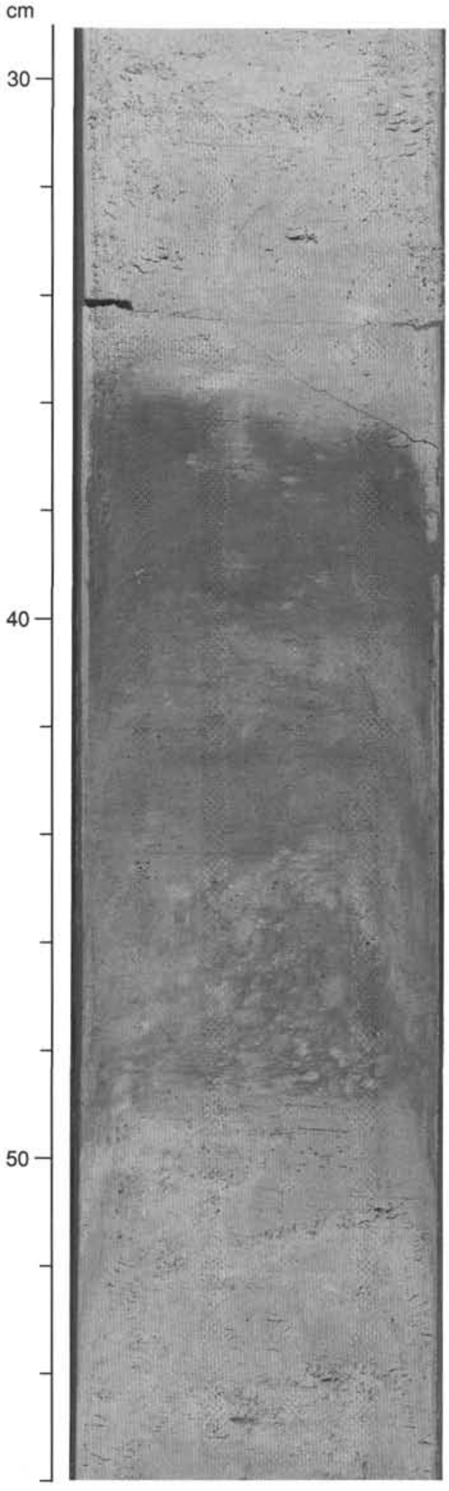

Figure 11. A decimeter-scale interbed of relatively more clay-rich, gray to grayish brown (5Y 5/1 to 10Y 5/2) nannofossil clay that is relatively enriched in hematite and opaque minerals (Section 160-969A-8H-7, 29–56 cm).

from shipboard work, is presented in Figure 23. From the six holes cored, two possible composite sections/sampling routes were constructed using the most intact sequences; one involves Holes 969A, 969B, and 969E, and the other involves Hole 969D (see Table 8, "Composite Depths" section, this chapter, and Fig. 23).

Depositional History

The earliest deposition recorded at Site 969 was the sedimentation of calcareous silty clays with laminae and thin beds of silt-sized calcite. The lack of marine microfossils and the presence of calcite with characteristic rice-grain textures suggests a nonmarine or possibly lacustrine depositional environment. The calcareous nannofossils within the uppermost levels of this sediment provide evidence of erosion of exposed Cretaceous marine sediments and either some reworking also of upper Miocene (pre-Messinian) sediments or else the onset of an, at least intermittent, marine influence.

The foraminifer nannofossil ooze present above the sharp, undeformed unconformity observed at 97.15 mbsf in Hole 969B represents an abrupt change from the lacustrine or brackish sedimentation represented below to fully marine deposition in the earliest Pliocene biozone (MPL1). The extended sapropel that occurs directly above the unconformity suggests that the Mediterranean went directly into a sapropel-generating mode that continued through the early Pliocene until high in MPL3 (at about 4.52 Ma), after which oxidized sediment is present through MPL4b. The red color and presence of hematite suggest that oxic bottom waters were present throughout this period and/or that the flux of organic matter was significantly reduced. It is not known whether a series of dark gray beds relatively enriched in hematite, opaque minerals, and some clay that occur as interbeds within the red interval are the oxidized equivalent of sapropels.

In the middle Pliocene, there was an abrupt return to the preservation of reduced sediment and sapropel deposition. The two groups of sapropels present in this interval (between nannofossil datums at 3.22 and 2.45 Ma) contain beds with the highest organic carbon values measured during Leg 160 (28.9% and 30.5% TOC). Above these two distinctive packets of sapropels, there is a return to red, oxidized sediment in an interval starting at about 2.51 Ma that spans the middle/late Pliocene boundary. Within the upper Pliocene, a further brief interval of red sediment occurs followed by preservation of reduced, gray sediment with intermittent sapropels persisting until the early Pleistocene/middle–late Pleistocene boundary, where a further thin interval of oxidized sedimentation includes the 0.99 Ma nannofossil datum. Thereafter, sapropel deposition occurred only in two beds (both Hole 969D) until after about 0.46 Ma, when sapropel deposition continued intermittently with the well-known upper Pleistocene sequence.

BIOSTRATIGRAPHY AND SEDIMENTATION RATES

Calcareous Nannofossils

Calcareous nannofossils were studied in core-catcher samples collected from Holes 969A, 969B, 969C, 969D, 969E, and 969F. To provide a higher resolution biostratigraphy, additional samples were collected from each section of core in Hole 969A. The samples ranged from late Pleistocene to early Pliocene age (Fig. 24).

Hole 969A

The base of the first biozone (MNN21) was detected in Sample 160-969A-1H-CC. This zone is defined by the presence of *Emiliania huxleyi* in quantities lower than those of the acme zone, which was not identified upsection. The accompanying assemblage includes small *Gephyrocapsa* (<3.5 µm), *Gephyrocapsa oceanica* s.l., *Helicosphaera kamptneri, Coccolithus pelagicus, Rhabdosphaera clavigera,* and *Pontosphaera japonica.*

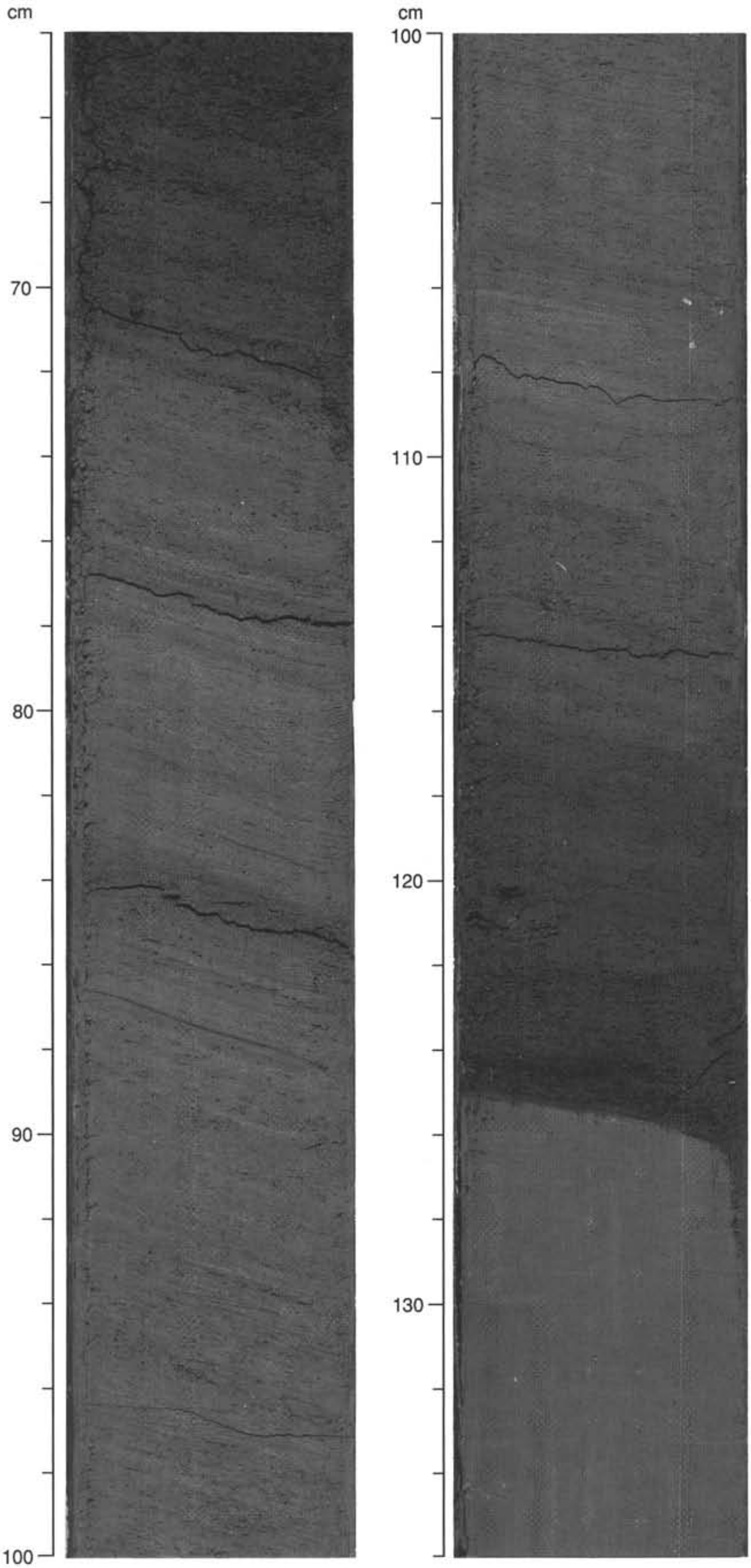

Figure 12. An intermittently laminated, composite sapropel of earliest Pliocene (Zone MPL1) age overlying massive calcareous silty clay (Section 160-969B-11H-6, 64–136 cm).

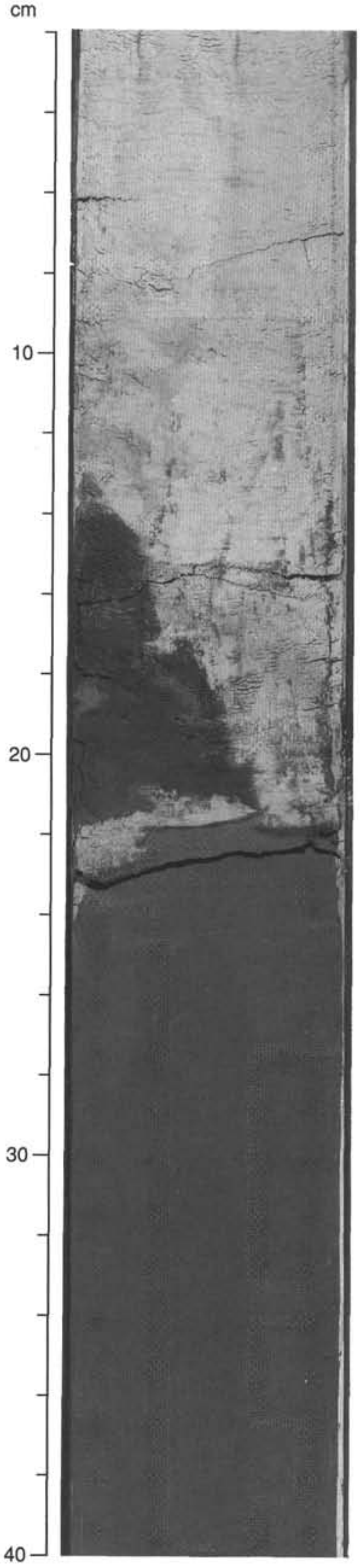

Figure 13. A deformed sapropel remnant overlying a faulted contact with calcareous silty clay at the base of Unit I (Section 160-969E-11H-6, 2–40 cm).

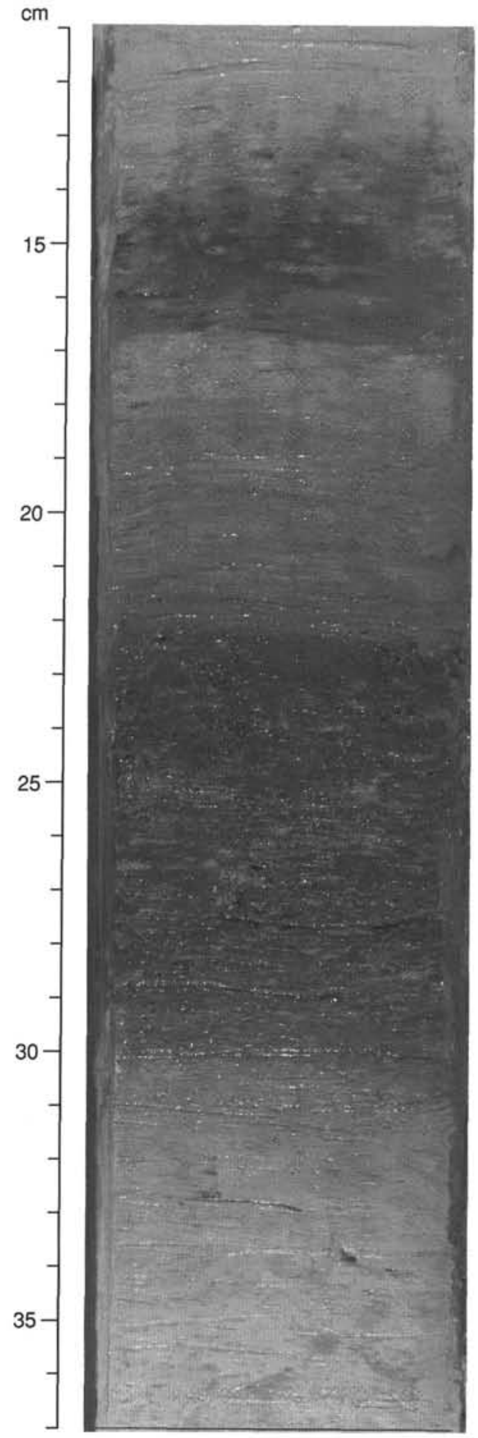

Figure 14. An 8-cm-thick development of sapropel S1 showing a distinctive supra-adjacent manganese-rich marker bed (Section 160-969E-1H-1, 11–37 cm).

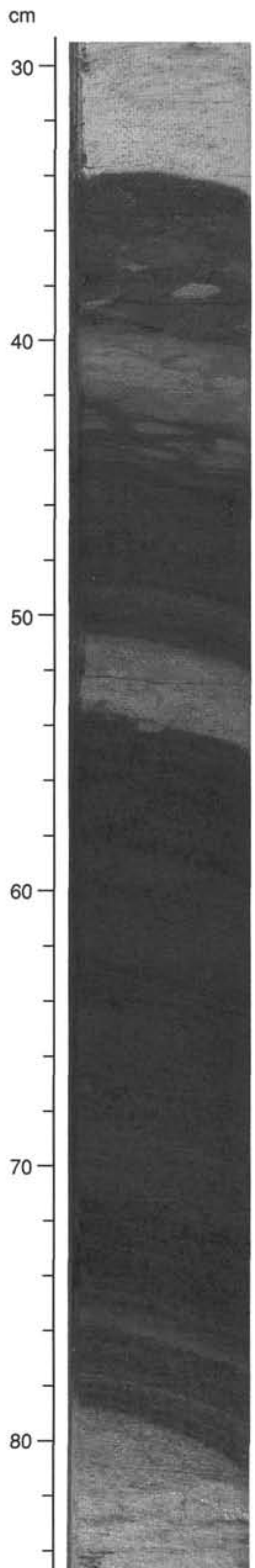

Figure 15. Sapropel S6 showing characteristic laminated lower section and moderately burrowed upper part (Section 160-969E-2H-1, 29–85 cm).

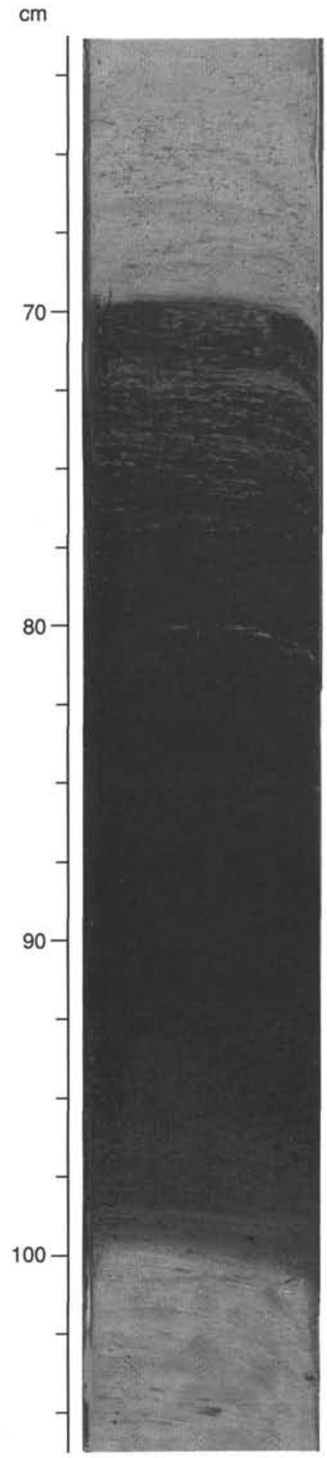

Figure 16. Intermittent laminae in the upper part of sapropel S5 (Section 160-969A-1H-3, 63–105 cm).

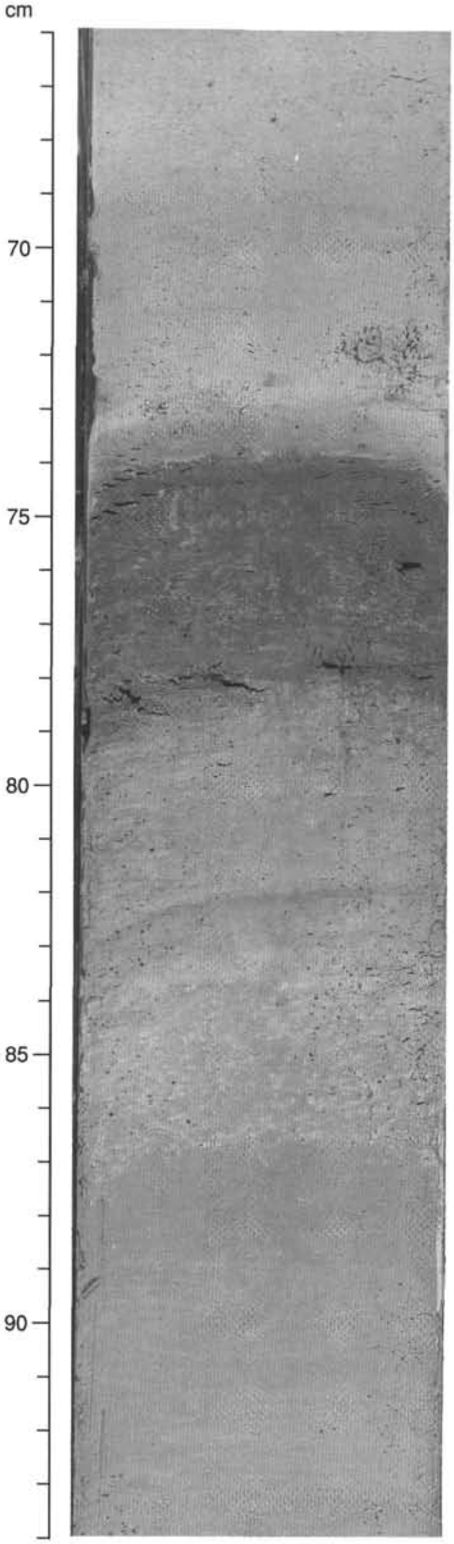

Figure 17. The lowermost sapropel within the upper Pleistocene sequence is oxidized (Section 160-969A-2H-1, 66–94 cm).

Samples 160-969A-2H-1, 70 cm, through 2H-2, 73 cm, were placed into Zone MNN20, which is a gap zone defined by the absence of both *E. huxleyi* and *Pseudoemiliania lacunosa.* The shipboard placement of the upper boundary of this zone is tentative because the first occurrence of *E. huxleyi* is difficult to recognize accurately using a light microscope. The accompanying assemblage is similar to that found uphole.

Samples 160-969A-2H-3, 65 cm, through 3H-1, 66 cm, contain nannofossils from Zone MNN19f. The upper boundary of the zone is defined by the last occurrence of *P. lacunosa,* whereas the lower boundary is defined by the first occurrence of *Gephyrocapsa* sp. 3. The last occurrence of *Gephyrocapsa* sp. 3 is in Sample 160-969A-2H-6, 63 cm. The accompanying assemblage is similar to that of the preceding zones.

Samples 160-969A-3H-2, 68 cm, through 3H-4, 70 cm, contain nannofossils from Zone MNN19e. This interval is interpreted as a gap zone identified by the absence of *Gephyrocapsa* sp. 3 and large *Gephyrocapsa* (>5.5 µm). Small *Gephyrocapsa* and *P. lacunosa* dominate the accompanying assemblage.

Samples 160-969A-3H-5, 70 cm, through 3H-CC contain nannofossils from Zone MNN19d. This zone is identified by the presence of large *Gephyrocapsa* (>5.5 µm). The accompanying assemblage is dominated by small *Gephyrocapsa, P. lacunosa,* and *G. oceanica* s.l. *Helicosphaera sellii* becomes rare in the uppermost part of the zone.

Sample 160-969A-4H-1, 76 cm, contains nannofossils from Zone MNN19c. This zone is a gap zone defined by the absence of both *Calcidiscus macintyrei* and large *Gephyrocapsa* (>5.5 µm). Small *Gephyrocapsa* and *G. oceanica* s.l. dominate the assemblage. *P. lacunosa* and *H. sellii* are common.

Samples 160-969A-4H-2, 67 cm, and 4H-2, 140 cm, contain nannofossils from Zone MNN19b. This interval is identified by the presence of both *G. oceanica* s.l. and *C. macintyrei.* The accompanying in situ and reworked assemblages are similar to those found in the previous samples.

Samples 160-969A-4H-3, 24 cm, through 4H-5, 76 cm, contain nannofossil assemblages in which both *G. oceanica* s.l. and *Discoaster brouweri* are absent and which include small *Gephyrocapsa, P. lacunosa, C. macintyrei,* and *H. sellii.* Based on the assemblage, this interval was placed into Zone MNN19a.

In Samples 160-969A-4H-6, 68 cm, through 5H-7, 34 cm, *D. brouweri* occurs in the absence of *Discoaster pentaradiatus* and *Discoaster surculus.* The accompanying assemblage is similar to that of the previous zone, but includes *Discoaster triradiatus.*

Samples 160-969A-5H-CC, through 6H-6, 138 cm, contain nannofossils from Zone MNN17–16b. This zone is recognized as the interval between the last occurrence of *D. pentaradiatus* and the last common occurrence of *Discoaster tamalis.* The accompanying assemblage includes small *Gephyrocapsa, D. brouweri, D. surculus, D. intercalaris,* and small reticulofenestrids.

Samples 160-969A-6H-7, 70 cm, through 8H-5, 120 cm, contain nannofossils belonging to Zone MNN16a. This zone is identified by the common occurrence of *D. tamalis* above the last occurrence of *Reticulofenestra pseudoumbilicus.* The accompanying assemblage is similar to that found in the preceding zone.

Samples 160-969A-8H-6, 120 cm, through 9H-2, 120 cm, contain nannofossils belonging to Zone MNN14–15. *Discoaster asymmetricus* is rare. The accompanying assemblage is similar to that found in the preceding zone.

Samples 160-969A-9H-3, 120 cm, through 9H-CC, contain nannofossils belonging to Zone MNN13. *H. sellii, R. pseudoumbilicus,* and *Sphenolithus abies* occur in the absence of *D. asymmetricus.* Additional changes from the preceding zone include the disappearance of *P. lacunosa* and small *Gephyrocapsa.* A few specimens of *Amaurolithus delicatus* are also present.

Samples 160-969A-10H-1, 120 cm, through 11H-CC, contain nannofossils belonging to Zone MNN12. This zone is identified by the presence of *Amaurolithus primus* and *Amaurolithus tricornicula-*

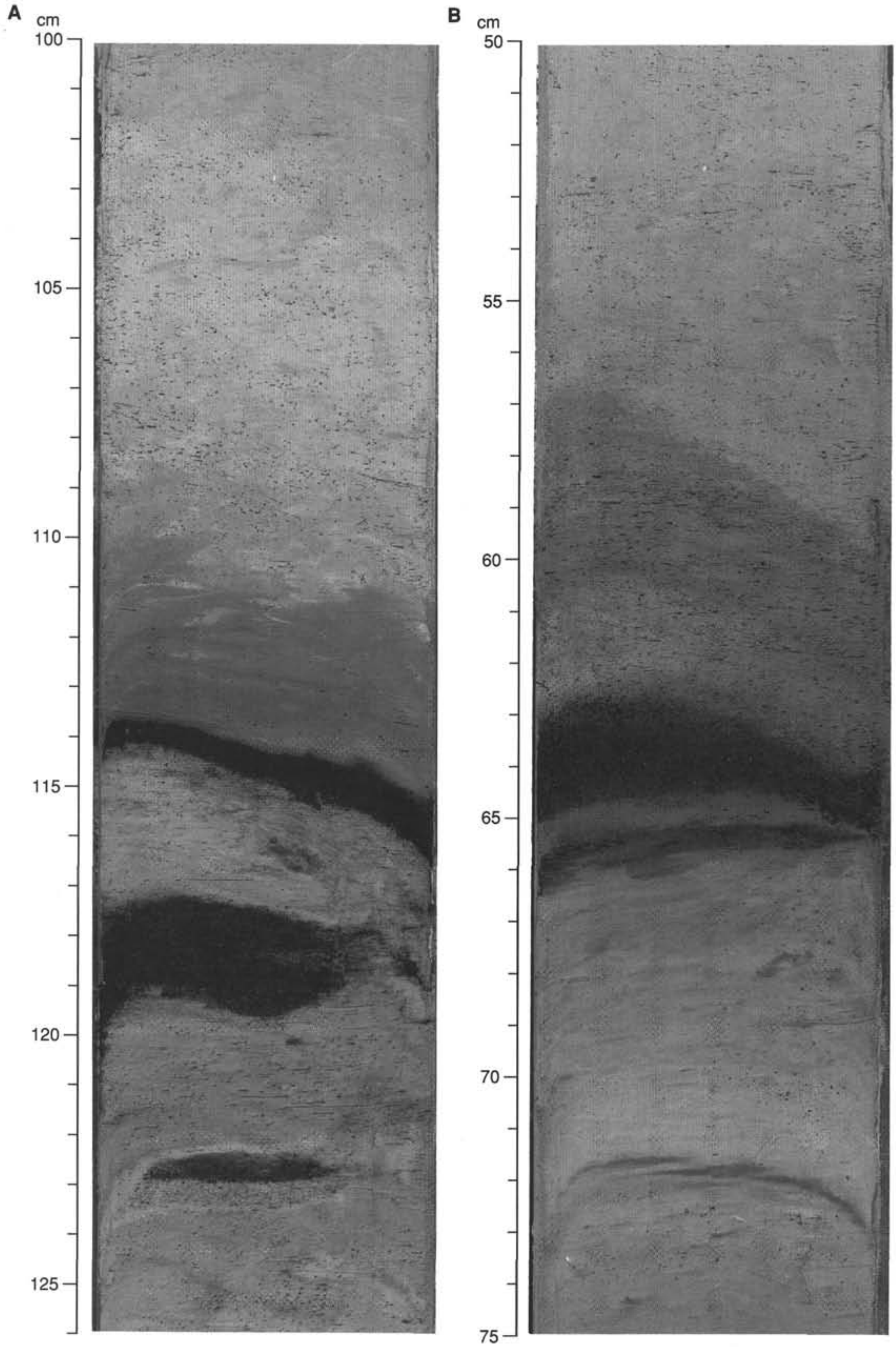

Figure 18. Examples of deformed and sheared sapropels within the upper Pliocene to lower Pleistocene sequence (**A.** Section 160-969A-3H-2, 100–126 cm; **B.** Section 160-969A-3H-4, 50–75 cm).

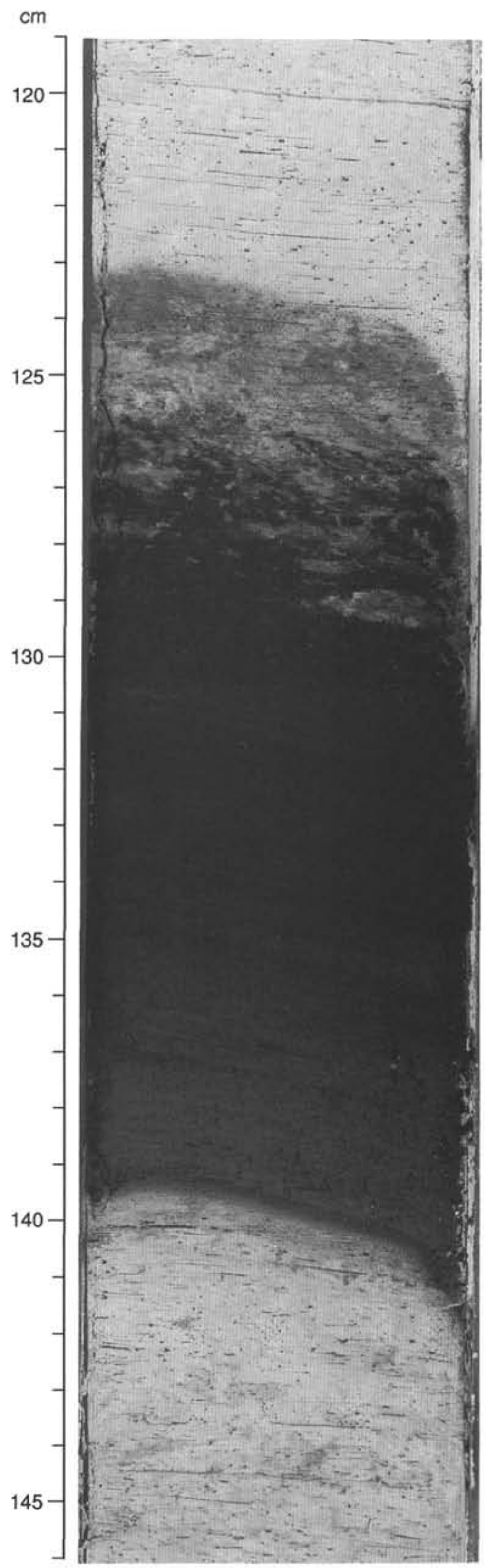

Figure 19. A laminated sapropel within the expanded uppermost Pliocene to lower Pleistocene sequence within Hole 969D. Note the typical *Chondrites*-burrowed top (Section 160-969D-5H-2, 119–146 cm).

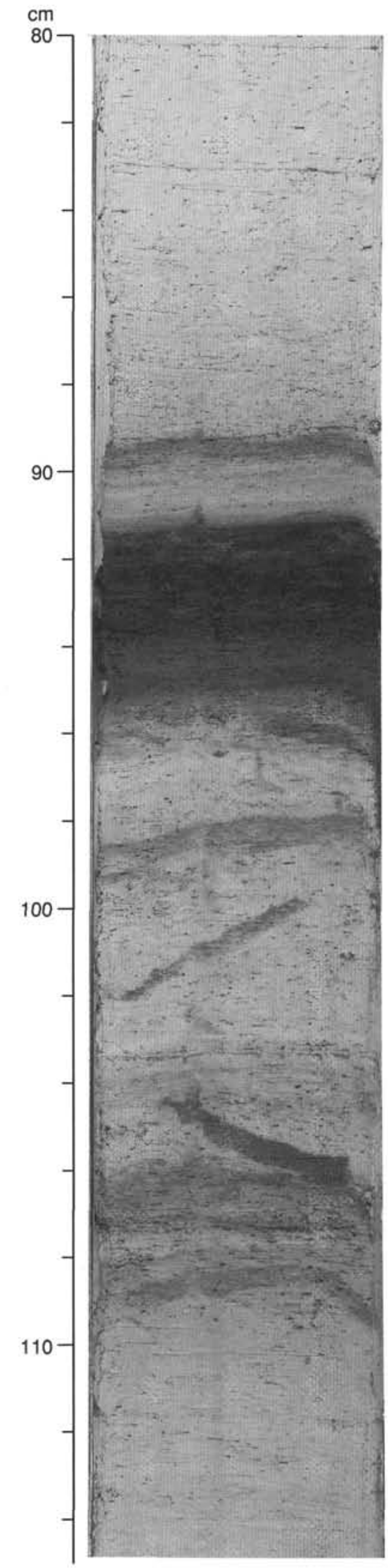

Figure 20. Some of the sapropels within the upper part of the uppermost Pliocene through lower Pliocene sequence are, unusually, burrowed by *Zoophycos* (Section 160-969D-4H-1, 80–115 cm).

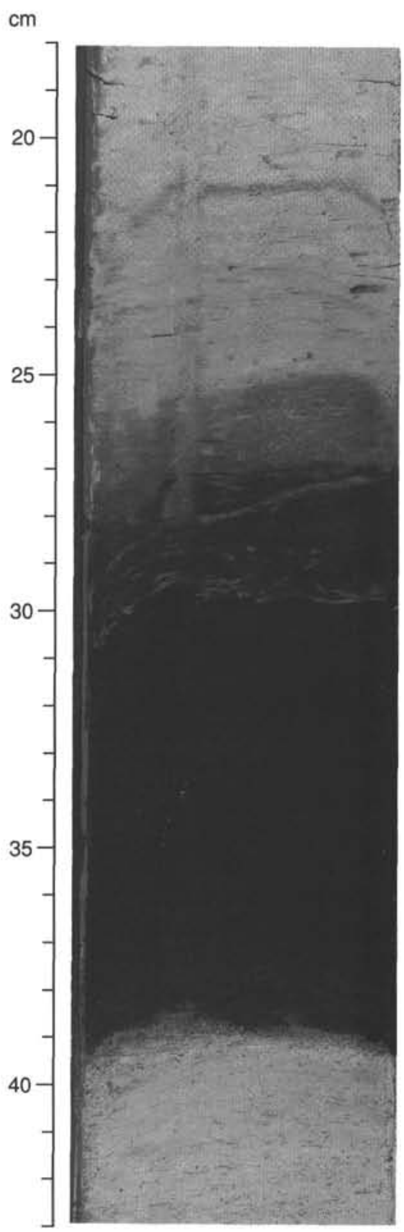

Figure 21. A black-colored sapropel from the lower of the middle Pliocene sapropel packets in Section 160-969E-6H-6, 18–43 cm. A TOC value of 28.54% was found in the equivalent bed within Hole 969A.

tus in the absence of *H. sellii. A. delicatus* is more abundant than in the zone above; otherwise, the accompanying assemblage is similar.

Samples 160-969A-12H-1, 18 cm, through 13H-CC could not be placed into a zonation owing to a paucity of nannofossils and significant reworking of older taxa. The Pliocene taxa that are present are not age diagnostic, including *S. abies, C. macintyrei,* and *C. pelagicus.* Cretaceous and Paleogene reworked taxa include *Micula decussata, Cribrosphaerella ehrenbergii, Cyclicargolithus floridanus,* and *Dictyococcites bisecta.*

Hole 969B

Eleven core-catcher samples were studied from Hole 969B. These samples generally correlate in age with samples collected from Hole 969A; however, an overlap of some zones was observed (Fig. 25). These overlaps can be attributed to missing parts of the geologic sequence owing to faulting, incorrect placement of some zonal bound-

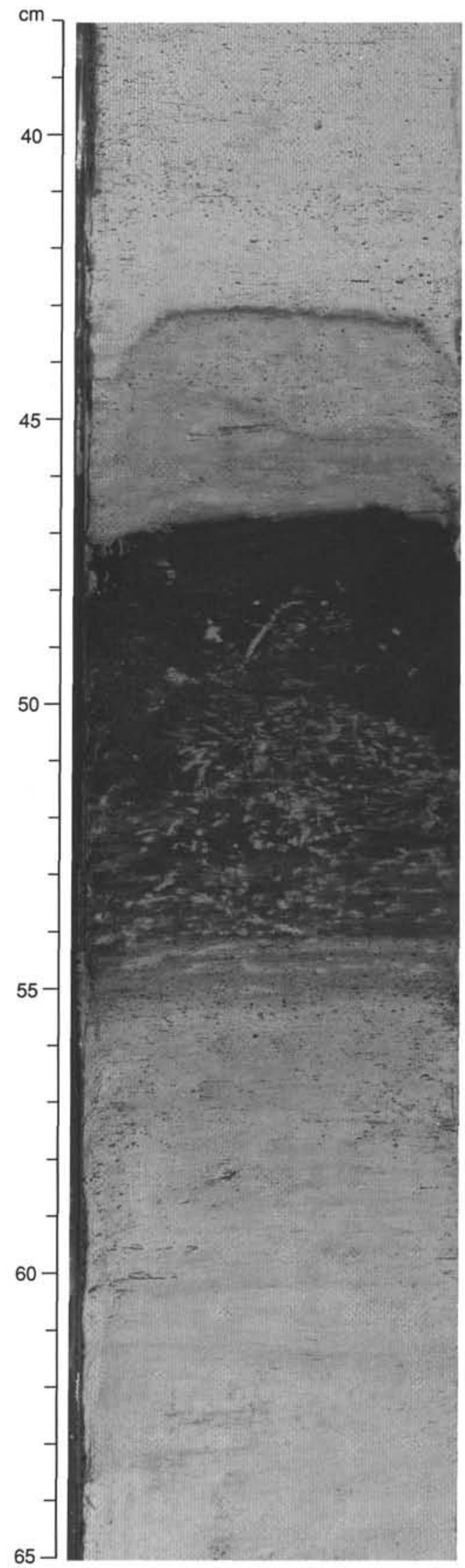

Figure 22. The lowermost bed of the upper of the two middle Pliocene sapropel packets is easily distinguished because it contains *Chondrites* burrows in the lower part of the bed only (Section 160-969E-6H-3, 38–65 cm).

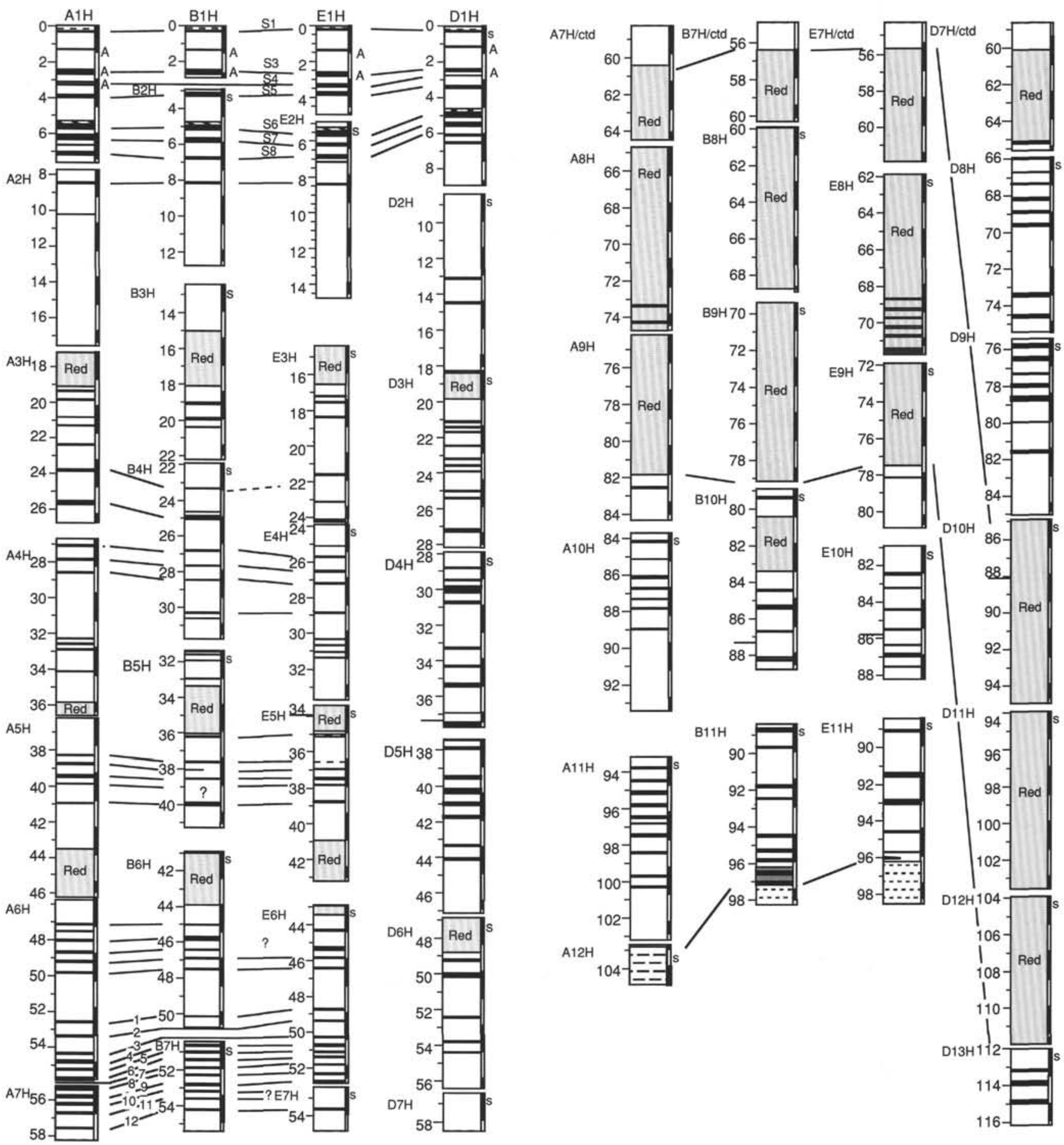

Figure 23. Summary of the occurrence of sapropels and red-colored intervals together with correlation among Holes 969A, 969B, 969E, and 969D.

aries, or the incorrect in situ depth attributed to unrecovered sediments used in correlations (see "Composite Depths" section, this chapter). In any case, shore-based studies should account for the discrepancies through additional biostratigraphic work and composite section correlations.

Hole 969C

The one core-catcher sample studied from Hole 969C is of middle to late Pleistocene age. This sample contains *P. lacunosa* but not *E. huxleyi,* which places this sample in Zone MNN19f.

Hole 969D

The 13 core-catcher samples studied from Hole 969D contain late Pleistocene to early Pliocene age nannofossils similar to the other holes at Site 969. However, the geologic section recovered from Hole 969D was expanded relative to the other holes. The discrepancy of the depths at which the nannofossil zones were detected is particularly apparent from Core 160-969A-5H-CC to the total depth of the hole, as shown on Figure 25. Other than the apparent expanded geologic section from Hole 969D, the assemblages observed are principally the same as those described for Hole 969A.

Table 2. Position and extent of sapropels recovered from Hole 969D.

Core, section, interval (cm)	Depth (mbsf)	Thickness (cm)
160-969D-		
1H-1, 27	0.27	6
1H-2, 87	2.37	9
1H-3, 25	3.25	22
1H-4, 25	4.75	10
1H-4, 42	4.92	21
1H-4, 102	5.52	12
1H-5, 3	6.03	20
1H-5, 55	6.55	3
2H-4, 13	13.53	7
2H-4, 123	14.63	1
2H-5, 10	15.00	5
3H-2, 114	21.04	1
3H-2, 119	21.09	4
3H-3, 5	21.45	4
3H-3, 42	21.82	3
3H-3, 96	22.36	8
3H-4, 31	23.21	7
3H-4, 74	23.64	3
3H-4, 108	23.98	9
3H-5, 61	25.01	4
3H-5, 101	25.41	6
3H-6, 129	27.19	13
4H-1, 91	28.81	3
4H-2, 5	29.45	15
4H-2, 51	29.91	35
4H-2, 122	30.62	17
4H-4, 82	33.22	9
4H-5, 35	34.25	16
4H-5, 140	35.30	17
4H-CC, 0	37.46	8
4H-CC, 12	37.58	4
5H-1, 0	37.40	6
5H-1, 45	37.85	9
5H-1, 60	38.00	5
5H-2, 42	39.32	29
5H-2, 123	40.13	16
5H-2, 149	40.39	8
5H-3, 38	40.78	31
5H-3, 120	41.60	16
5H-4, 75	42.65	2
5H-4, 139	43.29	11
5H-5, 58	43.98	8
5H-6, 16	45.06	0.5
6H-2, 6	48.46	22
6H-2, 81	49.21	12
6H-3, 102	50.92	6
6H-4, 103	52.43	9
6H-5, 18	53.08	2
6H-5, 80	53.70	20
6H-5, 108	53.98	2
6H-6, 2	54.42	4
7H-1, 97	57.00	1
7H-6, 136	65.00	4
8H-1, 6	65.96	2
8H-1, 77	66.67	4
8H-1, 140	67.30	15
8H-2, 68	68.08	13
8H-2, 143	68.83	3
8H-3, 63	69.53	13
8H-5, 142	73.32	18
8H-6, 108	74.48	17
9H-1, 27	75.67	16
9H-1, 96	76.36	21
9H-2, 38	77.28	5
9H-2, 96	77.86	18
9H-3, 14	78.54	25
9H-4, 5	79.95	1
9H-5, 9	81.49	15
11H-4, 2	98.92	16
11H-6, 2	101.92	4
11H-6, 35	102.25	15
11H-6, 75	102.65	13
11H-6, 125	103.15	5
12H-1, 27	104.17	12
12H-1, 70	104.60	12
12H-1, 110	105.00	4
13H-1, 25	112.25	23
13H-1, 130	113.30	25
13H-2, 113	114.60	39
13H-3, 42	115.42	2

Hole 969E

The 11 core-catcher samples studied from Hole 969E contain late Pleistocene to early Pliocene age nannofossils similar to the other holes at Site 969 as shown on Figure 25.

Hole 969F

The one core-catcher sample studied from Hole 969F is of middle to late Pleistocene age. This sample contains *P. lacunosa* but not *E. huxleyi,* which places this sample in Zone MNN19f.

Planktonic Foraminifers

Samples from all core catchers from Hole 969A were analyzed in addition to 31 samples from within the cores.

Pleistocene and Pliocene foraminifers range in abundance from absent to dominant and consist of diversified and generally well-preserved faunas similar to those observed in the other sites. The lower part of the section was devoid of planktonic foraminifers and abundant ostracodes were found. Abundant reworking occurs only in Core 160-969A-2H.

The interval spanning the *Truncorotalia truncatulinoides excelsa–Globigerina cariacoensis* Zones was identified for the Pleistocene and eight zonal boundaries, encompassing Zones MPL6 through MPL1, were identified for the Pliocene (Fig. 24), according to the zonation scheme of Cita (1975), emended by Sprovieri (1993).

As previously observed, the *Truncorotalia truncatulinoides excelsa* and *Globigerina cariacoensis* Zones were not recognized owing to the scarcity of *T. truncatulinoides excelsa.* The two zones span the entire Pleistocene, from Samples 160-969A-1H-1, 63–65 cm, through 4H-5, 3–5 cm.

Only Sample 160-969A-4H-6, 5–7 cm, was attributed to Zone MPL6. In this sample, the lowest occurrence of *Globorotalia inflata* was observed, together with the highest occurrence of the Pliocene species *Sphaeroidinella dehiscens.*

Zone MPL5b was identified from Samples 160-969A-4H-CC through 7H-1, 121–123 cm. Its lower boundary is equated the highest occurrence of *Globorotalia bononiensis* in Sample 160-969A-7H-2, 116–118 cm.

The highest occurrence of *Sphaeroidinellopsis* spp. in Sample 160-969A-7H-3, 120–122 cm, marks the top of MPL4b. This zone is identified through Sample 160-969A-7H-3, 120–122 cm.

The upper boundary of Zone MPL4a, placed with the highest occurrence of *Globorotalia puncticulata,* occurs in Sample 160-969A-7H-CC. This zone was identified through Sample 160-969A-8H-5, 43–45 cm.

Zone MPL3 was identified from Samples 160-969A-8H-CC through 9H-CC. Its boundaries are placed with the last occurrence of *Globorotalia margaritae* and the first occurrence of *G. puncticulata* at the top and at the bottom, respectively.

The first occurrence of *G. margaritae* in Sample 160-969A-10H-CC permits identification of the lower boundary of Zone MPL2 and the upper boundary of Zone MPL1 in Sample 160-969A-11H-2, 14–16 cm. The MPL1 acme level of *Sphaeroidinellopsis* spp. was also observed in Sample 160-969A-11H-CC.

The sediments below are devoid of planktonic foraminifers or contain very scarce and poorly preserved forms that are not age diagnostic.

Benthic Foraminifers

A (preliminary) qualitative study of benthic foraminifers was performed on Hole 969A in order to track the possible bathymetric changes through the Pliocene-Pleistocene sequence. The bathymetric zonal scheme is according to Hasegawa et al. (1990).

Benthic assemblages are well-preserved but extremely scarce and poorly diversified through the entire sequence recovered in Hole

Table 3. Position and organic carbon content of sapropels recovered from Hole 969A and correlatable beds in Holes 969B and 969E.

Core, section, interval (cm)	Depth (mbsf)	Thickness (cm)	C_{org} (%)	Number	Core, section, interval (cm)	Depth (mbsf)	Thickness (cm)	C_{org} (%)	Number	Core, section, interval (cm)	Depth (mbsf)	Thickness (cm)	C_{org} (%)	Number
160-969A-					160-969B-					160-969E-				
1H-1, 26	0.26	7	2.86	S1	1H-1, 27	0.27	7		S1	1H-1, 26	0.26	11		S1
1H-2, 88	2.38	28	3.64	S3	1H-2, 107	2.57	9		S3	1H-2, 117	2.67	7		S3
1H-3, 24	3.24	2	3.09	S4						1H-3, 25	3.25	3		S4
1H-3, 70	3.70	28		S5	2H-1, 22	3.12	33		S5	1H-3, 68	3.68	32		S5
1H-4, 80	5.30	41	3.93	S6	2H-2, 36	4.76	46		S6	2H-1, 34	5.24	45		S6
1H-5, 5	6.05	23	7.82	S7	2H-2, 124	5.64	23		S7	2H-1, 123	6.13	16		S7
1H-5, 108	7.08	9	3.4	S8	2H-3, 82	6.72	6		S8	2H-2, 37	6.77	14		S8
2H-1, 73	8.43	4			2H-4, 70	8.10	8			2H-3, 32	8.22	14		
3H-2, 59	19.29	12												
3H-2, 111	19.81	6	9.17											
3H-3, 63	20.83	1	16.96											
3H-3, 107	21.27	4.5	6.58											
3H-4, 62	22.32	2												
3H-5, 55	23.75	12	17.6		4H-1, 138	23.28	6							
3H-6, 17	24.87	9												
3H-6, 85	25.55	4	2.86											
3H-6, 94	25.64	11	2.46		4H-2, 149	24.89	17							
4H-1, 32	27.02	7	12.63		4H-4, 36	26.76	7			4H-2, 29	25.69	4		
4H-1, 110	27.80	10	8.76		4H-4, 122	27.62	5			4H-2, 108	26.48	10		
4H-2, 34	28.54	6			4H-5, 51	28.41	5			4H-3, 28	27.18	6		
4H-4, 95	32.15	2												
4H-4, 125	32.45	5	16.91											
4H-5, 8	32.78	1												
4H-5, 10	32.80	5	11.83											
4H-5, 133	34.03	4	6.32											
					5H-4, 27	36.17	1			5H-2, 110	36	10		
5H-2, 57	38.27	3	3.53		5H-5, 18	37.58	6							
5H-2, 100	38.70	9			5H-5, 60	38	1			5H-3, 51	36.91	2		
5H-3, 13	39.33	5	6.94		5H-5, 110	38.50	4			5H-3, 96	37.36	15		
5H-3, 25	39.45	3												
5H-3, 62	39.82	4	2.75							5H-3, 141	37.81	2		
5H-4, 21	40.91	5	8.33		5H-6, 108	39.98	5			5H-4, 79	38.69	6		
6H-1, 128	46.98	11	15.81		6H-3, 108	44.98	6							
6H-2, 28	47.48	2	5.36											
6H-2, 76	47.96	10	6.24		6H-4, 28	45.68	23							
6H-2, 136	48.56	14	6.42		6H-4, 98	46.38	7							
6H-3, 42	49.12	7	4.35		6H-4, 147	46.87	8			6H-2, 143	45.83	7		
6H-3, 95	49.65	11	5.38		6H-5, 56	47.46	7			6H-3, 47	46.37	7		
6H-5, 77	52.21	8	21.15	1	6H-7, 17	50.07	7		1	6H-4, 129	48.69	6		1
6H-6, 0	52.94	14	12.39	2						6H-5, 47	49.37	7		2
6H-6, 99	53.93	7	12.57	3						6H-5, 135	50.25	7		3
6H-6, 139	54.33	16	28.54	4	7H-1, 15	50.55	11		4	6H-6, 27	50.67	12		4
6H-7, 35	54.79	12	20.88	5	7H-1, 53	50.93	11		5	6H-6, 68	51.08	5		5
6H-CC, 2	55.29	8	19.14	6	7H-1, 96	51.36	11		6	6H-6, 105	51.45	7		6
					7H-1, 144	51.84	2		7	6H-6, 146	51.86	1		7
7H-1, 7	55.27	15	20.59	8	7H-2, 33	52.23	14		8	6H-7, 37	52.27	11		8
7H-1, 50	55.70	17	30.54	9	7H-2, 77	52.67	16		9	6H-CC, 13	52.74	7		9
7H-1, 94	56.14	11	18.46	10	7H-2, 119	53.09	8		10					
					7H-3, 16	53.56	6		11					
7H-2, 80	57.50	8	18.22	12	7H-3, 75	54.15	7		12	7H-1, 115	53.55	8		12
8H-6, 103	73.23	16												
8H-7, 36	74	13	0.03											
8H-CC, 12	74	5												
9H-1, 9	74.29	2												
9H-1, 38	74.58	3												
9H-1, 146	75.66	15												
9H-2, 68	76.38	8												
9H-6, 71	82.41	4	4.62											
10H-1, 145.5	85.155	0.5												
10H-1, 84	86.04	14	5.07											
10H-2, 148	86.68	10												
10H-3, 56	87.26	5												
10H-3, 115	87.85	6												
10H-4, 70	88.9	4	2.26											
11H-1, 53	93.73	7	4											
11H-1, 121	94.41	12	3.25											
11H-2, 35	95.05	14	3.42											
11H-2, 106	95.76	11	2.25											
11H-3, 20	96.4	12												
11H-3, 58	96.78	5												
11H-3, 118	97.38	15	5.08											
11H-4, 58	98.28	10												
11H-5, 44	99.64	16												
11H-5, 94	100.14	20												

969A. Most of the Pleistocene sediments (Samples 160-969A-1H-1, 63–65 cm, through 4H-1, 131–133 cm) contain relatively abundant *Ariculina tubulosa* along with rare specimens of *Pyrgo murrhina* and *Cassidulina carinata.* This assemblage may be related to the middle to lower mesobathyal assemblage E of Hasegawa et al. (1990).

In lower Pleistocene and upper Pliocene sediments (Samples 160-969A-4H-3, 9–11 cm, through 5H-CC) benthic foraminifers decrease in abundance and consist of *Gyroidinoides altiformis, Gyroidina soldanii,* and *Oridorsalis umbonatus.* This assemblage may be related to the middle mesobathyal assemblage D of Hasegawa et al. (1990).

In Cores 160-969A-7H through 9H, the benthic foraminifer *Siphonina reticulata* exhibits the highest relative abundances. It occurs together with the rarer taxa *Siphonina planoconvexa, Globocassidulina oblonga,* and *O. umbonatus.* This assemblage may be related

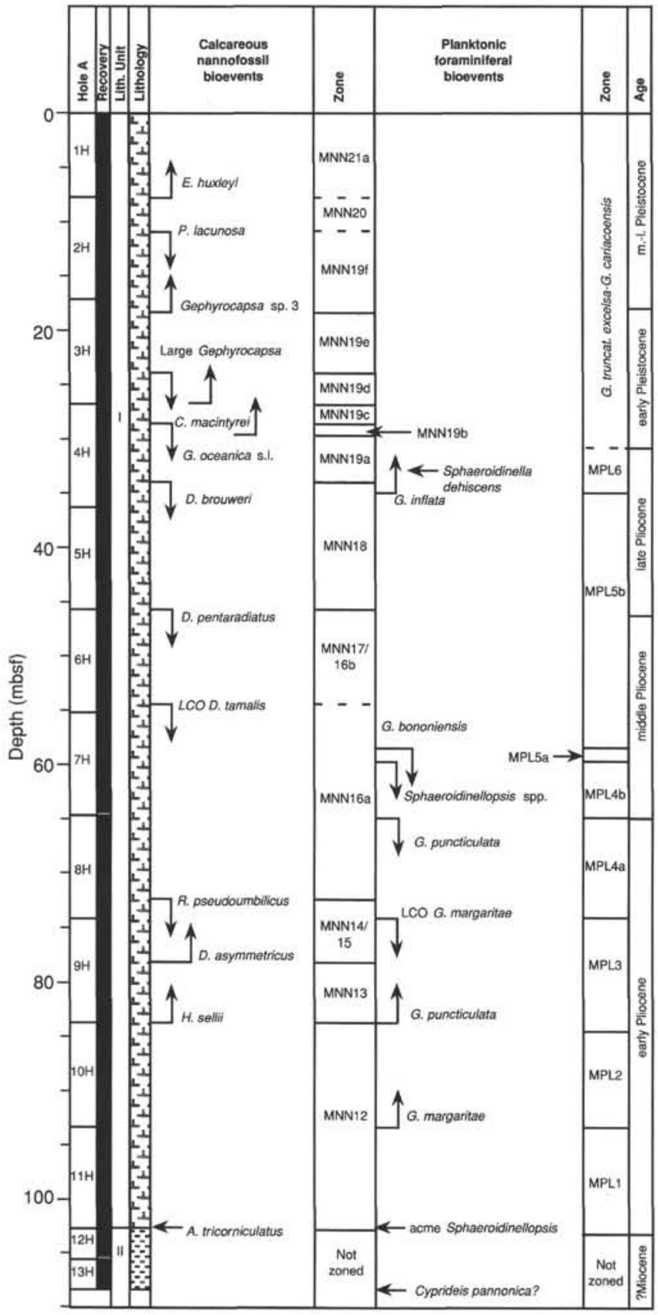

Figure 24. Composite of biostratigraphic events recognized in sediments recovered from Hole 969A including the lithostratigraphic record.

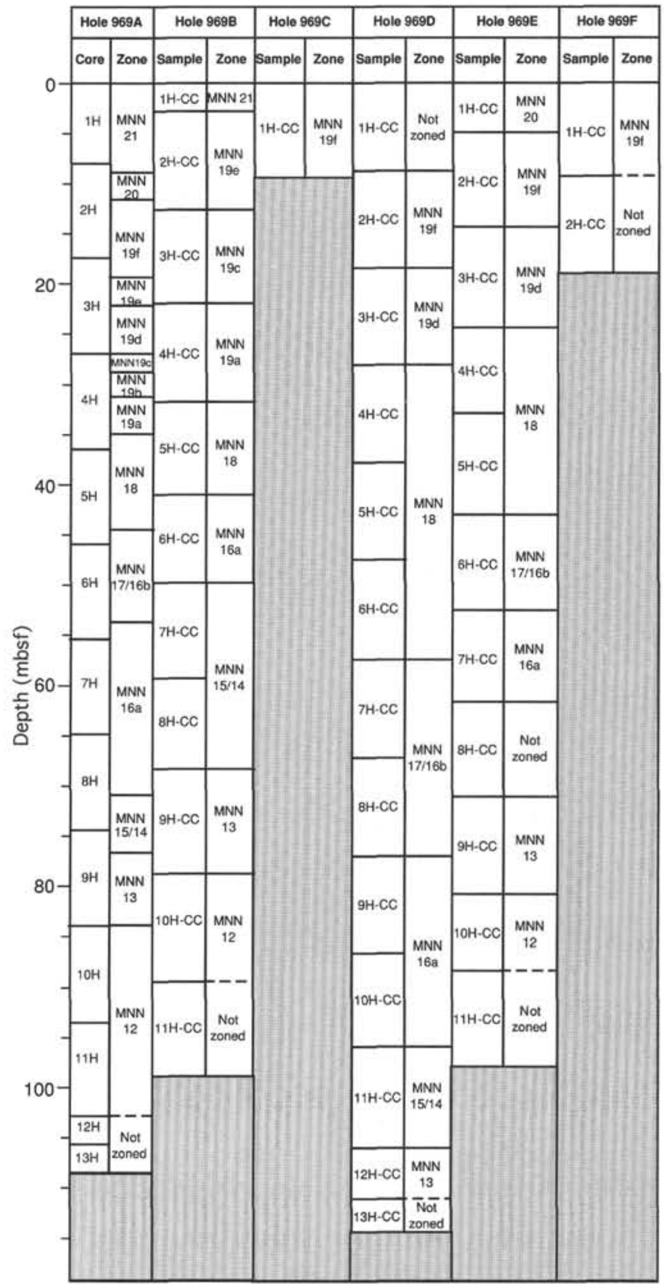

Figure 25. Composite of calcareous nannofossil zones recognized from samples collected from within each section of core in Hole 969A and core-catcher samples recovered from Holes 969C, 969D, 969E, and 969F.

to the epibathyal assemblage B of Hasegawa et al. (1990). The presence of abundant *S. reticulata* suggests salinities higher than normal marine waters (Hasegawa et al., 1990).

Other Taxa

Only a very few specimens of Bolboforma were found in samples from Hole 969A. They occur in Samples 160-969A-9H-5, 38–40 cm, and 10H-3, 100–102 cm (lower Pliocene); they may possibly be attributed to *Bolboforma* sp. E (Spiegler and Rögl, 1992). A few specimens of the microfossil morphologically similar to Bolboforma, as described for Holes 964A and 965A, were also found in Hole 969A.

Ostracodes tentatively identified as *Cyprideis pannonica* were also found in Sample 160-969A-13H-CC. These forms are typical of brackish environments and are common in evaporite-related facies in the Messinian. However, they are not considered age diagnostic, because they may also occur within the lowermost few centimeters of the invading Pliocene psycrospheric fauna (Benson, 1978).

Sedimentation Rates

Sedimentation rates for Hole 969A were calculated using 18 calcareous nannofossil and planktonic foraminiferal events (Table 4). The data are plotted on the age vs. depth curve shown in Figure 26. An error line is shown on the figure to indicate the degree of uncertainty as to the location of the nannofossil and foraminiferal events within the hole.

Calculated sedimentation rates vary from 6 to 33 m/m.y. through the sequence. Nine significant shifts in sedimentation rates were observed. From the seafloor to the last occurrence of *C. macintyrei*

Table 4. Stratigraphic list of calcareous nannofossil and planktonic foraminifer events for Site 969.

Event	Core, section, interval (cm)	Depth (mbsf)	Depth (mcd)	Age (Ma)
	160-969A-			
FO *E. huxleyi**	1H-CC	7.52	7.61	0.26
LO *P. lacunosa*	2H-3, 65	11.35	11.67	0.46
FO *Gephyrocapsa* sp. 3	3H-1, 66	17.86	19.03	0.99
LO *Gephyrocapsa* >5.5 µm	3H-5, 70	23.9	25.07	1.25
FO *Gephyrocapsa* >5.5 µm	3H-CC	27.05	28.22	1.5
LO *C. macintyrei*	4H-2, 67	28.87	31.35	1.62
FO *G. oceanica* s.l.	4H-2, 140	29.6	32.08	1.75
LO *D. brouweri*	4H-6, 68	34.88	37.36	1.99
FO *G. inflata*	4H-6, 5–7	34.25	36.73	2.13
LO *D. pentaradiatus*	5H-CC	46.18	48.98	2.51
LCO *D. tamalis*	6H-7, 70	55.14	58.19	2.82
LO *Sphaeroidinellopsis* spp.	7H-3, 120–122	59.4	62.78	3.22
LO *G. puncticulata*	7H-CC	64.49	67.87	3.57
LO *R. pseudoumbilicus*	8H-6, 120	73.4	77.13	3.85
LCO *G. margaritae*	8H-CC	74.71	78.44	3.94
FCO *D. asymmetricus*	9H-2, 120	76.9	82.26	4.11
FO *G. puncticulata*	9H-CC	84.3	89.66	4.52
FCO *G. margaritae*	10H-CC	93.36	100.8	5.10

Notes: FO = first occurrence; LO = last occurrence; FCO = first common occurrence; LCO = last common occurrence; * = to be confirmed by scanning electron microscopy.

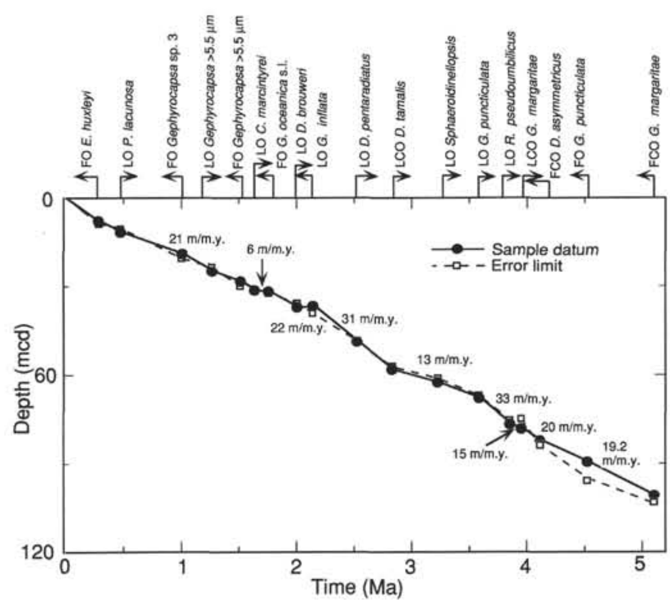

Figure 26. Age vs. depth diagram showing selected calcareous nannofossil and planktonic foraminifer datums with corresponding sedimentation rates. The solid line corresponds to the sample where the marker species was found for the corresponding first or last occurrence datum, and the dashed line corresponds to the nearest sample where the marker species was not found.

(1.62 Ma) the sedimentation rate was approximately 21 m/m.y. The sedimentation rate decreased to 6 m/m.y. in the interval from the last occurrence of *C. macintyrei* to the first occurrence of *G. oceanica* s.l. (1.75 Ma). Sedimentation increased to 22 m/m.y. in the interval from the latter event down to the last occurrence of *D. brouweri* (1.99 Ma). In the interval from the last occurrence of *D. brouweri* to the first occurrence of *G. inflata* (2.13 Ma) the sedimentation rate could not be determined, as the older first occurrence of *G. inflata* was observed higher in the section than the last occurrence of *D. brouweri*. The average sedimentation rate increased to 31 m/m.y. between the first occurrence of *G. inflata* and the last common occurrence of *D. tamalis* (2.82 Ma). Between the last common occurrence of *D. tamalis* and the last occurrence of *G. puncticulata* (3.57 Ma) the sedimentation rate decreased to 13 m/m.y. The sedimentation rate then increased to 33 m/m.y. in the interval from the last occurrence of *G. puncticulata* to the last occurrence of *R. pseudoumbilicus* (3.85 Ma). The sedimentation rate decreased to 15 m/m.y. between the last occurrence of *R. pseudoumbilicus* and the last common occurrence of *G. margaritae* (3.94 Ma). From the last common occurrence of *G. margaritae* to the first occurrence of *G. puncticulata* (4.52 Ma) the sedimentation rate averaged 21 m/m.y. From the latter bioevent to the first common occurrence of *G. margaritae* (5.10 Ma) the average sedimentation rate decreased to 19.2 m/m.y.

PALEOMAGNETISM

Paleomagnetic measurements were made on cores from Holes 969A, 969B, 969D, and 969E, following the methods discussed in the "Explanatory Notes" chapter (this volume). The NRM was routinely measured at 10-cm intervals on the archive half of each core section for each hole after AF demagnetization at 25 mT. NRM intensities were measurable throughout the recovered sequence and were above the noise level of the magnetometer (Fig. 27). Many of the intensity peaks coincide with sapropels (Fig. 27), as discussed by Roberts et al. (this volume).

Because of time constraints, only 16 discrete samples from Hole 969A were subjected to stepwise AF demagnetization. It was, therefore, not possible to verify the reliability of the whole-core measurements in detail. Most of the demagnetized samples display similar stability to that observed at previous sites (Fig. 28A) (e.g., Sites 964, 966, and 967); therefore, it is anticipated that shore-based studies will enable derivation of a reliable magnetic polarity stratigraphy. Samples from stratigraphic intervals that are dominantly red in color (see "Lithostratigraphy" section, this chapter) display coercivity spectra that are much more resistant to AF demagnetization than samples from other intervals, as is evident in the amount of remanence remaining even after demagnetization at 95 mT (Fig. 28B). This observation is consistent with the likelihood of the presence of hematite in the red intervals. The whole-core AF demagnetization results discussed below should therefore be treated with caution because of the possibility that AF demagnetization has not been able to isolate a stable characteristic remanence component.

The paleomagnetic inclination record generated from the archive-half sections at Site 969 is characterized by numerous zones of normal and reversed polarity (Fig. 29). In conjunction with the biostratigraphic data (see "Biostratigraphy and Sedimentation Rates" section, this chapter), it is possible to delineate a partial, but preliminary, magnetostratigraphy. Interpreted positions for the Matuyama/Brunhes boundary, Jaramillo Subchron, Gauss/Matuyama boundary, Gilbert/Gauss boundary, and upper limits of the Cochiti and Thvera Subchrons are shown on Figure 30, relative to the biostratigraphic datums. The position of the Gauss/Matuyama boundary is obscure in the magnetic record and is constrained primarily by biostratigraphic data. It occurs between the last common occurrence of *Discoaster tamalis* and the last occurrence of *Discoaster pentaradiatus*, which are dated in the Mediterranean at 2.82 and 2.51 Ma, respectively (Sprovieri, 1993). This polarity transition is poorly constrained in Hole 969A, and it is only slightly better resolved in the other holes at Site 969. A zone of normal polarity is evident in the whole-core record in Hole 969A, directly above the Gauss/Matuyama boundary. This zone is significantly older than would be expected for the Olduvai Subchron, as suggested by the first occurrence of *Globorotalia inflata* and the last occurrence of *Discoaster brouweri* at 2.13 and 1.99 Ma, respectively (Sprovieri, 1993). This zone of normal polarity may therefore be an artifact of incomplete cleaning of a normal polarity overprint. This part of the sequence consists largely of red sediment, which may be responsible for a normal polarity overprint that is resistant to AF demagnetization. A transition from reverse to normal polarity at approximately 70 mbsf may represent the Gilbert/Gauss

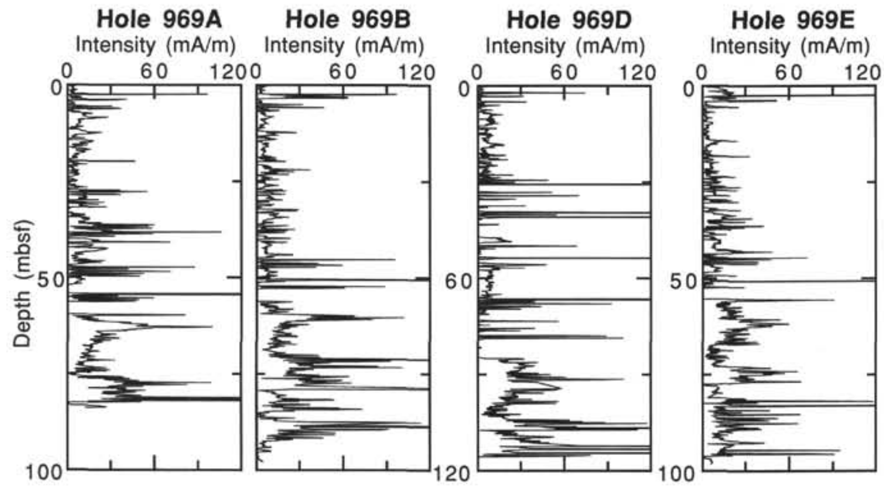

Figure 27. NRM intensity after AF demagnetization at 25 mT for Holes 969A, 969B, 969D, and 969E.

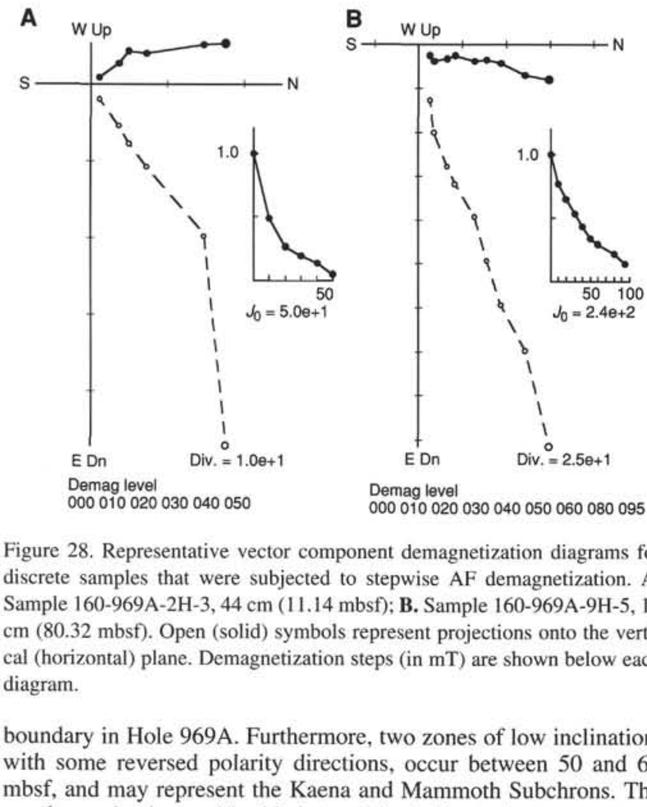

Figure 28. Representative vector component demagnetization diagrams for discrete samples that were subjected to stepwise AF demagnetization. **A.** Sample 160-969A-2H-3, 44 cm (11.14 mbsf); **B.** Sample 160-969A-9H-5, 12 cm (80.32 mbsf). Open (solid) symbols represent projections onto the vertical (horizontal) plane. Demagnetization steps (in mT) are shown below each diagram.

boundary in Hole 969A. Furthermore, two zones of low inclination, with some reversed polarity directions, occur between 50 and 60 mbsf, and may represent the Kaena and Mammoth Subchrons. The poorly resolved record in this interval is similar to that encountered at Site 966 (see "Paleomagnetism" section, "Site 966" chapter, this volume) and may result from the diagenetically reduced nature of the gray sediments in this interval (see "Lithostratigraphy" section, this chapter). The inferred positions of the Gilbert/Gauss boundary and the upper boundaries of the Cochiti and Thvera Subchrons are consistent with the biostratigraphic data (see "Biostratigraphy and Sedimentation Rates" section, this chapter), as shown on Figures 30 and 31. As is also the case at most other sites studied during Leg 160, the whole-core paleomagnetic data do not provide a clear magnetic polarity stratigraphy in the upper part of the record, including the interval around the Matuyama/Brunhes polarity transition. However, there is good agreement between the first occurrence of *Gephyrocapsa* sp. 3 (17.86 mbsf), which is dated at 0.99 Ma (Sprovieri, 1993), and an interval of normal polarity that possibly represents the Jaramillo Subchron.

First-order similarity among the whole-core data from Holes 969A, 969B, and 969E (Fig. 29), and good agreement between the preliminary magnetostratigraphic interpretation and the biozonations (Fig. 31), suggests that it should be possible to obtain a useful composite magnetostratigraphy from Site 969 after detailed post-cruise investigation.

STRUCTURAL GEOLOGY

Five of the six holes at Site 969 were located on a small (1 km across) northwest-southeast-striking ridge on part of the Mediterranean Ridge south of Crete. Hole 969D was located slightly to the southwest (Fig. 5, see "Site Geophysics" section, this chapter). The structural observations at this site indicate that although normal faulting is common on the most topographically elevated area, reverse faulting dominates the deformation in Hole 969D, which is in slightly deeper water.

In Holes 969A, 969B, 969E, and 969F, the majority of the faults are high-angle normal faults with millimeter to centimeter offsets. For some of the microfaults it was not possible to match offset layers on either side. In these cases, the displacement was inferred to have been greater than the length of the fault exposed in the core face (i.e., up to 20 cm). Concentrations of normal faults occur in Cores 160-969A-10H and 11H and 160-969B-5H and 6H (Table 5); minor faulting occurs in several places and typically is related to the occurrence of sapropels. Horizontal bedding planes predominate the succession in Holes 969A, 969B, and 969C, but tilted bedding surfaces are relatively common.

In Hole 969D, however, tilted bedding surfaces were observed in most of the cores, but particularly from Core 160-969D-5H downward. Sets of fanlike reverse faults and single reverse faults were found in this hole, clustering in Cores 160-969D-10H, 12H, and 13H (cf., Table 5). As a consequence of either tilting of beds or the "imbricate" thrust patterns observed in Hole 969D or as a result of normal faulting in the topographically high holes, the sequence preserved in Hole 969D appears to be expanded relative to the other holes (see "Composite Depths" section, this chapter).

A full list of the data collected from this site is given in Table 5.

Data

The Tensor orientation tool was run in all holes at this site. This allowed planar measurements made with respect to the core liner in Cores 160-969A-3H through 13H and 160-969E-3H through 11H to be corrected to geographic coordinates. Measurement of structures in three dimensions was not permitted in Holes 969B, 969C, and 969D because of the necessity of preserving intact sapropel sequences for post-cruise sampling. However, using the Tensor orientation data for the Hole 969D, it was possible to get an idea of the orientation of the

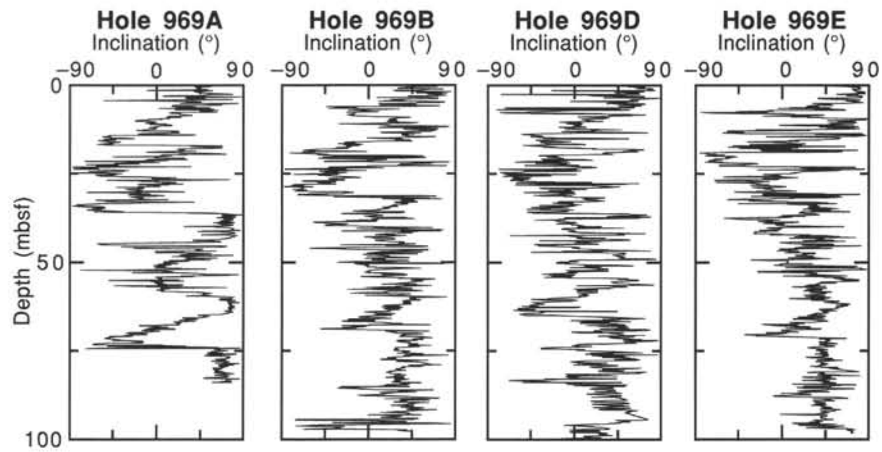

Figure 29. Paleomagnetic inclinations measured on archive-half cores using the shipboard pass-through magnetometer for Holes 969A, 969B, 969D, and 969E after AF demagnetization at 25 mT.

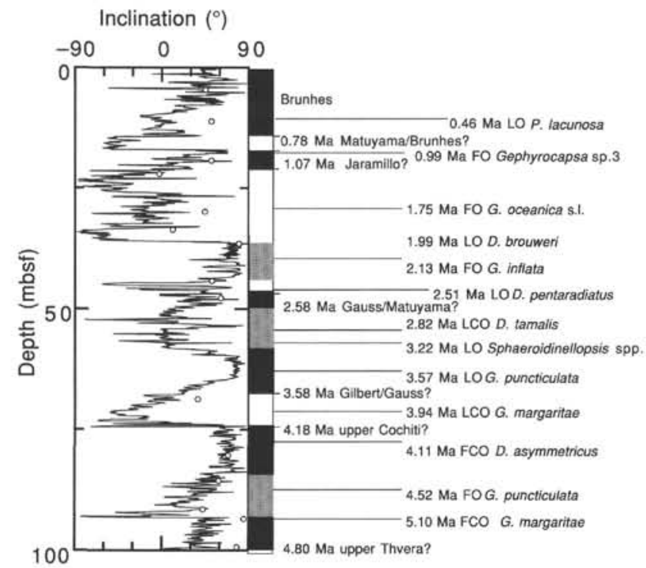

Figure 30. Whole-core paleomagnetic inclination data for Hole 969A (measured at 25 mT) compared with inclinations from stepwise-demagnetized discrete samples. Inclinations for discrete samples were determined by linear regression fits to multiple demagnetization points in each case. A preliminary polarity interpretation is shown on the right-hand side along with biostratigraphic datums.

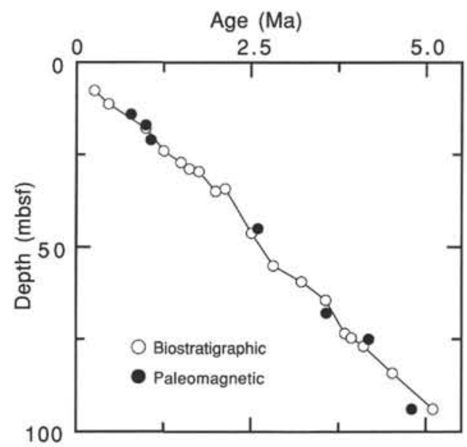

Figure 31. Age vs. depth plot for the preliminary magnetostratigraphic interpretation shown in Figure 30, compared with that obtained from the biostratigraphic datums for Hole 969A. The datums shown (from higher to lower in the sequence) are the interpreted positions of the Matuyama/Brunhes boundary, upper and lower Jaramillo polarity boundaries, Gauss/Matuyama boundary, Gilbert/Gauss boundary, and upper boundaries of the Cochiti and Thvera Subchrons.

dip direction both of bedding and faults from the apparent dip of these structures on the 90°–270° (core coordinates) plane of the core (see below).

Description of Structures

Sedimentary Bedding and Erosional Surfaces

Sedimentary bedding planes, identified by planar changes in color and grain size, showed a fairly consistent horizontal to subhorizontal orientation in Holes 969A and 969E (0°–10°). At certain intervals, however, a distinct tilt to the beds was observed (e.g., Cores 160-969A-2H and 3H and 160-969E-9H through 11H). In these intervals, the orientation of bedding planes is inconsistent over small stratigraphic distances (e.g., Section 160-969A-2H-6, 10–75 cm; Table 5) with dip angles varying from low to rare moderate angles. Figure 32 shows the geographic orientation of all bedding planes measured in cores from Holes 969A and 969E. The absence of any preferred orientation in this data set substantiates the observation of the variability of bedding planes within these cores.

From Core 160-969D-5H downward, slightly to moderately tilted bedding is visible on the core face (90°–270° plane). A distinct systematic increase in apparent dip of bedding, from shallowly (10°–25°) to moderately (20°–50°) dipping, was recognized with depth (see Table 5). Note, however, that geographic orientation of the 90°–270° plane of the core liner was not known prior to drilling so that the observation of increasing apparent dip downhole need not, and probably does not, reflect an increase in true dip of the beds. As a result of the sampling restrictions, it was not possible to measure a second apparent dip and calculate the true dips. In an attempt to derive some directional information from the apparent dip data, however, the 90°–270° plane of the core liner for each core in Hole 969D was reoriented to geographic coordinates using the Tensor data. It was then possible to assess the likely true dip direction from the two-dimensional dip direction of the bedding on the 90°–270° core face plane with a possible error of ±90°. Assuming that the tilts of the beds from Hole 969D were constant in dip direction, a first-order analysis of the reoriented 90°–270° core face planes and apparent dip lines from Cores 160-969D-5H through 12H show an overlap that can be tentatively interpreted to indicate that the bedding dips toward the northwest (Fig. 33). Cores 160-969D-1H through 3H contain few bedding planes that show apparent dips greater than 0°. Core 160-969D-13H

Table 5. Structural data collected at Site 969.

Core, section, interval (cm)	Depth (mbsf)	Feature	Offset width (cm)	Orientation on core face (degrees)		Second apparent orientation (degrees)		Calculated orientation (degrees)		Geographic orientation (degrees)		Comments
				Apparent dip	Direction	Apparent dip	Direction	Dip	Direction	Dip	Direction	
160-969A-												
2H-4, 12–16	12.32	SB		30	270	0	0	30	270			Underconsolidated ooze
2H-4, 17–18	12.37	SB		19	270	Not visible						Underconsolidated ooze
2H-5, 101–105	14.71	SB		35	270	4	0	35	277			
2H-6, 47–55	15.67	SB		56	90	0	293	75	23			
2H-6, 69–72	15.89	SB		20	270	8	0	21	291			Change in grain size
2H-6, 92–96	16.12	SB		36	270	46	180	52	215			
2H-6, 116–117	16.36	F?		10	90	15	0	18	33			
3H-1, 37–38	17.57	SB		15	270	9	0	17	301	17	176.5	
3H-1, 145–146	18.65	SB		20	90	28	0	33	34	33	269.5	Yellowish band
3H-2, 134–138	20.04	F?		75	270	0	55	81	325	81	200.5	Sense unknown

Note: Feature symbols defined in Table 2 ("Explanatory Notes" chapter, this volume).

Only part of this table is reproduced here. The entire table appears on the CD-ROM (back pocket).

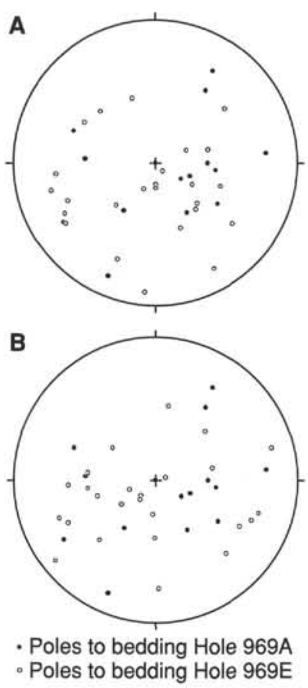

Figure 32. **A.** Equal-area lower hemisphere plot of the distribution of tilted bedding planes from Cores 160-969A-3H through 13H and 160-969E-3H through 11H with respect to the core coordinates. **B.** Equal-area lower hemisphere plot of the same data set after reorientation with respect to geographic coordinates using the Tensor tool data.

contains shallowly to moderately dipping beds that dip consistently toward 90° in the 90°–270° core face plane (Table 6), but, when reoriented to geographic coordinates, indicate a dip direction to the southwest.

Several intervals, some of which dip slightly to moderately, cut sedimentary bedding planes at low angles. These surfaces usually have a sharp basal contact and are believed to represent erosive discontinuities, as most of them are followed by upward-grading sequences. Some of the discontinuous boundaries are followed by debris-flow deposits that are centimeters to decimeters thick (e.g., Cores 160-969E-9H and 10H).

Normal Faults

The majority of the structures observed in Cores 160-969A-1H through 13H are high-angle normal faults, with dips between 55° and

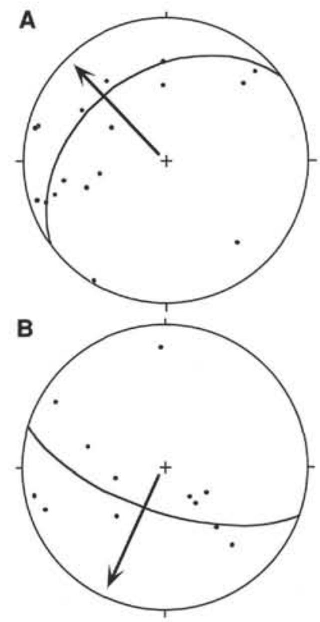

Figure 33. **A.** Poles on reoriented tilted bedding traces on the core face. The calculated best fit for these poles reflects their averaged direction of dip (arrow), at an angle of 52° toward 224°. **B.** Poles on reoriented apparent dips of fault traces on the core face, for which a preferred orientation and possible overlap of all data of 23° dip toward 198° was calculated. See text for discussion.

80° (Figs. 34A, B, 35A) and offsets from a few millimeters to more than 20 cm. Most measurements were taken from Cores 160-969A-10H and 11H (Table 5), but normal faults were also found at several intervals throughout the hole. Sets of closely packed normal faults, with dip angles varying from 60° to 80° along the same bed, were observed in some places (e.g., Section 160-969A-6H-5, 115–140 cm; Fig. 36).

Normal faults in Hole 969E have a wider range of dip angles than in Hole 969A, varying from 15° to 85°. The concentration of faults was also much lower and the offsets generally smaller (<1 cm; Table 5) than those observed in Hole 969A. When corrected with the Tensor tool data, the poles to the fault planes scatter and no systematic distribution pattern can be discerned (Figs. 33, 34B, D).

Reverse Faults

In Hole 969D, the faults show dominantly a reverse sense of movement and are concentrated over particular intervals (e.g., Sec-

Table 6. Structural data collected at Hole 969D providing the basis for reorientation of apparent dip on the 90°–270° core-face plane estimate of true dip (cf., Fig. 33).

Core	Depth (mbsf)	First apparent dip (degrees) Dip	Direction	Tensor (degrees)	Dip direction (±90°)	Comment
Sedimentary bedding:						
160-969D-						
3H	18.4	31	270	307	323	
4H	27.9	6	270	17	253	
		20	270			
5H	37.4	8	270	345	285	Estimated from core photograph
6H	46.9	6	270	246	284	
7H	56.4	2	270	49	211	Estimated from core photograph
8H	65.9	13	270	225	45	
		24	270			
9H	75.4	32	270	329	301	
		53	270			
10H	84.9	28	270	191	259	
		51	270			
11H	94.4	31	270	272	358	
		46	270			
12H	103.9			131	139	Not consistent
13H	112	12	90	18	251	
		41	90			
		10	270		71	Estimated from core photograph
Reverse faults:						
160-969D-						
3H	18.4			307	323	
4H	27.9			17	253	
5H	37.4	43	270	345	285	Offset = 8 cm
6H	46.9			246	284	
7H	56.4			49	211	
8H	65.9	50	90	225	225	Offset = 1.4 cm
9H	75.4	62	90	329	121	Offset = 2.1 cm
		12	270		301	Offset = 1.4 cm
10H	84.9	44	90	191	139	Offset < 1 cm
		7	270		258	Offset < 1 cm
	94.4	61	270			Offset < 1 cm
11H		17	90	272	358	
	103.9					
12H		63	270	131	139	Offset > 40 cm
	112	29	270			
		68	270			Offset > 30 cm
13H		12	270	18	251	
		51	270		251	Offset = 1 cm

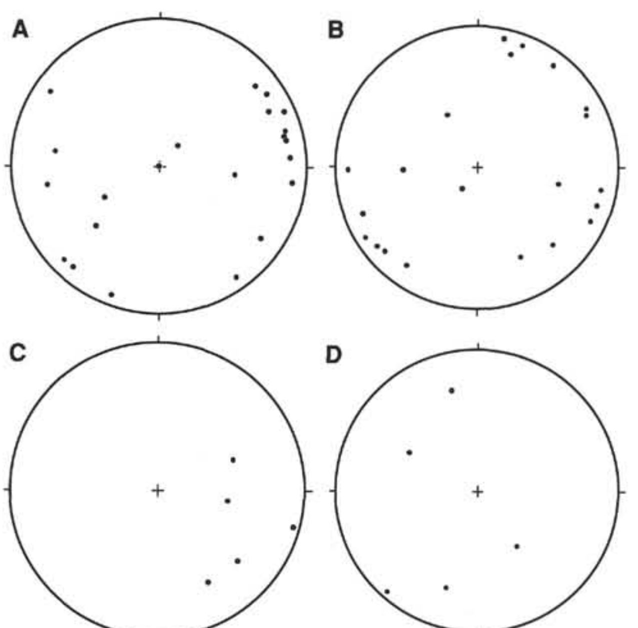

Figure 34. Stereographic projection of the distribution of normal fault pole data from Cores 160-969A-3H through 13H with respect to the core coordinates (**A**) and the geographic coordinates after reorientation using Tensor tool data (**B**). Equal-area lower hemisphere plot of poles to reverse faults of Cores 160-969E-3H through 11H with respect to the core liner (**C**) and in geographic coordinates (**D**).

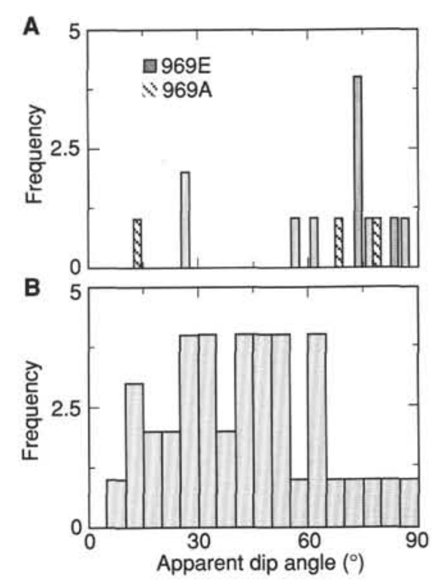

Figure 35. **A.** Distribution of apparent dip angles of normal microfaults in Holes 969A and 969E. **B.** Distribution in Hole 969D of apparent dip angles of faults, which have a dominantly reverse sense of movement (cf., Table 5).

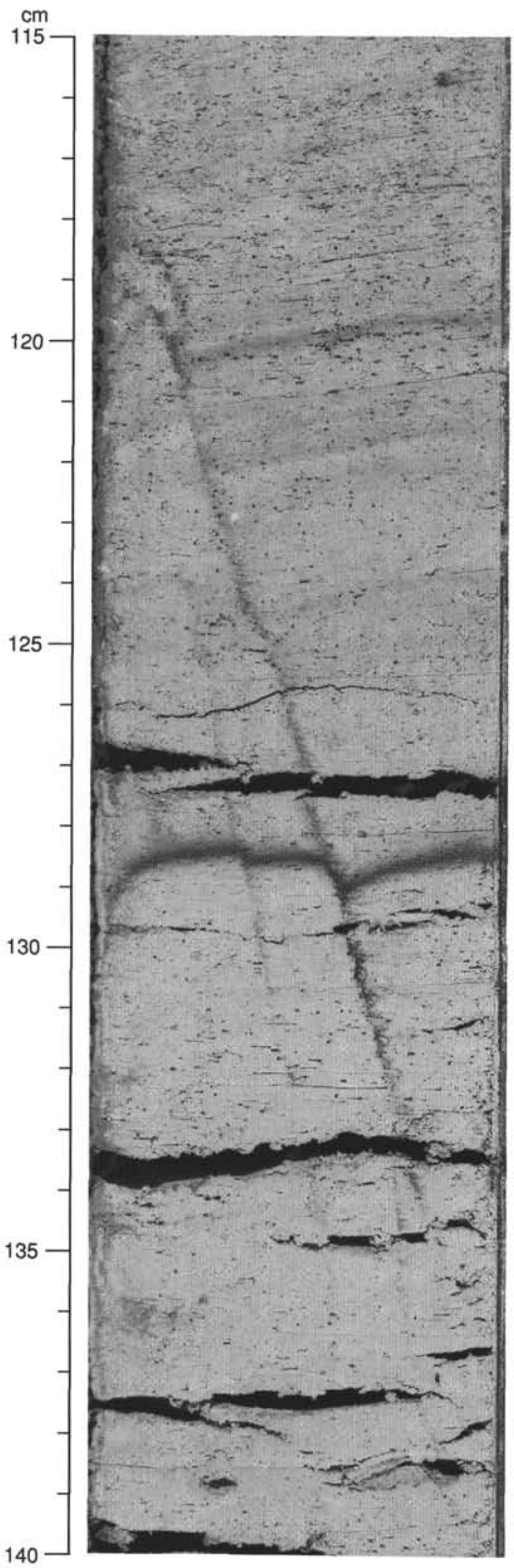

Figure 36. Steeply dipping normal faults offsetting a dark gray, sulfide-rich band at Section 160-969A-6H-5, 115–140 cm. The trace of the fault plane is marked by the appearance of sulfide.

tions 160-969D-10H-3, 12H-2, 12H-3, and 13H-1). Multiple intervals of these structures are visible where slight color variations of the sediments or burrows permit small (generally <1 cm) offsets to be seen. In general, the dip angle of the reverse faults is significantly lower than for normal faults elsewhere at this site (Fig. 35B). The dips of these reverse faults appear to vary systematically along single layers such that the boundary of an individual slice where it forms the footwall of a fault is steeper than the boundary of the same slice where it forms the hanging wall of the next thrust (Fig. 37). As all the faults dip in the same direction with respect to the core face, this relationship appears to resemble an imbricate fan of faults.

A similar approach to that described above for the approximate orientation of bedding planes, where only apparent dips are available, was used to obtain an estimate of the true dip direction of the reverse faults. The initial assumption made was that the dip direction of the faults does not vary from fault to fault (Fig. 37). Additionally, it was assumed that the true dip directions may lie close to the apparent dip directions measured, even if they range 90° to each direction. On this basis, reorientation of the fault traces on the core face using the Tensor measurements provided an estimate of possible true dip directions (180° range) of the fault planes (Fig. 33B). The calculated best fit of all reoriented apparent dip measurements reveals an area where all data overlap (see arrow in Fig. 33B). This means that the distribution of faults seen on the core face could be explained by a generally consistent trend of dip directions toward the southwest. It has to be pointed out that the aim of this data manipulation was just to test the hypothesis if the structural observations fit into the tectonic framework of the region (see below).

Interpretation

The varied orientation and dip angle of bedding planes observed in Holes 969A and 969E probably reflect the interplay between post- and syndepositional tectonic tilt. Interpretation of the bedding data from Hole 969D is more difficult, given the lack of orientation. An apparently thicker sedimentary sequence would be recorded if the dip direction of the bedding in Hole 969D has a relatively high angle (see "Lithostratigraphy" section, this chapter), which would provide an explanation for Unit II not being drilled in this hole. However, given the anomalous dip direction of bedding in Core 160-969D-13H compared to Cores 160-969D-5H through 12H, the assumption of constant dip appears doubtful at least for the bottom of the hole. In the context of the varied dip directions of faults in Hole 969A and 969E, it seems more likely that a significant part of the sequence (possibly Cores 160-969D-5H through 12H) recovered in Hole 969D may be affected by the same tectonic tilt, although other tilt directions were also recorded.

In addition, only the sapropel-bearing succession in Hole 969D represents a record that is comparable to the previous sites (see "Lithostratigraphy" section, this chapter). Because of that limitation, parts of the layered sediment succession in Holes 969A, 969B, and 969E are missing and probably faulted out along normal microfaults.

The three-dimensional normal fault data for Holes 969A and 969E show no clear distribution pattern when corrected for geographic orientation (Fig. 34). These observations suggest that either no systematic tectonic signature is recorded in the faults or the fault population contains some drilling-induced structures that mask the tectonic signature (see "Structural Geology" section, chapters for Sites 964, 966, 967, and 968, this volume). The presence of compressional faulting in the topographically lowest hole (Hole 969D) and its nearly complete absence in the elevated holes (Holes 969A, 969B, 969C, 969E, and 969F) suggest that shortening is preferentially taken up within the slope area.

Interpretation of the shipboard seismic data at this site is difficult, but one possibility is that a southwest-dipping thrust is located in the slope region of the ridge, although some possible collapse features can be seen at depth beneath the ridge itself (see Fig. 5 and "Site Geophysics" section, this chapter).

Although the southwest dip direction of the reverse faults in Hole 969D is only tentatively inferred from two-dimensional data, it is possible that these faults parallel the fault discerned on the seismic profile. Normal faulting in the ridge-top cores may have been generated either as a result of collapse or as minor tectonic structures associated with formation of the ridge itself.

In summary, Site 969 contains a variety of features that reflect the structural complexity of the area. Where it was possible to determine bedding-plane dip directions in three dimensions, they vary considerably, suggesting both tectonic tilt and sedimentary slope activity. The holes in the elevated area of the ridge record mainly extensional stress, whereas the sediments recovered from Hole 969D reflect a rather different tectonic microenvironment (and possibly on a larger scale, too), affected by mainly compression on the southwestern flank of the small ridge.

COMPOSITE DEPTHS

High-resolution (2–10-cm scale) data collected on whole cores on the MST and percent color reflectance collected on split cores from Holes 969A through 969E were used to determine depth offsets in the composite section. On the composite depth scale, sedimentary features present in adjacent holes were aligned so that they occur at approximately the same depth. Working from the top of the sedimentary sequence, a constant was added to the depth in meters below seafloor for each core in each hole to arrive at a composite depth for that core. The depth offsets that form the composite depth section are given in Table 7.

Percent color reflectance (collected at 2-cm intervals) and magnetic susceptibility data (collected at 3-cm intervals) were the primary parameters used for correlation purposes at this site. Natural gamma-ray data (collected at 10-cm intervals) and GRAPE wet-bulk density data (collected at 2-cm intervals) provided supplementary verification of core overlap and depth offsets. The percent color reflectance records (550-nm wavelength) and magnetic susceptibility data used to verify core overlap of the sedimentary section at Site 969 are shown on a composite depth scale in Figures 38 and 39, respectively. The sequences recovered from all the holes were affected to a varying extent by faulting and tilting, which resulted in localized difficulties in interhole correlation. The sequence below Core 2H in each of Holes 969A, 969B, and 969E differs markedly from that recovered from Hole 969D (see "Lithostratigraphy" section, this chapter). In comparison to the other sites drilled on Leg 160, Hole 969D appears to be the most complete sequence. However, significant depth offsets (more than 10 m) of equivalent layers occur between Hole 969D and the other holes. In addition, equivalent lower to middle Pliocene sapropels in Hole 969D appear much thicker than in the other holes as a result of drilling Hole 969D through tilted beds. Thus, it was not possible to put Hole 969D (below Core 160-969D-2H) into a composite section with the other holes without significant stretching and squeezing of the section.

Continuity of the sedimentary sequence, in terms of core overlap, was documented for the intervals 0–17 and 26–90 mcd in Holes 969A, 969B, 969C (one core), and 969E. Interhole comparison of MST and color reflectance data could not verify complete overlap in the intervals from 17 to 26 and 90 to 110 mcd in these holes but could not discount it either, as no apparent gap exists in the data.

The lack of verifiable overlap and continuity between 17 and 26 mcd (Cores 3H and 4H in Holes 969A, 969B, and 969C; uppermost Pliocene to lower Pleistocene) is most likely the result of partial shearing or faulting out of portions of the sedimentary sequence in each of the holes (see "Lithostratigraphy" and "Structural Geology" sections, this chapter). Correlation is also difficult in the lower Pliocene section (below 90 mcd) owing to faulting and to pull-out

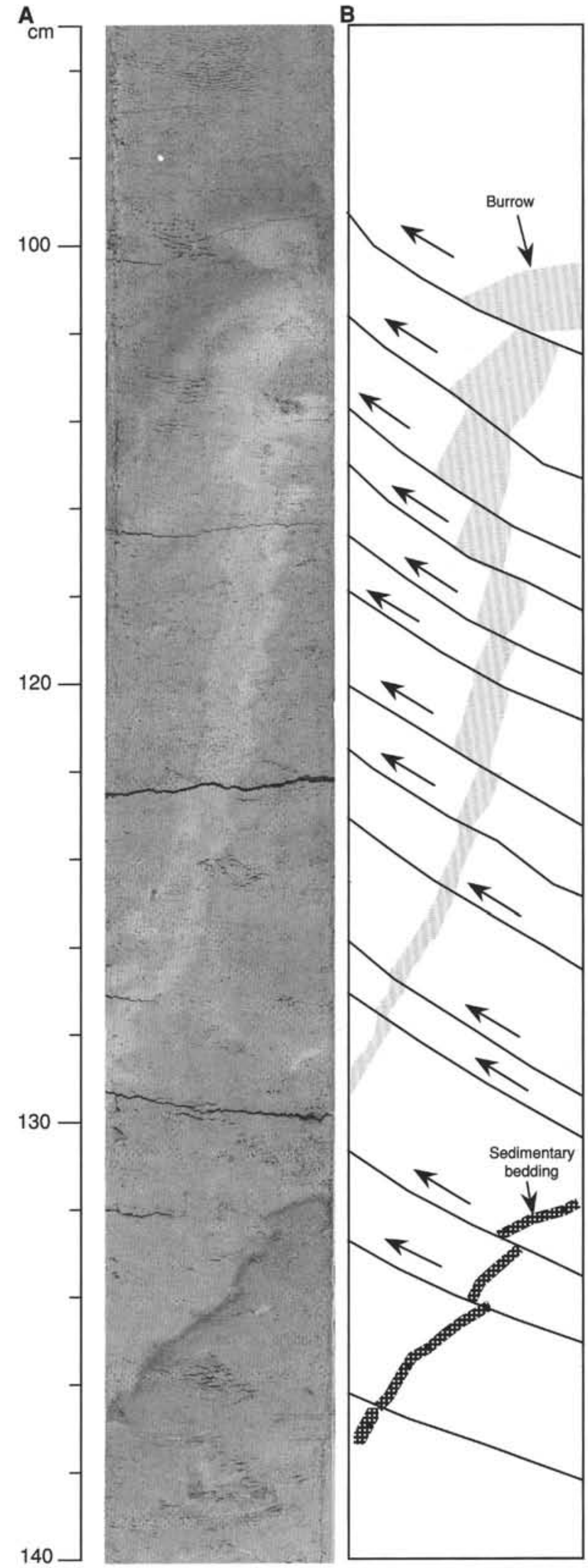

Figure 37. **A.** Fanlike reverse faulting of several centimeter-thick layers from Section 160-969D-10H-3, 95–140 cm. Each of the reverse microfaults offsets a burrow filled with very light gray ooze by a few millimeters to centimeters. **B.** Sketch of the same feature, including the identified fault planes and their relative sense of movement.

Table 7. Site 969 composite depth section.

Core	Depth (mbsf)	Offset (m)	Depth (mcd)	Core	Depth (mbsf)	Offset (m)	Depth (mcd)
160-969A-				160-969D-			
1H	0.00	0.09	0.09	1H	0.00	0.26	0.26
2H	7.70	0.32	8.02	2H	8.90	0.80	9.70
3H	17.20	1.17	18.37	3H	18.40	0.80	19.20
4H	26.70	2.48	29.18	4H	27.90	0.80	28.70
5H	36.20	2.80	39.00	5H	37.40	0.80	38.20
6H	45.70	3.05	48.75	6H	46.90	0.80	47.70
7H	55.20	3.38	58.58	7H	56.90	0.80	57.70
8H	64.70	3.73	68.43	8H	65.90	0.80	66.70
9H	74.20	5.36	79.56	9H	75.40	0.80	76.20
10H	83.70	7.44	91.14	10H	84.90	0.80	85.70
11H	93.20	8.28	101.48	11H	94.40	0.80	95.20
12H	102.70	8.28	110.98	12H	103.90	0.80	104.70
13H	105.50	8.28	113.78	13H	112.00	0.80	112.80
160-969B-				160-969E-			
1H	0.00	0.05	0.05	1H	0.00	0.00	0.00
2H	2.90	0.62	3.52	2H	4.90	0.44	5.34
3H	12.40	2.04	14.44	3H	14.40	3.64	18.04
4H	21.90	2.58	24.48	4H	23.90	3.82	27.72
5H	31.40	3.57	34.97	5H	33.40	4.60	38.00
6H	40.90	5.24	46.14	6H	42.90	6.30	49.20
7H	50.40	6.44	56.84	7H	52.40	6.95	59.35
8H	59.90	7.45	67.35	8H	61.90	8.33	70.23
9H	69.40	7.84	77.24	9H	71.40	10.18	81.58
10H	78.90	8.44	87.34	10H	80.90	11.06	91.96
11H	88.40	12.68	101.08	11H	88.40	12.88	101.28
160-969C-							
1H	0.00	4.42	4.42				

(suction) effects produced during APC coring that affected many sections in the last two cores of Holes 969A and 969B.

In contrast to Holes 969A, 969B, 969C, and 969E, the sequence recovered from Hole 969D appears intact and undeformed (see "Lithostratigraphy" and "Biostratigraphy and Sedimentation Rates" sections, this chapter). The upper Pleistocene sequence (Cores 160-969D-1H and 2H) is somewhat thinner but can be placed into the composite section (Table 7). The upper Pliocene to lower Pleistocene sequence (Cores 160-969D-3H through 5H) contains 31 apparently undeformed sapropels in 40 m of sediment, the same number found at other Leg 160 sites within this time interval. The two middle Pliocene sapropel packets (Cores 160-969D-6H and 7H) are also present, but appear thicker as a result of drilling through tilted beds. Several sapropels appear to be missing between the core breaks in Hole 969D.

Stretching and compression of the sedimentary features in aligned cores indicate distortion of the cored sequence resulting from coring disturbance, faulting, and shearing. All these phenomena are especially evident when comparing Hole 969D with the other holes. As with the other Leg 160 sites, much of the distortion occurs within individual cores on depth scales of less than 9 m and it was not possible to align many features in the color reflection and magnetic susceptibility records accurately by simply adding a constant to the mbsf core depth. Additional correlation problems arose at this site as a result of the large difference in apparent sedimentation rates between Hole 969D and the other holes. Correlation between features in Hole 969D (below Core 160-969D-2H) and the other sites cannot be achieved without significant stretching and squeezing of the sections. Within-core depth-scale changes as well as these much larger core-to-core depth offsets will require post-cruise processing to align many sedimentary features and to determine the extent of missing section in coring gaps at Hole 969D.

Following construction of the composite depth section for Site 969, two different spliced records were assembled from the aligned cores. The Site 969 spliced records can be used as sampling guides to recover a single sedimentary sequence. The first spliced record consists of cores from Holes 969A, 969B, 969C, and 969E. Intervals with significant disturbance or distortion were avoided where possible. The tie points for the splice are given in Table 8. As within-core distortion was considerable at this site (especially between 15 and 30 mcd and 90 and 100 mcd), a small (20 cm) depth discrepancy may result when comparing composite depths generated from the offset depth table (Table 7) with composite depths of a single downcore record (e.g., percent color reflectance) generated using the splice table (Table 8). This discrepancy results from within-core misalignments of the stratigraphic features used to make the splice. The second spliced record (Table 9) consists of the apparently more complete upper Pliocene to Pleistocene record of Cores 160-969D-1H through 6H tied to the middle Pliocene to lower Pliocene record of cores from Holes 969A, 969B, and 969D. Both splices are most likely incomplete in the upper Pliocene to lower Pleistocene portions (Cores 2H–5H in all holes). The first splice (Table 8) contains faulted and sheared sections throughout this interval whereas the second splice (Table 9) has coring gaps and, thus, missing sections within this same interval.

INORGANIC GEOCHEMISTRY

Thirteen interstitial-water samples were obtained at Site 969 from 5.95 to 107.7 mbsf, using the standard ODP titanium/stainless-steel squeezer (Manheim and Sayles, 1974), and subsequently analyzed for salinity, alkalinity, chloride, sulfate, lithium, potassium, calcium, magnesium, strontium, ammonium, and silica using methods described in the "Explanatory Notes" chapter (this volume). The results are listed in Table 10.

Organic Matter Degradation

The degradation of sedimentary organic matter at Site 969 is not reflected in a significant sulfate depletion. However, it is possible that such a process is obscured by a diffusive flux of sulfate from greater depth (see below). The concentration of ammonium increases steadily with depth, indicating continuing degradation of organic matter and the resulting production of ammonium and bicarbonate (i.e., alkalinity) (Fig. 40). A small fraction of the ammonium is fixed by minerals, which release some lithium to the pore water by ion exchange. The initial increase of the lithium pore-water concentration with depth corresponds to such a process (Fig. 40). However, most of the lithium increase, and in particular the rather abrupt increase near the bottom of Hole 969A, seems to result from the upward diffusion of lithium and other evaporite-related elements (see below).

After the initial increase in alkalinity in the top few meters from a bottom-water value of 2.5 to 3.2 meq/L at 6 mbsf, it gradually decreases to a value of 1.2 meq/L at the bottom of this hole. This decrease is most likely the result of recrystallization and/or precipitation of carbonate phases (see below).

The concentration of silica in the pore water initially increases from a bottom-water value of 10–15 μM to 325 μM at 6 mbsf (Fig. 41). Subsequently, its concentration decreases sharply to an almost constant level with depth of 150 μM. The initial abrupt increase in silica concentration is related to early diagenetic reactions involving the dissolution of amorphous silica phases. Radiolarians were observed in Core 160-969A-1H (see "Biostratigraphy and Sedimentation Rates" section, this chapter). The almost-constant silica levels of 150 μM in the pore waters below this depth interval reflect equilibrium with clay minerals and/or quartz.

Carbonate Diagenesis

Alkalinity consumption is evident from the pore-water profile of Site 969, which is related to the precipitation of a carbonate phase or to intense alteration of volcanogenic material below a depth of 6 mbsf (Gieskes, 1981, 1983). Because the abundance of the ash layers does

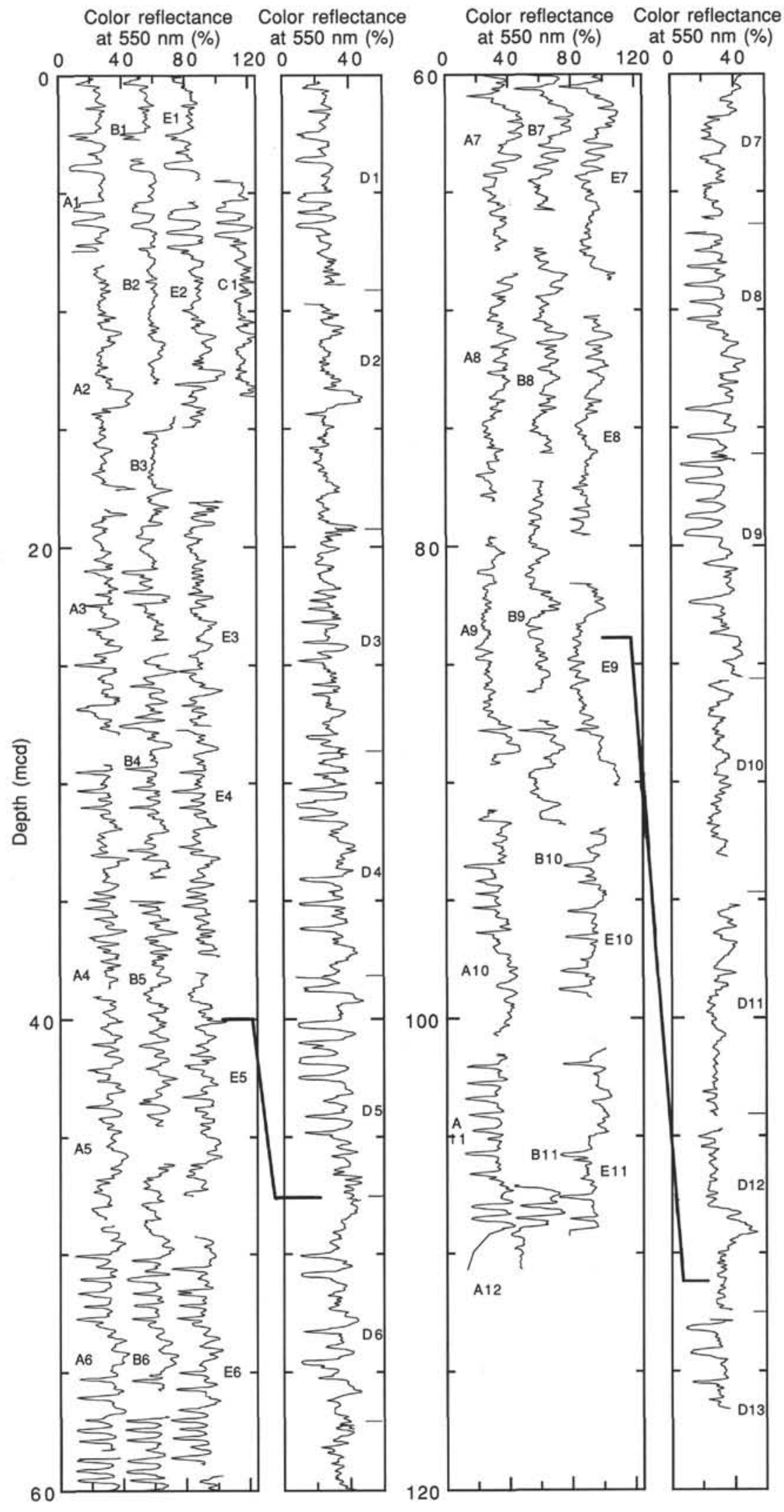

Figure 38. Percent color reflectance (550-nm wavelength) from Site 969 on the composite depth scale. Holes 969A, 969B, 969C, and 969E are offset from each other by a constant (30%). Cores for each hole are shown (e.g., B2 = Core 160-969B-2H). The tie lines show equivalent stratigraphic intervals.

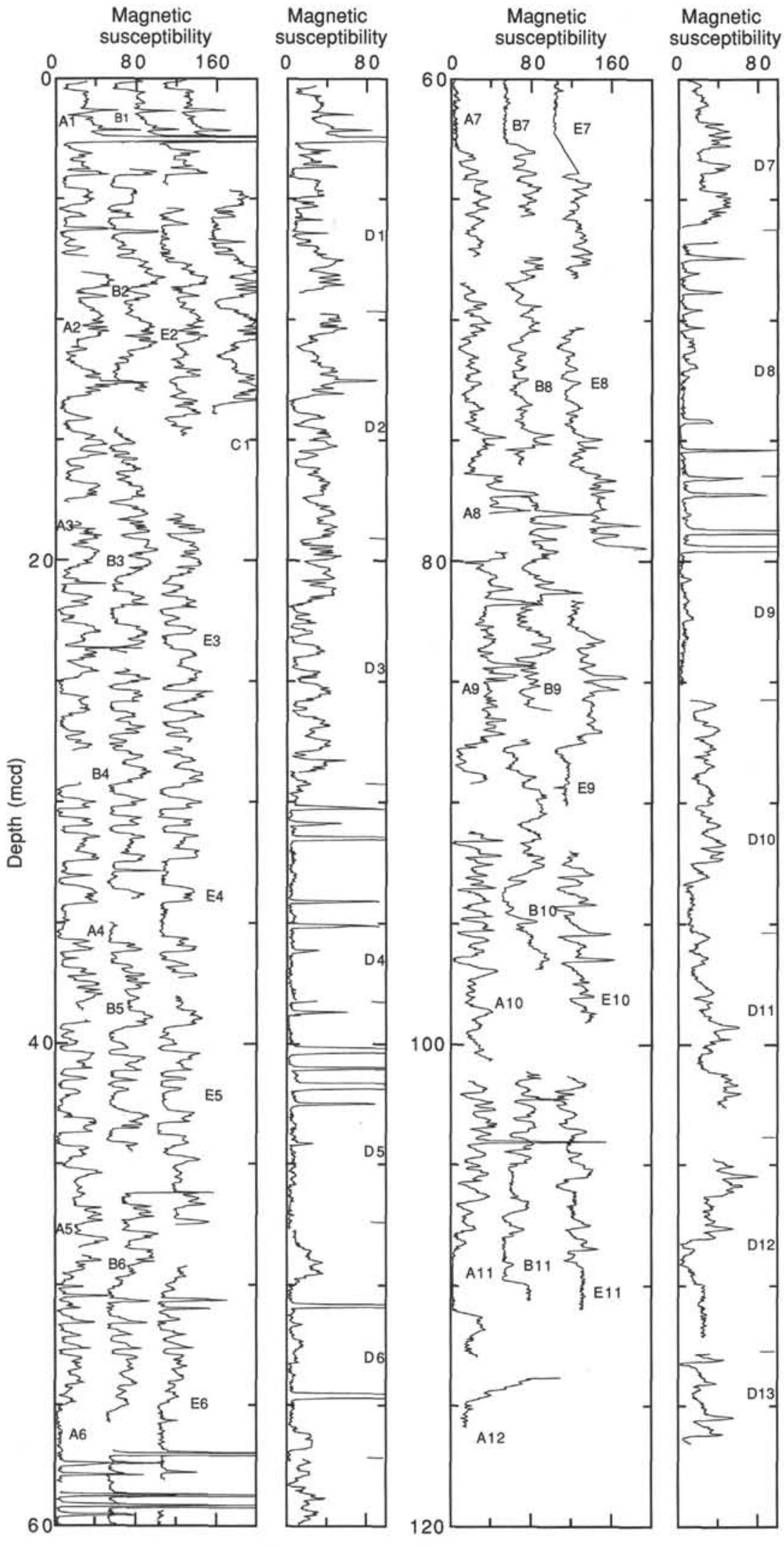

Figure 39. Magnetic susceptibility data (uncorrected instrument units) from Site 969 on the composite depth scale. Holes 969A, 969B, 969C, and 969E are offset from each other by a constant (50 instrument units). Cores for each hole are shown (e.g., B2 = Core 160-969B-2H).

Table 8. Site 969 splice tie points for Holes 969A, 969B, 969C, and 969E.

Hole, core, section, interval (cm)	Depth (mbsf)	Depth (mcd)		Hole, core, section, interval (cm)	Depth (mbsf)	Depth (mcd)
969A-1H-4, 110.0	5.60	5.69	ties to	969C-1H-1, 126.0	1.26	5.69
969C-1H-4, 66.0	5.16	9.59	ties to	969A-2H-2, 6.0	9.26	9.59
969A-2H-7, 52.0	17.22	17.55	ties to	969B-3H-3, 12.0	15.52	17.55
969B-3H-5, 44.0	18.84	20.87	ties to	969A-3H-2, 100.0	19.70	20.86
969A-3H-6, 64.0	25.34	26.50	ties to	969B-4H-2, 52.0	23.92	26.50
969B-4H-4, 104.0	27.44	30.02	ties to	969A-4H-1, 84.0	27.54	30.02
969A-4H-6, 68.0	34.88	37.36	ties to	969B-5H-2, 88.0	33.78	37.36
969B-5H-4, 62.0	36.52	40.10	ties to	969A-5H-1, 110.0	37.30	40.10
969A-5H-6, 48.0	44.18	46.98	ties to	969B-6H-1, 84.0	41.74	46.98
969B-6H-2, 140.0	43.80	49.04	ties to	969A-6H-1, 28.0	45.98	49.04
969A-6H-6, 146.0	54.40	57.46	ties to	969B-7H-1, 18.0	50.58	57.46
969B-7H-3, 78.0	54.18	61.06	ties to	969E-7H-1, 118.0	53.58	61.06
969E-7H-6, 126.0	61.16	68.64	ties to	969B-8H-1, 94.0	60.84	68.64
969B-8H-2, 58.0	61.98	69.78	ties to	969A-8H-1, 92.0	65.62	69.78
969A-8H-7, 24.0	73.94	78.10	ties to	969B-9H-1, 82.0	70.22	78.10
969B-9H-2, 132.0	72.22	80.10	ties to	969A-9H-1, 38.0	74.58	80.10
969A-9H-6, 60.0	82.30	87.82	ties to	969B-10H-1, 32.0	79.22	87.82
969B-10H-3, 114.0	83.04	91.64	ties to	969A-10H-1, 50.0	84.20	91.64
Append Core 160-969A-11H to Core 160-969A-10H						

Table 9. Site 969 splice tie points for Holes 969A, 969B, 969D, and 969E.

Hole, core, section, interval (cm)	Depth (mbsf)	Depth (mcd)		Hole, core, section, interval (cm)	Depth (mbsf)	Depth (mcd)
Append Core 160-969D-2H to 160-969D-1H						
Append Core 160-969D-3H to 160-969D-2H						
Append Core 160-969D-4H to 160-969D-3H						
Append Core 160-969D-5H to 160-969D-4H						
Append Core 160-969D-6H to 160-969D-5H						
969D-6H-2, 46.0	48.86	49.66	ties to	969B-5H-4, 14.0	36.04	49.66
969B-5H-4, 62.0	36.52	50.14	ties to	969A-5H-1, 110.0	37.30	50.14
969A-5H-6, 48.0	44.18	57.02	ties to	969B-6H-1, 84.0	41.74	57.02
969B-6H-2, 140.0	43.80	59.08	ties to	969A-6H-1, 28.0	45.98	59.04
969A-6H-6, 146.0	54.40	67.50	ties to	969B-7H-1, 18.0	50.58	67.50
969B-7H-3, 78.0	54.18	71.10	ties to	969E-7H-1, 118.0	53.58	71.10
969E-7H-6, 126.0	61.16	78.68	ties to	969B-8H-1, 94.0	60.84	78.68
969B-8H-2, 58.0	61.98	79.82	ties to	969A-8H-1, 92.0	65.62	79.82
969A-8H-7, 24.0	73.94	88.14	ties to	969B-9H-1, 82.0	70.22	88.14
969B-9H-2, 132.0	72.22	90.14	ties to	969A-9H-1, 38.0	74.58	90.14
969A-9H-6, 60.0	82.30	97.86	ties to	969B-10H-1, 32.0	79.22	97.86
969B-10H-3, 114.0	83.04	101.68	ties to	969A-10H-1, 50.0	84.20	101.68
Append Core 160-969D-11H to 160-969D-10H						

Table 10. Results of pore-water analysis for Site 969.

Core, section, interval (cm)	Depth (mbsf)	pH	Alkalinity (meq/L)	Salinity (g/kg)	Cl^- (mM)	Mg^{2+} (mM)	Ca^{2+} (mM)	SO_4^{2-} (mM)	NH_4^+ (μM)	SiO_2 (μM)	K^+ (mM)	Sr^{2+} (μM)	Li^+ (μM)	Na^+ (mM)
160-969A-														
1H-4, 145–150	5.95	7.55	3.277	38.5	630	60.0	16.5	29.3	136	323	12.5	147	39	584
2H-4, 145–150	13.65	7.66	2.660	39.0	636	61.0	12.8	29.5	185	149	12.6	174	42	542
3H-4, 140–150	23.10	7.52	2.283	40.5	657	61.8	13.5	30.9	263	135	13.0	221	47	566
4H-4, 140–150	32.60	7.46	2.159	41.8	678	64.5	16.5	31.1	330	130	13.4	252	55	579
5H-4, 140–150	42.10	7.26	2.087	44.0	702	65.9	19.2	32.3	395	127	13.0	286	64	595
6H-4, 140–150	51.34	7.42	1.882	45.0	726	66.4	21.7	31.8	445	173	13.4	329	76	614
7H-4, 140–150	61.10	7.37	1.734	47.0	750	71.0	26.5	33.6	500	135	13.8	361	89	621
8H-4, 140–150	70.60	7.35	1.546	48.0	782	77.2	28.4	36.3	610	154	14.1	376	105	647
9H-4, 140–150	80.1	7.28	1.504	50.5	806	80.5	31.8	37.6	620	140	14.3	403	124	662
10H-4, 140–150	89.60	7.35	1.392	52.8	839	84.5	37.3	40.1	705	162	15.2	443	145	699
11H-4, 140–150	99.10	7.18	1.183	54.7	864	85.6	39.9	39.8	790	175	15.3	456	165	705
12H-2, 73–80	103.68	—	—	57.7	903	90.6	42.6	41.0	775	114	16.5	505	193	727
13H-2, 70–75	107.70	—	—	60.2	936	93.6	51.8	49.2	—	—	17.9	519	217	752

Note: — = no data.

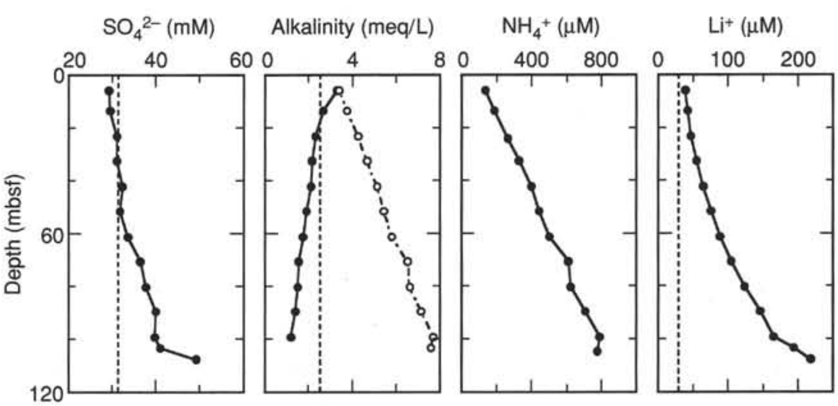

Figure 40. Pore-water vs. depth profiles at Hole 969A for sulfate, observed (solid symbols) and calculated (open symbols) alkalinity, ammonium, and lithium. The dashed line indicates the bottom-water concentration; the ammonium bottom-water concentration is <1 μM.

not increase with depth (see "Lithostratigraphy" section, this chapter) and a corresponding increase in magnesium is not discernible, the alteration of ash cannot be of importance (see also below).

Assuming a Redfield C/N ratio of 6.6 for the decomposition of organic matter, we have calculated the expected alkalinity from the ammonium pore-water profile (Fig. 40) in the same manner as at previous sites (see, e.g., "Inorganic Chemistry" section, "Site 963" chapter, this volume). The difference between the calculated and observed alkalinity values of more than 3.4 mM at 100 mbsf is not reflected in any corresponding decreases in the pore-water profiles of calcium and magnesium. In contrast, the concentration of calcium increases with depth. The calculated amount of Ca/Mg carbonate precipitation is negligible compared to the observed increases in the calcium, strontium, and magnesium concentrations in the lower part of this site (Fig. 42). These increases seem to be related to the upward diffusion of calcium and other alkali and alkaline earth elements (see below). Carbonate recrystallization and precipitation processes are reflected only in the shape of the depth profiles of calcium, strontium, calcium/chloride ratio, and strontium/chloride ratio (Figs. 41, 42).

Evaporite-related Fluxes

Salinity, chloride, and sodium concentrations increase from typical Mediterranean bottom-water concentrations to values that are more than 80% higher at 100 mbsf (Fig. 43). The concentration increases from 6 to 100 mbsf are rather gradual, whereas from 100 mbsf downward the increases are much sharper. Such a change in concentration gradient is most likely caused by a change in lithology. A less permeable layer may cause such inflections in diffusion-controlled profiles of conservative pore-water constituents. However, the

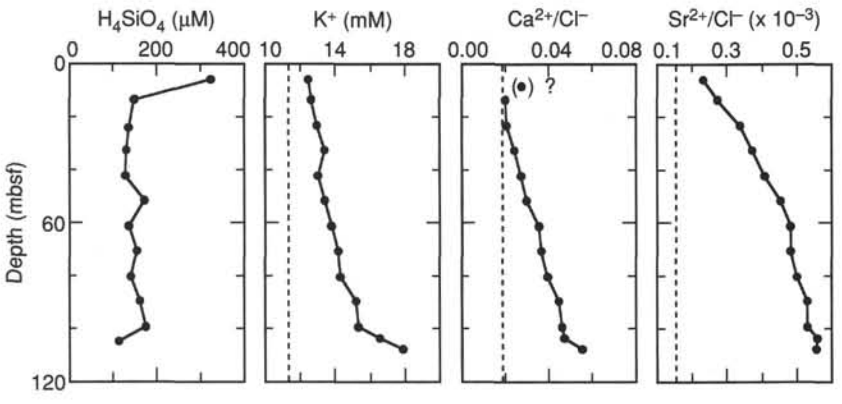

Figure 41. Pore-water vs. depth profiles at Hole 969A for silica, potassium, calcium/chloride ratio, and strontium/chloride ratio. The dashed line indicates the bottom-water concentration. The anomalous value in parentheses with a question mark is not well understood at this time.

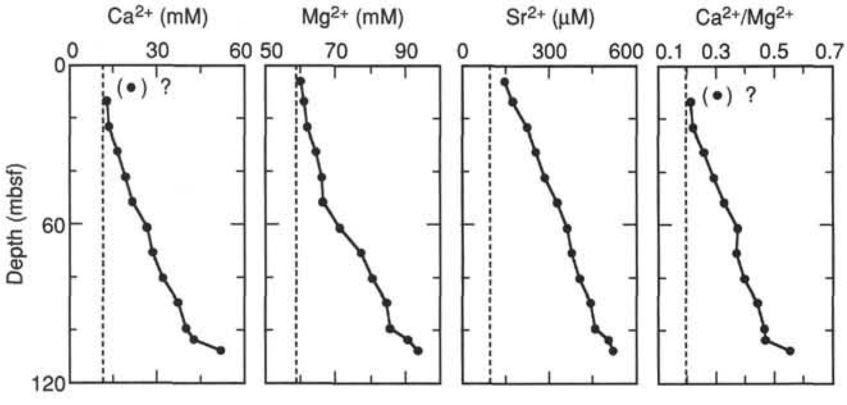

Figure 42. Pore-water vs. depth profiles at Hole 969A for calcium, magnesium, strontium, and calcium/magnesium ratio. The dashed line indicates the bottom-water concentration. The anomalous samples marked by parentheses and a question mark are not well understood at this time.

profiles could as well be explained by the presence of a relatively coarse-grained interval, permitting lateral flow that locally may prevail over the generally diffusion-controlled profiles. The increase in chloride is accompanied by increases in magnesium, calcium, strontium, sodium, lithium, and potassium and a distinct decrease in silica (Figs. 40–43). Usually, a gradual decrease is observed in the potassium concentration vs. depth in marine sediments (see "Inorganic Geochemistry" section, "Site 963" chapter, this volume). Similar uptake reactions probably take place at Site 969. However, this process is masked by a major upward flux of potassium from a deeper source in the sediments. The relatively large increases especially of lithium, potassium, and sulfate point to the presence of a late-stage evaporite brine at some depth below this site.

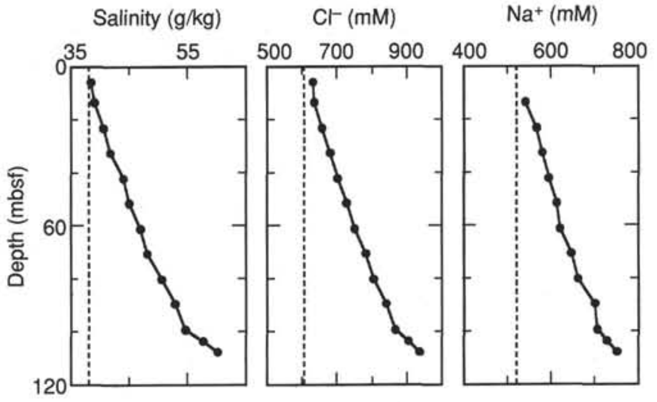

Figure 43. Pore-water vs. depth profiles at Hole 969A for salinity, chloride, and sodium. The dashed line indicates the bottom-water concentration.

ORGANIC GEOCHEMISTRY

Volatile Hydrocarbons

As part of the shipboard safety and pollution-prevention monitoring program, hydrocarbon gases were analyzed in all cores of Hole 969A by the headspace technique. Only trace concentrations of methane were recorded ranging from 2 to 4 ppm.

Carbonate and Organic Carbon

The abundances of total, inorganic, and organic carbon and of calcium carbonate in sediments from Hole 969A are summarized in Table 11. Random sampling was performed for carbonate analysis. For organic matter assessment, samples were specifically taken from the sapropels.

Carbonate content varies from 1% to 80% and averages 54% (134 samples analyzed). About 70% of the samples analyzed have a carbonate content between 60% and 80% (Fig. 44). Carbonate content in the sapropels is highly variable, but not related to depth.

Organic carbon was preferentially determined for visually distinguished organic-matter-rich intervals. Values are higher than 2% in most of the sapropels and reach a maximum of 30.5%, which is, to our knowledge, the highest organic carbon content ever measured in a Mediterranean sapropel. There is an assemblage of particularly organic-matter-rich sapropels in Cores 160-969A-6H and 7H (Table 11, Fig. 44). The black layer at 63–64 cm in Section 160-969A-3H-3 is unusual in that it apparently contains organic matter that, from its analytical data, resembles burnt wood (charcoal). Despite the organic carbon content of about 17%, elemental analysis failed to detect significant amounts of hydrogen, nitrogen, and sulfur. Rock-Eval pyrol-

Table 11. Concentration of total, inorganic, and organic carbon, calcium carbonate, total nitrogen, and sulfur in sediments from Hole 969A.

Core, section, interval (cm)	Depth (mbsf)	Total carbon (%)	Inorganic carbon (%)	Organic carbon (%)	$CaCO_3$ (%)	Nitrogen (%)	Sulfur (%)	C_{org}/N	C_{org}/S
160-969A-									
1H-1, 29–30	0.29	8.94	6.08	2.86	50.6	0.23	1.39	12.4	2.1
1H-1, 69–71	0.69		6.81		56.7				
1H-2, 69–70	2.19		4.99		41.6				
1H-2, 98–99	2.48	0.08	0.08	0.00	0.7	0.00	0.00		
1H-2, 112–113	2.62	9.92	6.28	3.64	52.3	0.26	2.01	14.1	1.8
1H-3, 24–25	3.24	7.63	4.54	3.09	37.8	0.22	1.37	14.3	2.3
1H-3, 39–40	3.39		6.10		50.8				
1H-4, 75–76	5.25		6.39		53.2				
1H-4, 103–104	5.53	10.47	6.54	3.93	54.5	0.25	1.76	15.7	2.2
1H-4, 128–129	5.78		6.72		56.0				
1H-5, 17–18	6.17	13.99	6.17	7.82	51.4	0.46	2.38	17.0	3.3
1H-5, 76–77	6.76		6.08		50.6				
1H-5, 112–113	7.12	9.09	5.69	3.40	47.4	0.22	2.04	15.3	1.7
2H-1, 76–77	8.46		8.49		70.7				
2H-1, 138–139	9.08		5.42		45.1				
2H-2, 122–123	10.42		6.64		55.3				
2H-3, 135–136	12.05		6.99		58.2				
2H-4, 135–136	13.55		9.54		79.5				
2H-5, 36–37	14.06		7.22		60.1				
2H-5, 122–123	14.92		6.57		54.7				
2H-6, 125–126	16.45		6.48		54.0				
3H-1, 135–136	18.55		4.46		37.2				
3H-2, 92–93	19.62	5.68	5.58	0.10	46.5	0.04	0.12		
3H-2, 113–114	19.83	9.09	2.60	6.49	21.7	0.37	1.47	17.6	4.4
3H-2, 116–117	19.86	14.69	5.52	9.17	46.0	0.44	2.30	20.8	4.0
3H-3, 63–64	20.83	20.42	3.46	16.96	28.8	0.20	0.44	84.8	38.4
3H-3, 109–110	21.29	12.95	6.37	6.58	53.1	0.37	3.47	17.7	1.9
3H-3, 138–139	21.58		6.87		57.2				
3H-4, 47–48	22.17		7.81		65.1				
3H-4, 64–65	22.34	9.01	7.17	1.84	59.7	0.13	0.17	14.5	11.0
3H-5, 58–59	23.78	17.98	0.38	17.60	3.2	0.94	7.60	18.8	2.3
3H-5, 134–135	24.54		5.25		43.7				
3H-6, 86–87	25.56	8.79	5.93	2.86	49.4	0.22	2.00	13.1	1.4
3H-6, 100–101	25.70	7.96	5.50	2.46	45.8	0.17	2.02	14.2	1.2
3H-6, 128–129	25.98		4.70		39.2				
4H-1, 25–26	26.95	8.15	8.00	0.15	66.6	0.04	0.06		
4H-1, 36–37	27.06	15.98	3.35	12.63	27.9	0.66	5.29	19.1	2.4
4H-1, 44–45	27.14	7.04	6.83	0.21	56.9	0.04	0.71		
4H-1, 88–89	27.58		6.47		53.9				
4H-1, 114–115	27.84	13.27	4.51	8.76	37.6	0.50	4.34	17.5	2.0
4H-2, 114–115	29.34		8.72		72.6				
4H-3, 139–140	31.09		7.95		66.2				
4H-4, 83–84	32.03		7.50		62.5				
4H-4, 128–129	32.48	18.51	1.60	16.91	13.3	0.79	7.77	21.4	2.2
4H-5, 7–8	32.77	9.32	4.65	4.67	38.7	0.23	4.80	20.3	1.0
4H-5, 12–13	32.82	16.21	4.38	11.83	36.5	0.62	8.29	19.1	1.4
4H-5, 67–68	33.37		6.55		54.6				
4H-5, 135–136	34.05	12.09	5.77	6.32	48.1	0.34	2.32	18.6	2.7
4H-6, 143–144	35.63		7.73		64.4				
5H-1, 80–81	37.00		8.05		67.1				
5H-2, 58–59	38.28	10.17	6.64	3.53	55.3	0.20	2.32	17.7	1.5
5H-2, 129–130	38.99		8.46		70.5				
5H-3, 15–16	39.35	12.01	5.07	6.94	42.2	0.35	7.80	19.8	0.9
5H-3, 63–64	39.83	10.03	7.28	2.75	60.6	0.17	0.89	16.2	3.1
5H-3, 128–129	40.48		6.09		50.7				
5H-4, 21–22	40.91	12.65	4.32	8.33	36.0	0.42	2.79	19.8	3.0
5H-4, 108–109	41.78		7.43		61.9				
5H-5, 119–120	43.39		9.12		76.0				
5H-6, 128–129	44.98		9.13		76.1				
6H-1, 6–7		45.76		8.61		71.7			
6H-1, 107–109	46.77		8.48		70.6				
6H-1, 132–133	47.02	16.77	0.96	15.81	8.0	0.79	4.91	20.0	3.2
6H-2, 27–28	47.47	11.35	5.99	5.36	49.9	0.30	1.11	18.0	4.8
6H-2, 78–79	47.98	11.75	5.51	6.24	45.9	0.37	7.66	16.9	0.8
6H-2, 126–127	48.46		7.35		61.2				
6H-2, 140–141	48.60	12.47	6.05	6.42	50.4	0.36	8.18	17.8	0.8
6H-3, 44–45	49.14	10.71	6.36	4.35	53.0	0.26	6.30	16.8	0.7
6H-3, 70–71	49.40		7.29		60.7				
6H-3, 99–100	49.69	11.05	5.67	5.38	47.2	0.30	9.53	18.2	0.6
6H-4, 133–134	51.27		8.99		74.9				
6H-5, 48–49	51.92		7.86		65.5				
6H-5, 79–80	52.23	23.60	2.45	21.15	20.4	1.03	8.47	20.6	2.5
6H-5, 144–146	52.88		7.92		66.0				
6H-6, 8–10	53.02	17.46	5.07	12.39	42.2	0.61	6.86	20.3	1.8
6H-6, 21–23	53.15		8.30		69.1				
6H-6, 68–69	53.62		9.11		75.9				
6H-6, 81–82	53.75		7.78		64.8				
6H-6, 99–100	53.93	15.05	2.48	12.57	20.7	0.64	10.40	19.5	1.2
6H-6, 145–146	54.39	28.87	0.33	28.54	2.7	1.34	11.65	21.4	2.4
6H-7, 40–41	54.84	22.49	1.61	20.88	13.4	0.98	12.32	21.4	1.7
6H-7, 61–62	55.05		7.29		60.7				
6H-CC, 7–10	55.34	20.14	1.00	19.14	8.3	0.92	9.86	20.8	1.9
7H-1, 18–19	55.38	22.85	2.26	20.59	18.8	0.91	9.00	22.5	2.3
7H-1, 60–61	55.80	30.97	0.43	30.54	3.6	1.33		22.9	
7H-1, 84–85	56.04	6.34	6.32	0.02	52.6	0.04	2.55		
7H-1, 100–102	56.20	22.18	3.72	18.46	31.0	0.90	8.89	20.6	2.1
7H-1, 111–113	56.31	8.30	8.30	0.00	69.1	0.03	0.58		

Table 11 (continued).

Core, section, interval (cm)	Depth (mbsf)	Total carbon (%)	Inorganic carbon (%)	Organic carbon (%)	$CaCO_3$ (%)	Nitrogen (%)	Sulfur (%)	C_{org}/N	C_{org}/S
7H-1, 130–133	56.50		7.47		62.2				
7H-2, 84–85	57.54	19.32	1.10	18.22	9.2	0.91	13.18	20.0	1.4
7H-2, 131–132	58.01		7.74		64.5				
7H-3, 136–137	59.56		8.18		68.1				
7H-4, 124–125	60.94		7.65		63.7				
7H-5, 127–128	62.47		7.18		59.8				
7H-6, 116–117	63.86		7.72		64.3				
8H-1, 71–72	65.41		8.81		73.4				
8H-2, 71–72	66.91	8.30	8.30	0.00	69.1	0.03	0.15		
8H-3, 72–73	68.42		8.28		69.0				
8H-4, 72–73	69.92		7.31		60.9				
8H-6, 73–74	72.93		6.90		57.5				
8H-6, 108–109	73.28	8.32	8.18	0.14	68.1	0.03	0.10		
8H-7, 43–45	74.13	7.17	7.14	0.03	59.5	0.06	0.00		
9H-1, 96–97	75.16		7.77		64.7				
9H-2, 100–101	76.70		6.73		56.1				
9H-3, 74–75	77.94		7.27		60.6				
9H-4, 63–64	79.33		7.03		58.6				
9H-5, 103–104	81.23		7.12		59.3				
9H-6, 65–66	82.35	8.52	8.52	0.00	71.0	0.03	0.05		
9H-6, 72–73	82.42	11.39	6.77	4.62	56.4	0.32	0.21	14.3	21.8
9H-6, 80–81	82.50	9.12	9.12	0.00	76.0	0.04	0.10		
9H-6, 90–91	82.60		8.03		66.9				
10H-1, 79–80	84.49		8.26		68.8				
10H-2, 66–67	85.86		7.82		65.1				
10H-2, 90–91	86.10	12.71	7.64	5.07	63.6	0.35	0.99	14.4	5.1
10H-2, 115–116	86.35		7.67		63.9				
10H-3, 18–19	86.88	11.49	8.73	2.76	72.7	0.22	0.22	12.5	12.5
10H-3, 78–79	87.48		8.22		68.5				
10H-4, 58–59	88.78		9.07		75.6				
10H-4, 71–72	88.91	10.98	8.72	2.26	72.6	0.18	0.19	12.5	11.9
10H-5, 86–87	90.56		9.65		80.4				
10H-6, 109–110	92.29		9.55		79.6				
11H-1, 48–49	93.68		8.10		67.5				
11H-1, 56–57	93.76	11.75	7.75	4.00	64.6	0.30	1.07	13.3	3.7
11H-1, 125–126	94.45	11.22	7.97	3.25	66.4	0.25	1.12	13.0	2.9
11H-2, 27–28	94.97		8.62		71.8				
11H-2, 43–44	95.13	11.57	8.15	3.42	67.9	0.26	0.72	13.1	4.8
11H-2, 64–65	95.34	8.45	8.45	0.00	70.4	0.03	0.11		
11H-2, 110–111	95.80	10.40	8.15	2.25	67.9	0.21	0.24	10.7	9.3
11H-3, 101–102	97.21		8.02		66.8				
11H-3, 122–123	97.42	11.46	6.38	5.08	53.1	0.37	0.94	13.8	5.4
11H-3, 130–131	97.50	10.32	8.02	2.30	66.8	0.18	5.62	12.8	0.4
11H-4, 45–46	98.15		7.88		65.6				
11H-5, 75–76	99.95		8.96		74.6				
12H-2, 35–36	103.30		2.77		23.1				
13H-1, 96–97	106.46	4.28	4.24	0.04	35.3	0.04	0.84		

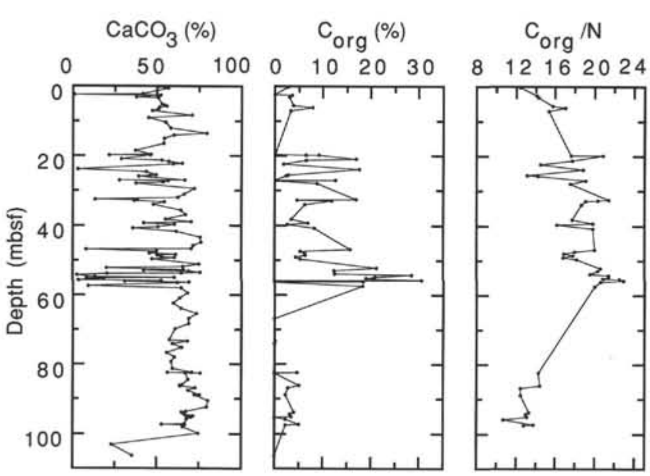

Figure 44. Downhole distribution of calcium carbonate and organic carbon concentrations and the ratio of organic carbon to total nitrogen in sediments from Hole 969A.

ysis yielded neither hydrocarbon-type material (HI = 22) nor carbon dioxide (OI = 3) above trace levels, and there was virtually no extractable organic matter.

Organic Matter Type: C_{org}/N Ratios and Rock-Eval Pyrolysis

C_{org}/N ratios for all sapropels, with only one exception, exceed a value of 12; they have an average of 17 and a maximum of 22.9, disregarding the "charcoal" sample (Table 11, Fig. 44). As already observed for sapropels at previous sites (see "Organic Geochemistry" section, chapters for Site 964 and 966–968, this volume), the surprisingly high values of the C_{org}/N ratios suggest a predominance of terrestrial organic matter that is not in accordance with the indications provided by the Rock-Eval parameters. As at the other sites, the high C_{org}/N ratios in the sapropels are tentatively interpreted as representing an effective removal of nitrogen compounds from the marine organic matter during diagenesis. However, the possibility that the primary marine organic matter was already poor in nitrogen-bearing constituents cannot be excluded.

Results of Rock-Eval pyrolysis (Table 12) show that hydrogen indices for many samples exceed 300, with a maximum value slightly above 457 measured in Section 160-969A-7H-1. The hydrogen index values indicate partial oxidation of the primary marine organic matter and/or an admixture of terrigenous organic matter. Consistent with the relationship between organic matter type and elemental composi-

Table 12. Results of Rock-Eval analysis for Hole 969A.

Core, section, interval (cm)	Depth (mbsf)	S_1 (mg/g)	S_2 (mg/g)	S_3 (mg/g)	TOC (%)	PC	HI	OI	T_{max} (°C)	PI	S_2/S_3
160-969A-											
1H-1, 29–30	0.29	0.47	4.58	3.75	2.86	0.42	160	131	419	0.09	1.22
1H-2, 112–113	2.62	0.98	8.34	4.22	3.64	0.77	229	116	418	0.11	1.98
1H-3, 24–25	3.24	0.38	5.68	3.93	3.09	0.50	184	127	419	0.06	1.45
1H-4, 103–104	5.53	0.75	10.10	4.05	3.93	0.90	257	103	418	0.07	2.49
1H-5, 17–18	6.17	3.58	26.37	5.62	7.82	2.49	337	72	420	0.12	4.69
1H-5, 112–113	7.12	0.60	8.49	3.50	3.40	0.75	250	103	423	0.07	2.43
3H-2, 113–114	19.83	1.17	22.23	3.90	6.49	1.94	343	60	421	0.05	5.70
3H-2, 116–117	19.86	3.44	34.90	5.02	9.17	3.18	381	55	420	0.09	6.95
3H-3, 63–64	20.83	0.74	3.71	0.47	16.96	0.37	22	3	357	0.17	7.89
3H-3, 109–110	21.29	2.12	19.06	4.41	6.58	1.76	290	67	419	0.10	4.32
3H-4, 64–65	22.34	0.19	3.45	2.41	1.84	0.30	188	131	421	0.05	1.43
3H-5, 58–59	23.78	5.25	50.81	6.95	17.60	4.65	289	39	424	0.09	7.31
3H-6, 86–87	25.56	0.28	5.07	2.72	2.86	0.44	177	95	421	0.05	1.86
3H-6, 100–101	25.70	0.23	5.59	2.56	2.46	0.48	227	104	419	0.04	2.18
4H-1, 36–37	27.06	3.45	38.89	6.13	12.63	3.51	308	49	418	0.08	6.34
4H-1, 114–115	27.84	2.53	27.05	4.98	8.76	2.46	309	57	417	0.09	5.43
4H-4, 128–129	32.48	6.66	65.48	6.36	16.91	5.99	387	38	413	0.09	10.30
4H-5, 7–8	32.77	2.03	14.37	4.62	4.67	1.36	308	99	418	0.12	3.11
4H-5, 12–13	32.82	9.44	38.00	8.89	11.83	3.94	321	75	412	0.20	4.27
4H-5, 135–136	34.05	2.98	24.31	5.51	6.32	2.27	385	87	422	0.11	4.41
5H-2, 58–59	38.28	1.02	8.54	4.42	3.53	0.79	242	125	424	0.11	1.93
5H-3, 15–16	39.35	4.28	27.18	5.78	6.94	2.61	392	83	422	0.14	4.70
5H-3, 63–64	39.83	0.67	7.77	3.54	2.75	0.70	283	129	428	0.08	2.19
5H-4, 21–22	40.91	4.24	29.97	6.48	8.33	2.84	360	78	420	0.12	4.63
6H-1, 132–133	47.02	10.86	50.69	9.86	15.81	5.11	321	62	414	0.18	5.14
6H-2, 27–28	47.47	1.91	15.89	5.28	5.36	1.48	296	99	419	0.11	3.01
6H-2, 78–79	47.98	2.41	14.82	6.10	6.24	1.43	238	98	414	0.14	2.43
6H-2, 140–141	48.60	3.62	15.08	5.52	6.42	1.55	235	86	409	0.19	2.73
6H-3, 44–45	49.14	1.43	10.95	4.60	4.35	1.03	252	106	420	0.12	2.38
6H-3, 99–100	49.69	3.35	16.53	5.38	5.38	1.65	307	100	415	0.17	3.07
6H-5, 79–80	52.23	12.90	75.32	12.94	21.15	7.32	356	61	424	0.15	5.82
6H-6, 8–10	53.02	9.56	46.98	9.04	12.39	4.69	379	73	417	0.17	5.20
6H-6, 99–100	53.93	8.44	43.18	9.28	12.57	4.28	344	74	417	0.16	4.65
6H-6, 145–146	54.39	23.84	86.04	15.58	28.54	9.12	301	55	410	0.22	5.52
6H-7, 40–41	54.84	16.53	89.71	9.75	20.88	8.82	430	47	415	0.16	9.20
6H-CC, 7–10	55.34	14.98	83.60	8.12	19.14	8.18	437	42	419	0.15	10.30
7H-1, 18–19	55.38	24.98	93.42	8.81	20.59	9.83	454	43	411	0.21	10.60
7H-1, 60–61	55.80	23.30	108.45	15.33	30.54	10.94	355	50	419	0.18	7.07
7H-1, 100–102	56.20	18.53	84.45	8.83	18.46	8.55	457	48	414	0.18	9.56
7H-2, 84–85	57.54	16.92	77.93	7.94	18.22	7.87	428	44	412	0.18	9.81
9H-6, 72–73	82.42	1.54	18.34	3.87	4.62	1.65	397	84	418	0.08	4.74
10H-2, 90–91	86.10	1.77	17.38	3.61	5.07	1.59	343	71	414	0.09	4.81
10H-3, 18–19	86.88	1.11	8.70	2.97	2.76	0.81	315	108	415	0.11	2.93
11H-1, 56–57	93.76	1.34	12.36	3.50	4.00	1.14	309	88	405	0.10	3.53
11H-1, 125–126	94.45	0.74	9.25	2.81	3.25	0.83	285	86	416	0.07	3.29
11H-2, 43–44	95.13	1.34	11.61	2.99	3.42	1.07	339	87	411	0.10	3.88
11H-3, 122–123	97.42	1.27	16.21	3.49	5.08	1.45	319	69	421	0.07	4.64

Notes: TOC = total organic carbon; PC = petroleum potential as pyrolyzable carbon; HI = hydrogen index; OI = oxygen index; PI = production index; see the "Explanatory Notes" chapter (this volume) for units for these parameters.

tion, the oxygen indices show an opposite trend to the hydrogen indices. The general tendency for higher hydrogen indices with increasing content of organic matter does not hold for the extremely organic-matter-rich sapropels (Fig. 45).

Sulfur

Sulfur contents are reported in Table 11. They are generally high in all sapropels, but those between about 47 and 58 mbsf are particularly enriched. Here, values range from 5% to 12%, and the maximum of 13.2% was found in Sample 160-969A-7H-2, 84–85 cm. Most of the sulfur is present as pyrite, because pyrite concretions were visually detected in the sapropels and abundant disseminated pyrite was observed under the microscope. The downhole profile of sulfur roughly parallels that of organic carbon (Fig. 46).

Extractable Bitumen: Assessment of Paleotemperatures

Forty-eight sapropel samples were analyzed for long-chain alkenones following the procedure described in the "Explanatory Notes" chapter (this volume).

As shown in Figure 47, sea-surface temperatures were generally variable during the Pleistocene (above about 30 mbsf); they show a

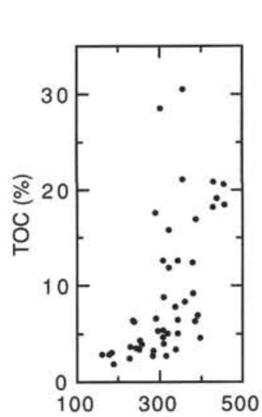

Figure 45. Relationship between total organic carbon and hydrogen index for sediments from Hole 969A.

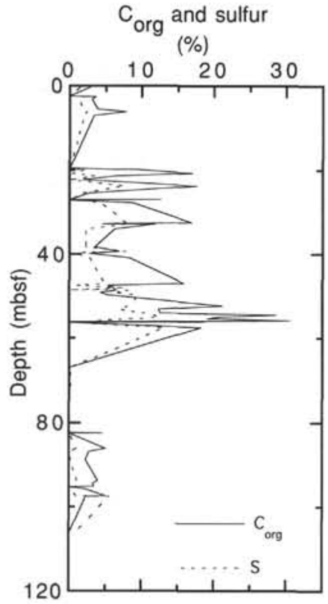

Figure 46. Downhole variation of organic carbon and total sulfur contents in sediments from Hole 969A.

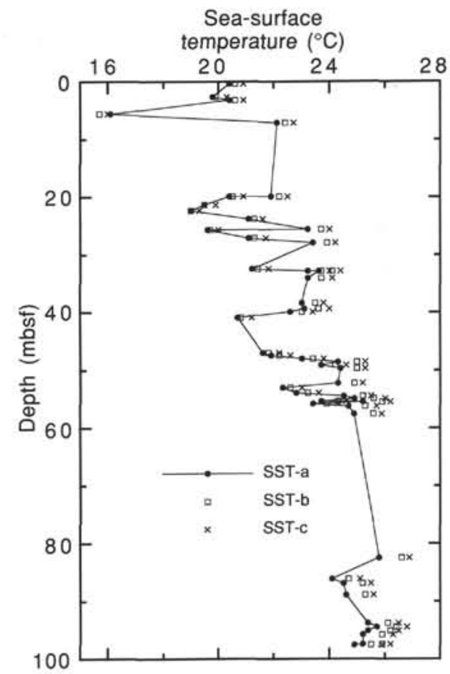

Figure 47. Variation of paleo-sea-surface temperatures (SST) during times of sapropel deposition as a function of depth in Hole 969A. Temperatures were calculated from the alkenone unsaturation index ($U^{k'}_{37}$ according to the calibrations of (a) Sikes and Volkman (1993), (b) Prahl and Wakeham (1987), and (c) Brassell (1993).

range of approximately 7°C between 16° and 23°C regardless of the calibration used. In the Pliocene (below 30 mbsf), temperatures were higher and less variable. This trend was already observed at previous sites (see "Organic Geochemistry" section, "Site 964," "Site 966," and "Site 967" chapters, this volume). Nevertheless, the estimated Pliocene temperatures at Site 969 are slightly lower than those found in the eastern part of the basin (see "Organic Geochemistry" section, "Site 966" and "Site 967" chapters, this volume).

The alkenone sea-surface temperature pattern is in general accordance with the results of previous geochemical studies on Mediterranean sapropels (ten Haven, 1986; ten Haven et al., 1987; K.C. Emeis, pers. comm., 1995) and the current understanding of climate development during the past few million years.

PHYSICAL PROPERTIES

A complete suite of physical properties (see "Explanatory Notes" chapter, this volume) was measured in all cores from Hole 969A, and MST measurements were gathered in cores from Holes 969A through 969F. In this section, we describe the downhole distribution of physical properties in Hole 969A.

Index Properties

Bulk and dry densities were measured in every section of unconsolidated sediment down to 108 mbsf. In addition, index properties samples were taken from selected sapropels and from 5–10 cm above and below these sapropels. Density generally increases with depth (Table 13, Fig. 48). Sapropels show low values of bulk density and high values of porosity and water content (Fig. 48).

Discrete-sample *P*-wave and Shear Strength Measurements

Horizontal and vertical *P*-wave velocities measured with the digital sonic velocimeter show a generally increasing trend with depth in Hole 969A (Table 14, Fig. 49). Owing to an increase in rock strength, the measurement method was switched from DSV 1 to DSV 3 at 39 mbsf. The DSV 3 measurements show a large scatter. A comparison of DSV 1 and DSV 3 water velocities shows that the DSV 3 values are about 300 m/s higher, although the calibration measurements on aluminum blocks agree very well. Therefore, velocities determined with DSV 3 should be considered suspect. However, measurements of vane-shear strength also show considerable scatter in the section below 45 mbsf (Table 15, Fig. 49) besides a general increase with depth from less than 20 kPa to up to 300 kPa.

GRAPE Density

The overall trend of the GRAPE data (Fig. 50) is toward slightly increasing density with depth, and the rate of the density increase is low but constant. Low GRAPE-density values correlate with the index properties densities of the sampled sapropels but can also reflect the effects of undrained core samples. Most measurements are scattered between 1.3 and 1.7 g/cm^3, but the section at 60–80 mbsf shows markedly reduced scatter from 1.55 to 1.7 g/cm^3. A comparison of index properties density measurements with GRAPE density (Fig. 50) suggests that the GRAPE measurements in this hole underestimate density, despite application of the Boyce correction (see "Explanatory Notes" chapter, this volume, and as discussed in the "Physical Properties" section, "Site 967" chapter, this volume).

Compressional Wave Velocities

High-resolution compressional wave velocities were measured using the PWL of the MST (Fig. 51). The gradient changes with depth in three steps, with a large decrease of compressional wave velocity values in the upper 20 m and lower gradients between 20 and 45 mbsf and between 55 and 65 mbsf.

Magnetic Susceptibility

Figure 52 shows the results of magnetic susceptibility measurements from Hole 969A. Two large sections, one from 0 to 50 mbsf

Table 13. Index properties measured in APC cores from Hole 969A.

Core, section, interval (cm)	Depth (mbsf)	Water content (wt%)	Porosity (vol%)	Bulk density (g/cm^3)		Grain density (g/cm^3)		Dry density (g/cm^3)	
				Method B	Method C	Method B	Method C	Method B	Method C
160-969A-									
1H-1, 69–71	0.69	38.37	63.54	1.70	1.66	2.87	2.70	1.05	1.02
1H-2, 68–70	2.18	41.55	67.50	1.66	1.61	2.99	2.72	0.97	0.94
1H-3, 39–41	3.39	38.70	64.14	1.70	1.66	2.90	2.71	1.04	1.02
1H-4, 75–77	5.25	41.61	66.78	1.64	1.62	2.89	2.75	0.96	0.94
1H-4, 102–104	5.52	54.66	77.23	1.45	1.41	2.88	2.61	0.66	0.64
1H-4, 128–130	5.78	41.90	66.67	1.63	1.61	2.84	2.74	0.95	0.94
1H-5, 75–77	6.75	40.37	64.34	1.63	1.62	2.73	2.66	0.97	0.96
2H-1, 137–139	9.07	33.99	60.17	1.81	1.75	3.01	2.75	1.20	1.15
2H-2, 120–122	10.40	34.08	58.27	1.75	1.73	2.77	2.70	1.15	1.14
2H-3, 134–136	12.04	33.05	58.13	1.80	1.76	2.88	2.71	1.21	1.18

Only part of this table is reproduced here. The entire table appears on the CD-ROM (back pocket).

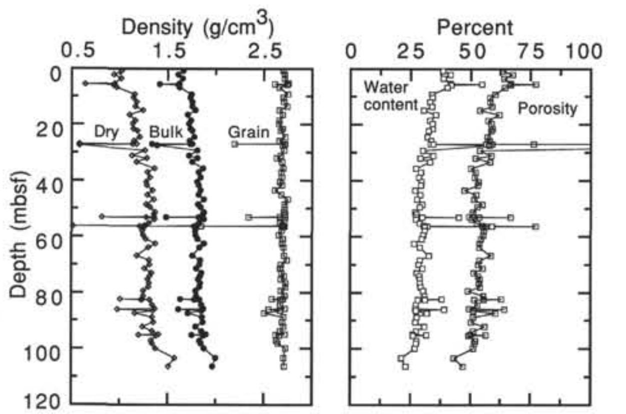

Figure 48. Index properties measured in cores from Hole 969A. Density calculations were made using method C (see "Explanatory Notes" chapter, this volume).

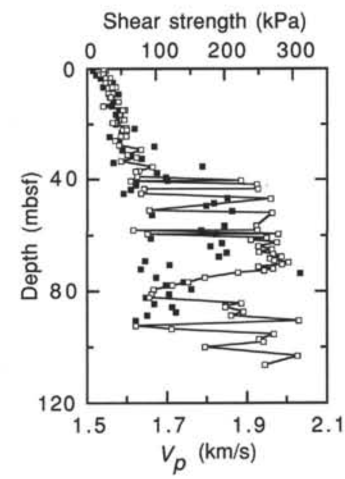

Figure 49. *P*-wave velocity and vane shear strength measured in cores from Hole 969A; DSV 1 (vertical) V_p = connected open squares; vane shear strength = solid squares.

Table 14. Compressional wave velocity measured in split APC cores from Hole 969A.

Core, section, interval (cm)	Depth (mbsf)	Measurement type	Velocity (km/s)
160-969A-			
1H-1, 74.7	0.75	DSV 1	1.55
1H-1, 75.5	0.76	DSV 2	1.54
1H-2, 71.6	2.22	DSV 1	1.53
1H-2, 73.1	2.23	DSV 2	1.54
1H-3, 39.0	3.39	DSV 1	1.56
1H-3, 40.9	3.41	DSV 2	1.55
1H-4, 69.2	5.19	DSV 1	1.55
1H-4, 70.0	5.20	DSV 2	1.55
1H-5, 76.9	6.77	DSV 2	1.57
1H-5, 77.6	6.78	DSV 1	1.56

Note: Direct DSV measurements.

Only part of this table is reproduced here. The entire table appears on the CD-ROM (back pocket).

Table 15. Vane shear strength measured in split APC cores from Hole 969A.

Core, section, interval (cm)	Depth (mbsf)	Strength (kPa)
160-969A-		
1H-1, 84.1	0.84	8.17
1H-2, 77.5	2.28	13.31
1H-3, 43.5	3.44	19.70
1H-4, 75	5.25	37.73
1H-5, 69.7	6.70	23.16
2H-1, 145.2	9.15	46.01
2H-2, 111.2	10.31	35.63
2H-3, 143.9	12.14	38.25
2H-4, 140.7	13.61	36.58
2H-5, 121.1	14.91	46.74

Only part of this table is reproduced here. The entire table appears on the CD-ROM (back pocket).

and another between 60 and 100 mbsf, show relatively high and constant values. They are bordered by smaller sections between 50 and 60 mbsf and between 100 and 106 mbsf with lower susceptibility. Below 106 mbsf, values increase again. On a finer scale, considerable variation can be observed.

Natural Gamma-ray Radiation

NGR values measured using the MST from Hole 969A show several first-order trends (Fig. 53). NGR values are generally about 20 counts per second (cps) with anomalously high values between 45 and 55 mbsf and below 103 mbsf. These large-scale variations correlate (R = 0.81) to the amount of organic carbon in the sediments. A section of low NGR values is at 60–80 mbsf. Superimposed on these first-order trends are many centimeter- to decimeter-scale variations.

Thermal Conductivity

Thermal conductivity at Hole 969A was sampled once per section in all cores from Hole 969A (Table 16, Fig. 54). Thermal conductiv-

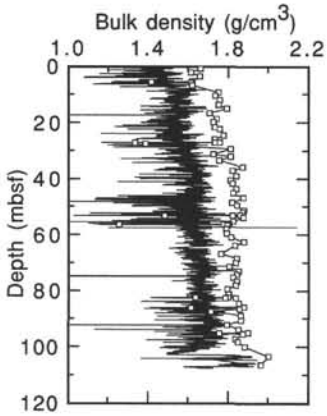

Figure 50. Density measured as part of index properties measurements (connected open symbols) and GRAPE density (line) measured using the MST.

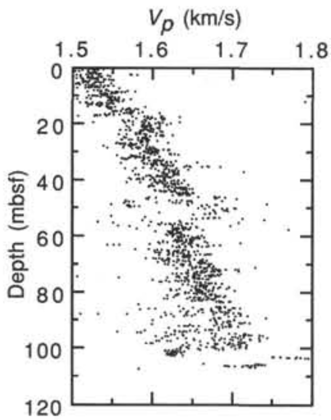

Figure 51. *P*-wave velocities measured in cores from Hole 969A using the PWL component of the MST.

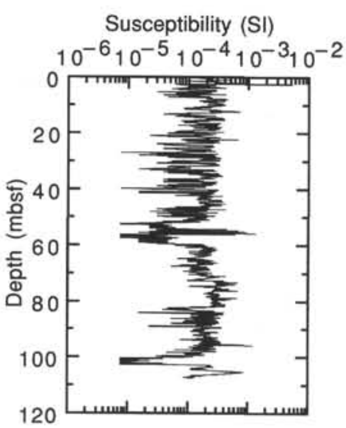

Figure 52. Magnetic susceptibility measured with the MST in cores from Hole 969A.

ity values increase with depth from 1.2 to 1.6 W/(m · K) owing to a reduction in porosity.

HEAT-FLOW MEASUREMENTS

In situ formation temperatures were measured with the ADARA system at Cores 160-969A-5H, 7H, and 9H (Table 17, Fig. 55). All

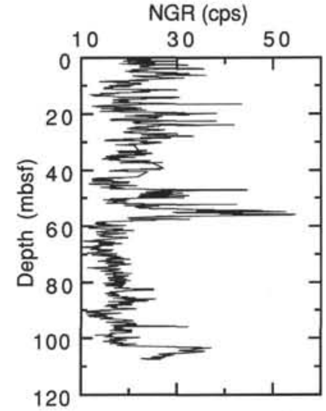

Figure 53. Natural gamma-ray radiation measured in cores from Hole 969A.

Table 16. Thermal conductivity measured in APC cores from Hole 969A.

Core, section, interval (cm)	Depth (mbsf)	Thermal conductivity (W/[m · K])
160-969A-		
1H-1, 50	0.50	1.244
1H-2, 50	2.00	1.098
1H-3, 50	3.50	1.301
1H-4, 50	5.00	1.258
1H-5, 50	6.50	1.184
2H-1, 50	8.20	1.222
2H-2, 50	9.70	1.242
2H-3, 50	11.20	1.397
2H-4, 50	12.70	1.421
2H-5, 50	14.20	1.229

Only part of this table is reproduced here. The entire table appears on the CD-ROM (back pocket).

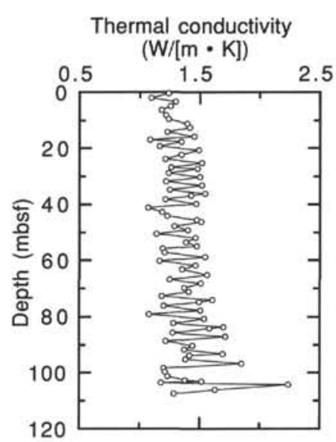

Figure 54. Thermal conductivity measured in cores from Hole 969A.

time-temperature series are of high quality and no obvious disturbance was observed during the temperature measurements. However, the temperature at 45.5 mbsf (Core 160-969A-5H) seems unreasonably low compared to the observed mud-line temperature, which is confirmed by three independent measurements. The ADARA temperature of 11.04°C at 45.5 mbsf would result in unrealistic temperature gradients and heat-flow values. If the low value at 45.5 mbsf is neglected, the average temperature gradient is 8.0 K/km. Together with thermal conductivity values from the core measurements (see

Table 17. In situ formation temperature measurements made with the ADARA at Hole 969A.

Core	Depth (mbsf)	Temperature (°C)
160-969A-		
Mud line	0.0	14.14
5H	45.5	11.04
7H	65.0	14.74
9H	83.5	14.78

"Physical Properties" section, this chapter), the heat flow in the upper 100 mbsf is 14 mW/m^2. Similar low values were observed at previous Leg 160 sites (see "Heat-flow Measurements" section, "Site 968" chapter, this volume). Owing to the lack of available temperature data and the failure of the TLT, it is not possible to explain the low value at 45.5 mbsf.

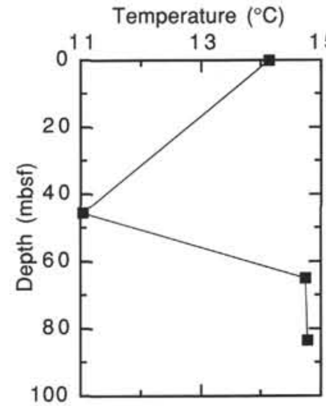

Figure 55. Results of ADARA measurements in Hole 969A.

SUMMARY AND CONCLUSIONS

Site 969 (33°50.40′N, 24°53.06′E, in 2200 m of water) is located on the Mediterranean Ridge in an area of limited tectonic deformation near the Inner Deformation Front. In the vicinity of the site, an upper sedimentary unit approximately 120 m (130 ms TWT) thick overlies a strong seismic reflector inferred to be the Messinian. Based on piston-core and seismic information, the location was chosen to recover a complete Pliocene to Pleistocene sedimentary record from the sill separating the Levantine Basin in the east from the Ionian Basin in the west.

Our specific objectives at Site 969 were (1) to recover complete sedimentary sequences that record the conditions of sapropel formation in an intermediate water depth interval from the lowermost Pliocene to the Holocene and (2) to recover the transition interval from the uppermost Miocene to the lower Pliocene.

Six holes were cored at Site 969 to a maximum depth of 116 mbsf. Recovery and core quality in the APC cores were excellent (average recovery 102%) and a sediment section was recovered that spans the uppermost Miocene(?)/lowermost Pliocene to the Holocene. The sedimentary sequence consists of nannofossil ooze and nannofossil clay with sapropels of early Pliocene to Holocene age (Unit I) that unconformably overlie calcareous silty clay of indeterminate age (Unit II), of which a total of 5.45 m was recovered. Holes 969A, 969B, and 969C contain locally faulted and thinned sedimentary sequences. However, sedimentological markers and physical properties in these holes could unambiguously be correlated. Hole 969D appears to be expanded, perhaps because the beds are tilted, and appears to have yielded a more complete sedimentary sequence in the upper Pliocene to lower Pleistocene.

More than 80 sapropels were recovered from the lower Pliocene through Holocene section at Site 969. These occur in five distinct groups separated by intervals of sediment that are commonly oxidized and are yellowish brown in color with no preserved sapropels. The lowermost sapropel occurs near the transition of Units I and II, presumably in the lowermost Pliocene. The darkest black sapropels have a fine, bedding-parallel parting, which may be the result of a primary lamination. Their organic carbon content reaches up to 30%. Based on the amount of hydrocarbons liberated by pyrolysis, the organic matter is interpreted to be degraded marine material with admixtures of terrigenous origin. One sapropel appears to be composed of a charcoal-like material. The organic matter has unusually high C_{org}/N ratios and high organic carbon concentrations that are associated with high sulfur concentrations of up to 12 wt%. Preliminary assessment of paleo-sea-surface temperatures suggests that the surface mixed layer was significantly warmer during the Pliocene as compared to the Pleistocene.

The sapropels clearly stand out in a number of continuously logged physical properties; their density is lower (1.4 g/cm^3) than that of carbonate oozes, their water content is higher, and their natural gamma-ray emission is distinctly higher and correlates with organic carbon concentrations.

Stratigraphic control for the sediment sequence was achieved using calcareous nannofossils and planktonic foraminifers; siliceous microfossils were not found. The 18 biostratigraphic events recognized in Hole 969A range from the earliest Pliocene (MPL1) to the late Pleistocene. The clay-rich unit at the base of the recovered sequence contained no age-diagnostic taxa and yielded only reworked marine specimens and ostracodes indicative of brackish waters. The age vs. depth relationship reveals that the sedimentation rate in Hole 969A averaged 22 m/m.y. since the early Pliocene and varied between 6 and 86 m/m.y. In Hole 969D, rates of up to 60 m/m.y. that were calculated for the middle Pliocene are clearly related to tectonic thickening of the interval.

Several polarity zones were recognized by measuring discrete samples, and these zones compare well with the biostratigraphic data. The magnetic intensity was found to be much higher in the sapropels than in the surrounding sediment. A significant increase in intensity appears to be a general feature of sapropels and may be related to postdepositional magnetic enhancement by mineral formation during diagenesis.

Pore-water concentrations of dissolved ions imply that solutions characteristic of late-stage brine, possibly derived from dissolving evaporites at depth, are present below the penetration depth of the cored sediment intervals. The ratios of ammonium and alkalinity show that some carbonate diagenesis occurs in the sediment.

The setting of the site on the Mediterranean Ridge imparted structural elements of both extension and compression to the sediments. In most holes drilled at Site 969, bedding is horizontal to subhorizontal and bedding planes as well as normal faults show no preferred orientation. In Hole 969D, the section is tilted and reverse faults occur in closely packed structures with the preferred orientation of the faults to the southwest. In the sequence, bedding was found to increase to an inclination of 30° in Core 160-969D-5H, which in part accounts for the increased thickness of the middle Pliocene sedimentary sequence in this hole.

As was expected, Site 969 yielded a sedimentary sequence that most likely includes the uppermost Messinian, a well-developed basal Pliocene, and a Pliocene to Holocene section with abundant and extraordinarily organic-rich sapropels. Tectonic overprinting resulted in considerable variation between holes that are within a few hundred meters' distance. Detailed post-cruise interhole correlation is needed to establish if the sequence is complete and to address higher resolution paleoceanographic issues.

REFERENCES

Belderson, R.H., Kenyon, N.H., Stride, A.H., and Stubbs, A.H., 1972. 10-km wide views of the Mediterranean deep sea floor. *Deep-Sea Res.,* 17:267–270.

Benson, R.H., 1978. The paleoecology of the ostracodes of DSDP Leg 42A. *In* Hsü K.J., Montadert, L., et al., *Init. Repts. DSDP,* 42 (Pt. 1): Washington (U.S. Govt. Printing Office), 777–787.

Brassell, S.C., 1993. Applications of biomarkers for delineating marine paleoclimatic fluctuations during the Pleistocene. *In* Engel, M.H., and Macko, S.A. (Eds.), *Organic Geochemistry: Principles and Applications:* New York (Plenum), 699–738.

Cita, M.B., 1975. Planktonic foraminiferal biozonation of the Mediterranean Pliocene deep-sea record: a revision. *Riv. Ital. Paleontol. Stratigr.,* 81:527–544.

Cita, M.B., and Camerlenghi, A., 1990. The Mediterranean Ridge as an accretionary prism in collision context. *Mem. Soc. Geol. Ital.,* 45:463–480.

Cita, M.B., Fornaciari, M., Camerlenghi, A., Corselli, C., Erba, E., McCoy, F., and Vezzoli, L., 1986. Anoxic basins of the Eastern Mediterranean: new evidence from the Bacino Bannock area. *Mem. Soc. Geol. Ital.,* 36:131–144.

Cita, M.B., and Limonov, A., 1993. Olimpi mud volcano area (study area 3). 3.1. Geological setting. *In* Limonov, A.F., Woodside, J.M., and Ivanov, M.K. (Eds.), *Mud Volcanism in the Mediterranean and Black Seas and Shallow Structure of the Eratosthenes Seamount.* UNESCO Rep. Mar. Sci., 64:58–65.

Dewey, J.F., Pitman, W.C., Ryan, W.B.F., and Bonin, J., 1973. Plate tectonics and the evolution of the Alpine system. *Geol. Soc. Am. Bull.,* 84:3137–3180.

Finetti, I., 1982. Structure, stratigraphy and evolution of central Mediterranean. *Boll. Geofis. Teor. Appl.,* 24:247–315.

Giermann, G., 1969. The Eastern Mediterranean Ridge. *Rapp. Comm. Int. Mer Medit.,* 19:605–607.

Gieskes, J.M., 1981. Deep-sea drilling interstitial water studies: implications for chemical alteration of the oceanic crust, layers I and II. *In* Warme, J.E., Douglas, R.G., and Winterer, E.L. (Eds.), *The Deep Sea Drilling Project: A Decade of Progress.* Spec. Publ.—Soc. Econ. Paleontol. Mineral., 32:149–167.

————, 1983. Interstitial waters of deep sea sediments. *In* Chester, J.P., and Riley, R. (Eds.), *Chemical Oceanography* (Vol. 6): New York (Academic), 221–269.

Hasegawa, S., Sprovieri, R., and Poluzzi, A., 1990. Quantitative analysis of benthic foraminiferal assemblages from Plio-Pleistocene sequences in the Tyrrhenian Sea, ODP Leg 107. *In* Kastens, K.A., Mascle, J., et al., *Proc. ODP, Sci. Results,* 107: College Station, TX (Ocean Drilling Program), 461–478.

Hersey, J.B., 1965. Sedimentary basins of the Mediterranean Sea. *Proc. Symp. Colston Res. Soc.,* 17:75–91.

Hsü, K.J., Montadert, L., et al., 1978. *Init. Repts. DSDP,* 42 (Pt. 1): Washington (U.S. Govt. Printing Office).

Hsü, K.J., and Ryan, W.B.F., 1973. Summary of the evidence for extensional and compressional tectonics in the Mediterranean. *In* Ryan, W.B.F., Hsü, K.J., et al., *Init. Repts. DSDP,* 13 (Pt 2): Washington (U.S. Govt. Printing Office), 1011–1019.

Kastens, K., 1991. Rate of outward growth of the Mediterranean Ridge. *Tectonophysics,* 109:25–50.

Kastens, K.A., Breen, N.A., and Cita, M.B., 1992. Progressive deformation on an evaporite-bearing accretionary complex: SeaMARC 1, SeaBeam, and piston-core observations from the Mediterranean Ridge. *Mar. Geophys. Res.,* 14:249–298.

Le Pichon, X., 1982. Land-locked oceanic basins and continental collision: the Eastern Mediterranean as a case example. *In* Hsü, K.J. (Ed.), *Mountain Building Processes:* New York (Academic), 201–211.

Limonov, A.F., Woodside, J.M., and Ivanov, M.K. (Eds.), 1994. *Mud Volcanism in the Mediterranean and Black Seas and Shallow Structure of the Eratosthenes Seamount.* UNESCO Rep. Mar. Sci., 64.

Manheim, F.T., and Sayles, F.L., 1974. Composition and origin of interstitial water of marine sediments based on deep sea drilled cores. *In* Goldberg, E.D. (Ed.), *The Sea* (Vol. 5): New York (Wiley Interscience), 527–568.

Prahl, F.G., and Wakeham, S.G., 1987. Calibration of unsaturation patterns in long-chain ketone composition for paleotemperature assessment. *Nature,* 330:367–369.

Ryan, W.B.F., Kastens, K.A., and Cita, M.B., 1982. Geological evidence concerning compressional tectonics in the Eastern Mediterranean. *Tectonophysics,* 86:213–242.

Sikes, E.L., and Volkman, J.K., 1993. Calibration of alkenone unsaturation ratios ($U_{37}^{k'}$) for paleotemperature estimation in cold polar waters. *Geochim. Cosmochim. Acta,* 57:1883–1889.

Spaak, P., 1982. Accuracy in correlation and ecological aspects of the planktonic foraminiferal zonation of the Mediterranean Pliocene [Ph.D. dissert.]. Univ. Utrecht, The Netherlands.

Spiegler, D., and Rögl, F., 1992. Bolboforma (Protophyta, incertae sedis) im Oligozän und Miozän des Mediterran und der Zentralen Paratethys. *Ann. Naturhist. Mus. Wien,* 94:59–95.

Sprovieri, R., 1993. Pliocene–early Pleistocene astronomically forced planktonic Foraminifera abundance fluctuations and chronology of Mediterranean calcareous plankton bio-events. *Riv. Ital. Paleontol. Stratigr.,* 99:371–414.

Stride, A.H., Belderson, R.H., and Kenyon, N.H., 1977. Evolving miogeanticlines of the East Mediterranean (Hellenic, Calabrian and Cyprus Outer Ridges). *Phil. Trans. R. Soc. London A,* 284:255–258.

ten Haven, L., 1986. Organic and inorganic aspects of Mediterranean late Quaternary sapropels and Messinian evaporitic deposits [Ph.D. thesis]. Univ. Utrecht, The Netherlands. *Geol. Utraiectina,* 46.

ten Haven, H.L., Baas, M., de Leeuw, J.W., and Schenck, P.A., 1987. Late Quaternary Mediterranean sapropels, I. On the origin of organic matter in Sapropel S_7. *Mar. Geol.,* 75:137–156.

Truffert, C., Chamot-Rooke, N., Lallemant, S., de Voogd, B., Huchon, P., and Le-Pichon, X., 1993. The crust of the Western Mediterranean Ridge from deep seismic data and gravity modelling. *Geophys. J. Int.,* 114:360–372.

Ms 160IR-110

NOTE: Core-description forms ("barrel sheets") and core photographs can be found in Section 5, beginning on page 535. Forms containing smear-slide data can be found in Section 6, beginning on page 951. Color reflectance, physical properties, chemistry, and thin-section data are presented on the CD-ROM (back pocket).